Poly(vinylidene fluoride) membranes: Preparation, modification, characterization and applications

by

Chenggui Sun

A thesis
presented to the University of Waterloo
in fulfillment of the
thesis requirement for the degree of
Doctor of Philosophy
in
Chemical Engineering

Waterloo, Ontario, Canada, 2009

AUTHOR'S DECLARATION

I hereby declare that I am the sole author of this thesis. This is a true copy of the thesis, including any required final revisions, as accepted by my examiners.

I understand that my thesis may be made electronically available to the public.

Abstract

Hydrophobic microporous membranes have been widely used in water and wastewater treatment by microfiltration, ultrafiltration and membrane distillation. Poly(vinylidene fluoride) (PVDF) materials are one of the most popular polymeric membrane materials because of their high mechanical strength, excellent thermal and chemical stabilities, and ease of fabrication into asymmetric hollow fiber membranes.

In this work, specialty PVDF materials (Kynar 741, 761, 461, 2851, RC-10186 and RC10214) newly developed by Arkema Inc. were used to develop hollow fiber membranes via the dry/wet phase inversion. These materials were evaluated from thermodynamic and kinetic perspectives. The thermodynamic analysis was performed by measuring the cloud points of the PVDF solution systems. The experimental results showed that the thermodynamic stability of the PVDF solution system was affected by the type of polymer and the addition of additive (LiCl); and the effects of the additive (LiCl) depended on the type of polymer. The kinetic experiments were carried out by determining the solvent evaporation rate in the "dry" step and the small molecules (solvent, additive) diffusion rate in the "wet step". Solvent evaporation in the early stage could be expressed quantitatively. In the "wet" step, the concentrations of solvent and additive had a linear relationship with respect to the square root of time ($t^{1/2}$) at the early stage of polymer precipitation, indicating that the mass-transfer for solvent-nonsolvent exchange and additive LiCl leaching was diffusion controlled. The kinetic analysis also showed that the slope of this linear relationship could be used as an index to evaluate the polymer precipitation rate (solvent-nonsolvent exchange rate and LiCl leaching rate).

The extrusion of hollow fiber membranes was explored, and the effects of various fabrication parameters (such as dope extrusion rate, internal coagulant flow velocity and take-up speed) on the structure and morphology of the hollow fiber membranes were also investigated. The properties of the hollow fiber membranes were characterized by gas permeation method and gas-liquid displacement method. The morphology of the hollow fibers was examined by scanning electron microscope (SEM). It was found that Kynar 741 and 2851 were the best among the PVDF polymers studied here for the fabrication of hollow fiber membranes.

In order to reduce the problems associated with the hydrophobicity of PVDF on hollow fiber module assembly, such as tubesheet leaking through problem and fouling problem, amine treatment was used to modify PVDF membranes. Contact angle measurements and filtration experiments were performed. Fourier-transform infrared (FT-IR) spectroscopy and energy dispersive x-ray analysis (EDAX) were used to analyze the modified polymer. It was revealed that the hydrophilicity of the modified membrane was improved by amine treatment and conjugated C=C and C=O double bonds appeared along the polymer backbone of modified PVDF.

Hollow fiber membranes fabricated from Kynar 741 were tested for water desalination by vacuum membrane distillation (VMD). An increase in temperature would increase the water productivity remarkably. Concentration polarization occurred in desalination, and its effect on VMD could be reduced by increasing the feed flowrate. The permeate pressure build-up was also investigated by experiments and parametric analysis, and the results will be important to the design of hollow fiber modules for VMD in water desalination.

Keywords: Poly(vinylidene fluoride), microporous membrane, thermodynamics, kinetics, hollow fiber, amine, membrane distillation, pressure build-up, concentration polarization

Acknowledgements

I would like to express my sincere gratitude to Dr. Xianshe Feng, for his invaluable guidance, advice and support in my four year's research and in the preparation of this thesis.

My deep appreciation also goes to all my friends in the membrane research group for their advice and assistance. I would like to thank Dr. Jialong Wu for FT-IR tests.

I appreciate the services and help from Patricia Anderson, Liz Bevan, Rose Guderian, Lorna Kelly and other departmental secretaries.

I would like to thank the examination committee for their advices and comments on my thesis.

I would like to thank all my best friends for their support and encouragement.

Most importantly, I would like to thank my grandparents and parents for their love and support.

Research support from Arkema Inc. and the Natural Sciences and Engineering Research Council of Canada (NSERC) is gratefully acknowledged.

To my grandparents, parents and all my best friends

Table of Contents

Appendices:

List of Figures

List of Tables

List of Abbreviations

AGMD	Air gap membrane distillation
AMP	2-Amino-2-methyl-1-propanol
ANOVA	Analysis of variance
DMAc	Dimethylacetamide
DCMD	Direct contact membrane distillation
DEA	Diethanolamine
ED	Electrodialysis
EDAX	Energy dispersive x-ray analysis
FT-IR	Fourier-transform infrared spectroscopy
GS	Gas separation
ID	Inner diameter
LM	Liquid membrane
MD	Membrane distillation
MEA	Monoethanolamine
MF	Microfiltration
MWCO	Molecular weight cut-off
MS	Mass spectrometry
NF	Nanofiltration
NMP	N-methyl-2-pyrrolidone
OD	Outer diameter
PE	Polyethylene
PEG	Poly(ethylene glycol)
PMA	Poly(methyacrylate)
PMMA	Poly(methyl methacrylate)
PP	Polypropylene
PTFE	Polytetrafluoroethylene
PV	Pervaporation
PVAc	Poly(vinylacetate)
PVDF	Poly(vinylidene fluoride)

PVP	Poly(vinyl pyrrolidone)
RO	Reverse osmosis
SEM	Scanning electron microscopy
SGMD	Sweeping gas membrane distillation
SS	Sum of squares
TSS	Total sum of squares
UF	Ultrafiltration
VMD	Vacuum membrane distillation
XPS	X-ray photoelectron spectroscopy

List of Symbols

α_1	Compaction factor
α_2	Confidence level
γ	Surface tension
δ	Thickness
ε	Porosity
η	Feed viscosity
μ	Gas viscosity
θ	Contact angle
λ	Mean free path

Nomenclature

A	Membrane area
C_f	Concentration of feed solution
C_p	Concentration of permeate
C_t	Concentration of small molecules at time t
C_∞	Concentration of small molecules at infinite time
D	Diameter of the gas molecule
D_K	Knudsen diffusion coefficient
D_{ns}	Diffusion coefficient of nonsolvent
D_s	Diffusion coefficient of the solvent
F	Local molar flowrate of vapor
F_o	Permeate product flowrate
H	Henry's law constant
J_{ps}	Permeation flux obtained with the dextran solution
J_{pwp}	Pure water permeation flux
J_{total}	Permeance of a gas through a membrane
K	Slope of equation 2.5
K_f	Mass transfer coefficient for the feed
K_m	Membrane permeability
K_{ov}	Overall mass transfer coefficient
M	Molecular weight
N	Permeation flux
$\overline{P}$	Average pressure of the feed side and the permeate side
ΔP	Pressure difference
P_e	Pressure of the vapor at the dead end of a fiber
$P_{f,i}$	Partial pressure of permeate species i
P_o	Pressure of the vapor at the outlet of a fiber
$P_{p,i}$	Partial pressure of permeate species at permeate side

P_{sat}	Saturated vapor pressure
Q	Gas flux
R	Gas constant
R_{rej}	Rejection ratio
R_{df}	Fouling resistance
T	Temperature
V	Volume
W_t	Weight of the cast film and the glass plate at time t
W_0	Value of W_t at time $t = 0$
W_∞	Value of W_t when the solvent is completely evaporated

b	Empirical parameter, Chapter 3
d_i	Inner diameter of a hollow fiber
d_o	Outer diameter of a hollow fiber
k	Boltzman constant
l	Effective pore length
m	Empirical parameter, Chapter 3
n	Number of hollow fiber
p	Pressure
Δp	Pressure across the membrane
r	Pore radius
Δt	Time
x_b	Mole fraction of NaCl in the bulk feed
x_i	Mole fraction of NaCl at the interface
z	Distance from random position to the dead end

Chapter 1

Introduction

1.1 Background

Membranes and membrane processes have been widely used in industries. Membranes are not only interphases but also selective barriers between the two phases that need to be physically separated [Mulder, 1991; Ho and Sirkar, 1992]. Membrane processes can be classified as ultrafiltration (UF), microfiltration (MF), membrane distillation (MD), reverse osmosis (RO), nanofiltration (NF), electrodialysis (ED), dialysis, gas separation (GS), separation processes by liquid membranes (LM) and pervaporation (PV) [Mulder, 1991; Cheryan, 1998].

Currently, both organic and inorganic materials have been used to manufacture membranes [Mulder, 1991; Cheryan, 1998]. And there are two classes of organic membrane materials, i.e., hydrophobic materials and hydrophilic materials [Zeman and Zydney, 1996]. Polytetrafluoroethylene (PTFE) and polypropylene (PP) are two of the most popular hydrophobic materials. PTFE flat sheet or tubular membranes and PP hollow-fiber membranes, produced by stretching or thermal method, have been widely used. However, the symmetric structures of membranes fabricated via the above methods resulted in a considerably large membrane resistance to mass transfer [Kong and Li, 2001].

As a membrane material, Poly(vinylidene fluoride) (PVDF) offers many advantages that enable it to compete favorably with other polymer materials. Its molecular formula is listed as following:

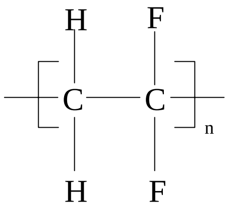

$$\left[-\overset{\displaystyle H}{\underset{\displaystyle H}{C}}-\overset{\displaystyle F}{\underset{\displaystyle F}{C}}- \right]_n$$

As a semicrystalline polymer, PVDF crystalline phase provides thermal stability while the amorphous phase provides the desired membrane flexibility [Kong and Li, 2001]. What's more, PVDF membranes have high hydrophobicity, mechanical strength, and thermal and chemical stabilities [Wang et al., 1999]. In addition, PVDF is soluble in high-boiling point and commercially available solvents: N-methyl-2-pyrrolidone (NMP), N-dimethylformamide (DMF) and Dimethylacetamide (DMAc) [Bottino et al., 1988], which make it easier to fabricate more permeable asymmetric membranes via the dry/wet phase inversion method.

Dry/wet phase inversion method was developed from the "immersion-precipitation" method. In this method, a homogeneous polymer solution is cast to a piece of nascent film or spun to a nascent hollow fiber, and then immersed into a coagulation bath, where phase separation and polymer precipitation occurs [Cheng et al., 1999]. The essence of this method is to obtain a porous solid from a homogeneous solution in a controlled manner. The process of solidification is initiated by a phase transition of the solution into a polymer-lean phase and a polymer-rich phase, which densifies to form a solid matrix at a certain stage. The membrane porous structure can be tuned by controlling the initial stage of phase transition [Mulder, 1991; Cheng et al., 1999].

Dry/wet phase inversion process consists of three steps [Reuvers et al., 1981; Mulder, 1991; Cheryan, 1998]: 1) composition change in the polymer solution by the solvent evaporation before immersion into the coagulation bath (nonsolvent); 2) composition change in the polymer solution after immersion into the coagulation bath: the solvent diffuses into the coagulation bath whereas the nonsolvent will diffuse into the cast film; 3) demixing process, which takes place when the composition of the polymer solution becomes thermodynamically unstable. Finally a solid porous membrane with an asymmetric structure is obtained.

PVDF microporous membranes have been widely used in water treatment and purification. Microfiltration, ultrafiltration, nanofiltration and reverse osmosis are four pressure-driven membrane processes. Membrane distillation (MD) is a newly developed thermally driven membrane process for water and wastewater treatment, which has attracted a lot of researchers' interests since the late 1990s [El-Bourawi et al., 2006]. The advantages of MD over the pressure-driven processes are: 1) complete rejection of ions, macromolecules, colloids, cells, and other non-volatile constituents, 2) lower operating pressures, 3) less demanding requirements for mechanical properties, 4) capability of recovering valuable products from effluents [Lawson and Lloyd, 1997; Ei-Bourawi et al., 2006].

In order to expand the application range of PVDF membranes due to the hydrophobic nature, physical modification and chemical modification are used to enhance membrane hydrophilicity [Pasquier et al., 2000; Tarvainen et al., 2000; Kushida et al., 2001; Hester and Mayes, 2002]. Various methods for modifying PVDF membranes have been proposed, including dip coating, chemical or radiochemical grafting, plasma treatment and chemical treatment [Bottino et al , 2000].

1.2 Objectives of research

The objectives of this research are to fabricate PVDF membranes from the specialty PVDF materials newly developed by Arkema Inc. and investigate their potential applications for water and wastewater treatment. In collaboration with Arkema, who worked on the material science of PVDF, the following tasks have been undertaken:

1) Evaluation of newly developed materials from thermodynamic and kinetic perspectives. The equilibrium thermodynamics of the ternary polymer-solvent-nonsolvent systems and the kinetics (i.e., the rate of solvent evaporation and polymer precipitation) of membrane formation were investigated.

2) Exploration of extruding hollow fiber membranes from the new PVDF materials. The effects of the fabrication parameters involved in hollow fiber spinning on the membrane properties (dimension, morphology, and performance) were investigated.

3) Modification of the PVDF membranes by chemical treatment. The influences of modification on the hydrophilicity, permeability and fouling resistance of the membranes were determined.

4) Demonstration of PVDF microporous membranes for use in desalination by vacuum membrane distillation (VMD). The operating parameters affecting

VMD performance were investigated and the mass transfer in VMD was analyzed.

1.3 Outline of the thesis

This thesis includes seven chapters.

Chapter 1 is the overview of membrane processes, membrane materials, membrane preparation techniques and the objectives of this research.

Chapter 2 reviews the prior works on the membrane formation mechanism, the preparation and characterization of microporous membranes, the modification of PVDF membranes, and membrane distillation processes.

In Chapter 3, the specialty PVDF materials newly developed by Arkema Inc. were used to cast membranes via the dry/wet phase inversion method. The membrane formation mechanism was studied from a thermodynamic and a kinetic point of view.

Based on the research findings from the thermodynamic and kinetic studies, the effects of various fabrication parameters on the properties of hollow fiber membranes were investigated in Chapter 4.

Chapter 5 deals with how to improve the hydrophilicity of PVDF membranes by amine treatment, in order to expand the applicability of PVDF membranes.

Chapters 6 is concerned with the application of microporous PVDF membranes in VMD. The mass transfer was analyzed, and the effects of operating variables (temperature, feed concentration, feed flowrate, membrane permeability), fluid dynamics and permeate pressure build-up inside the hollow fibers for shell side feed were investigated.

Chapter 7 summarizes the general conclusions drawn from this study and recommends the further research that shall be carried out in future.

Chapter 2

Literature review

2.1 Introduction to microporous membranes

2.1.1 Historical development in microporous membranes

The transport of water or other solvent through a semi-permeable membrane, termed as osmosis, has been known since 1748 [Lonsdale, 1982; Boddeker, 1995]. In 1855, Fick developed the first synthetic "membrane" with nitrocellulose [Cheryan, 1998]. In 1907, Bechhold prepared nitrocellulose membranes with graded pore sizes, coming up with the term ultrafiltration [Baker, 2004; Cheryan, 1998]. By the early 1930s, microporous membranes made of collodion were commercially available, and during the following 20 years, more polymers were discovered to make microfiltration membranes. At the end of the World War II, microfiltration has been widely used in drinking water treatment [Baker, 2004]. The period from 1960 to 1980 is the golden age of membrane technology. In the early 1960s, Sourirajan and Loeb discovered "immersion precipitation" – a new membrane fabrication method. The Loeb-Sourirajan membranes consist of a dense and thin "skin" layer and a sponge-like porous structure support sublayer. The membranes were defect free, with high fresh water productivity and high desalination efficiency. Their work contributed to the development of membrane science and membrane processes remarkably. Inspired by the idea of Loeb and Sourirajan, more membrane formation processes, such as interfacial polymerization and multilayer composite casting and coating, were developed. By 1980, both microfiltration and ultrafiltration had been established with large plants installed worldwide [Kesting, 1985; Baker, 2004].

2.1.2 Mass transport models through microporous membrane

Microfiltration and ultrafiltration are pressure-driven processes using microporous membranes, which permit the passage of certain components and retains other certain permeants [Cheryan, 1998]. Microfiltration and ultrafiltration can be divided into two general classes: depth filtration and screen filtration, as shown in Figure 2.1 [Baker, 2004]. The depth filtration removes the particles by capturing them in the pores of the membrane, as a result of the constrictions of pores and the adsorption along the tortuous paths. Most microfiltration processes are depth filtration. However, most ultrafiltration membranes with a relatively dense surface layer on a more open microporous support sublayer are screen filters. The pores of surface layer are smaller than the particles to be removed. The separation is achieved by particles being captured and accumulated on the surface of the membrane [Baker, 2004].

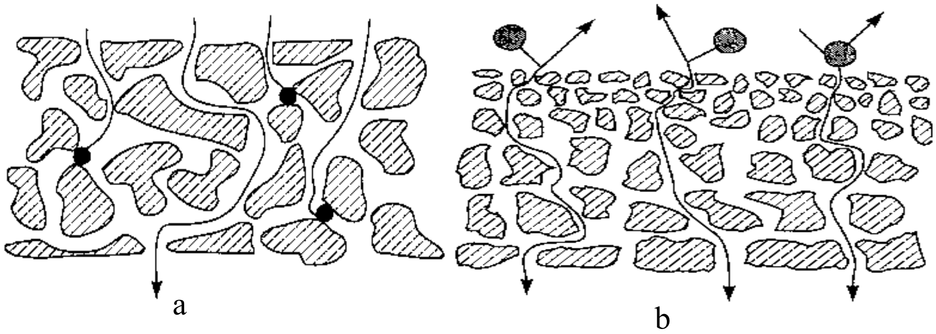

Figure 2.1 Depth filtration mechanism (a) and screen filtration mechanism (b) of separation of particulates [Baker, 2004].

In membrane separation processes, the flux through the membrane may decrease due to the concentration polarization. Since the solute in a solution is retained by the membrane whereas the solvent permeates through the membrane, the solute can accumulate at the membrane surface leading to an increase in the solute concentration at the membrane surface [Mulder, 1991]. This is shown in Figure 2.2. This phenomenon is called concentration polarization, and the effect of concentration polarization can be reduced by controlling the feed flow hydrodynamics. However, if particles, colloids, emulsions, suspensions or macromolecules are deposited onto the membrane, as illustrated in Figure 2.2, membrane fouling will also occur, especially for microfiltration and ultrafiltration [Mulder, 1991]. In such cases, the permeate flux can be described by the Darcy's law [Ho and Sirkar, 1992], which relates the permeate flux to the resistances of the membrane and the fouling layer:

$$J = \frac{V}{A \cdot \Delta t} = \frac{\Delta p}{\eta(R_m + R_f)} \qquad (2.1)$$

where V is the quantity of permeate, A is the membrane area, and Δt is the filtration time, Δp is the pressure drop across the membrane, η is the viscosity of the feed, R_m is the membrane resistance, R_f is the resistance resulting from the membrane fouling layer.

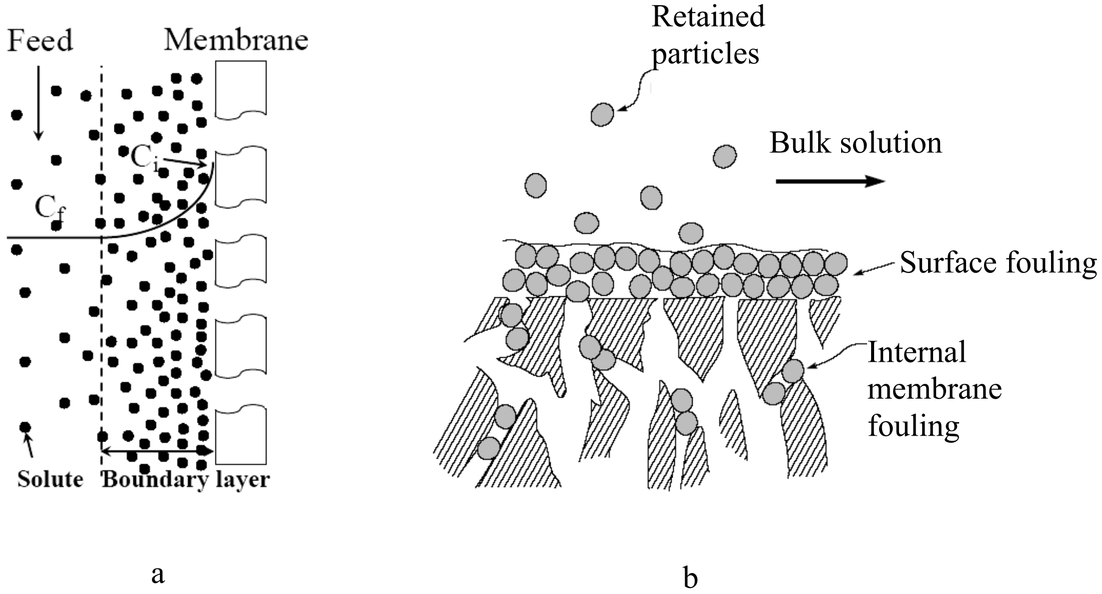

Figure 2.2 Schematic of the concentration polarization (a) and the membrane fouling (b) [Baker, 2004].

2.2 Fabrication of microporous membranes

2.2.1 Membrane and module preparation techniques

Immersion precipitation techniques that are used to cast flat membranes and spin hollow fiber membranes are different. They will be described below.

1. Casting of flat membrane

As shown in Figure 2.3, the polymer solution, often referred to as the casting solution, is cast directly upon a supporting layer by means of a casting knife. Then the cast film is immersed in a coagulant bath (nonsolvent) where the polymer precipitates and the membrane forms. Various liquids can be used as the nonsolvent, but water is the most widely used nonsolvent. The membranes obtained can be used directly or subject to a post treatment (e.g., heat treatment) [Mulder, 1991]. Flat membranes also can be easily cast by hand with the aid of a scraper, which are very useful for laboratory scale experiments.

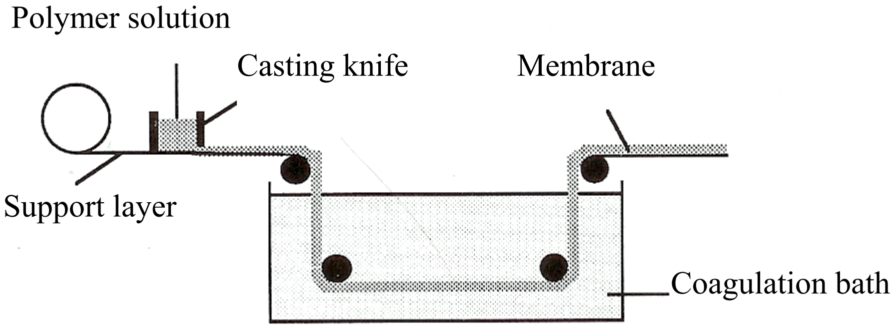

Figure 2.3 Schematic depicting the preparation of flat membranes [Mulder, 1991].

2. Fabrication of hollow fiber membrane

Hollow fiber membranes can be prepared via dry/wet spinning method. The preparation process is illustrated in Figure 2.4. The polymer solution is sent to the spinneret by pump or under gas pressure after being filtered. The internal coagulant is delivered to the inner tube of the spinneret to give stress to open the hollow fiber. After a short time of solvent partial evaporation in the air or a controlled atmosphere (the term "dry" originates from this step), the fiber is immersed into a coagulant bath, in which polymer precipitates and membrane forms [Mulder, 1991]. Polymer precipitation occurs on both sides of the fiber. After precipitation, the hollow fibers are collected.

For the dry/wet spinning process, the main parameters that affect the membrane dimensions and properties are: dope extrusion rate, solvent partial evaporation time, internal coagulant flow velocity, and take-up speed.

And in the dry/wet spinning process, the fiber dimensions depend on the dimension of spinneret directly, so it is important to choose the spinneret properly. The cross-section of commonly used spinneret is shown in Figure 2.5.

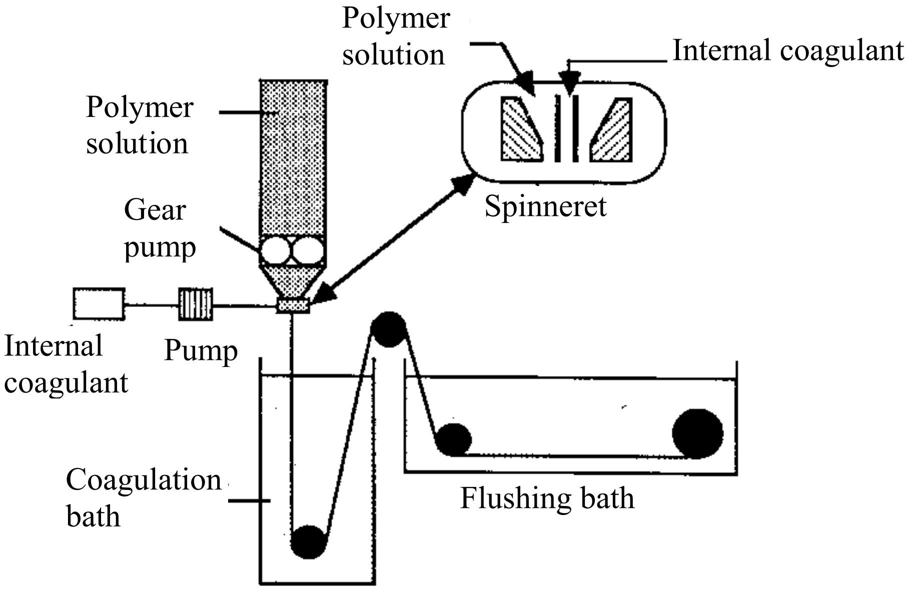

Figure 2.4 Schematic of a dry-wet spinning process [Mulder, 1991].

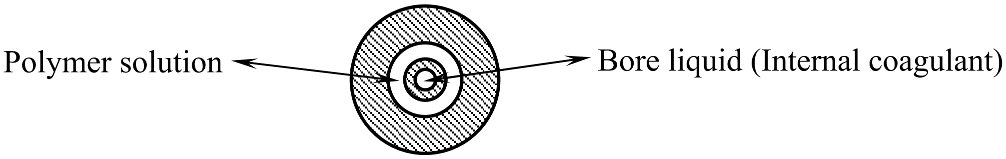

Figure 2.5 Cross-section of spinneret used for dry-wet spinning.

3. Tubesheet potting

The membrane modules are assembled by potting hollow fibers in a stainless steel sleeve tubing with an epoxy, so that the fibers are embedded in the epoxy to form a tubesheet [Ismail and Kumari, 2004; Childress et al., 2005]. One end of the tubesheet is cut open so that the permeate from the lumen side of the fibers can exit, as shown in Figure 2.6. Figure 2.7 illustrates a hollow fiber membrane potted by the resin.

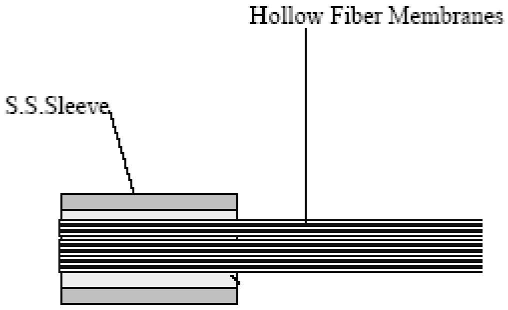

Figure 2.6 Schematic showing a tubesheet of hollow fiber membrane module.

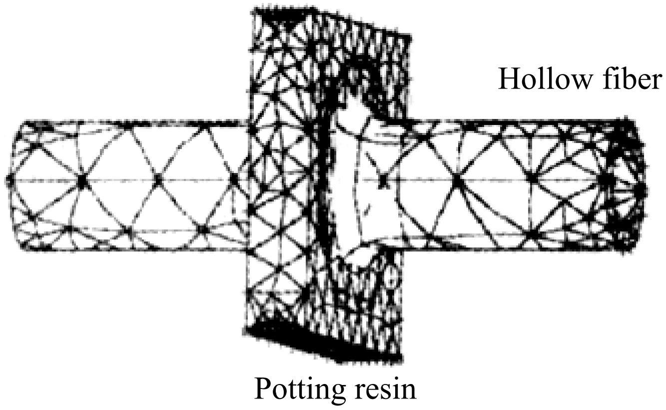

Figure 2.7 Schematic of a potted hollow fiber [Childress et al., 2005].

2.2.2 Mechanism of membrane formation in dry/wet phase inversion method: thermodynamics consideration and kinetics consideration

The structure of the membrane prepared via the dry/wet phase inversion method is mainly determined by: 1) the thermodynamic properties of the polymer-solvent-nonsolvent system, and 2) the kinetic properties, including the rate of solvent evaporation in the dry step, and the rate of phase separation in the immersion precipitation step [Young and Chen, 1991 b]. The phase diagram is a convenient tool to evaluate the thermodynamic aspects of the membrane precipitation process [Strathmann and Kock, 1971]. Kinetic studies on changes in composition due to the solvent evaporation or due to the solvent-nonsolvent exchange are essential to understand the formation of membrane and tune the pore structures of membrane [Matsuyama, 2000].

1. Thermodynamic aspect of membrane formation

From a thermodynamic point of view, the polymer-solvent-nonsolvent system, which can be regarded to have undergone an isothermal process, can be depicted in a ternary-phase diagram, as illustrated in Figures 2.8 and 2.9 [Witte et al., 1996; Barth et al., 2000; Ismail and Yean, 2003].

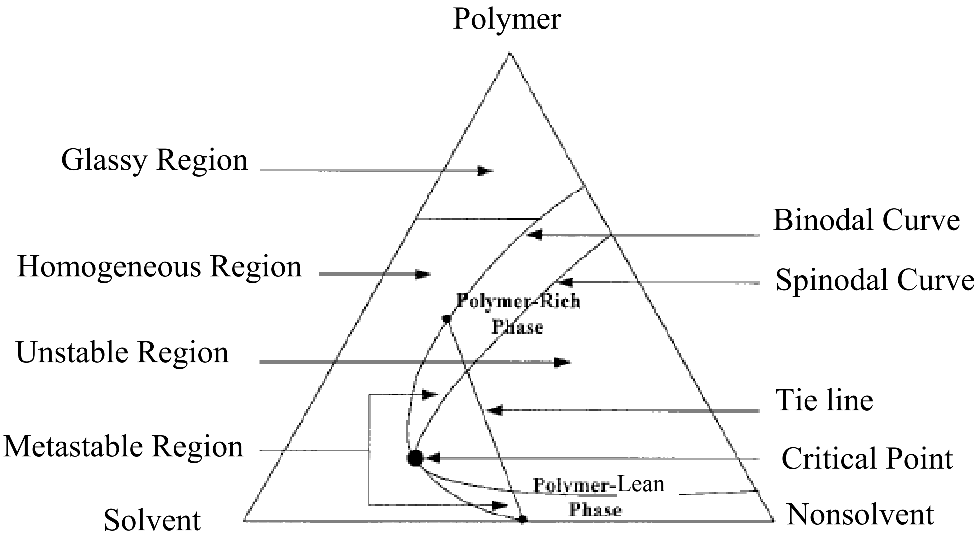

Figure 2.8 Ternary-phase diagram of polymer-solvent-nonsolvent system [Ismail and Yean, 2003].

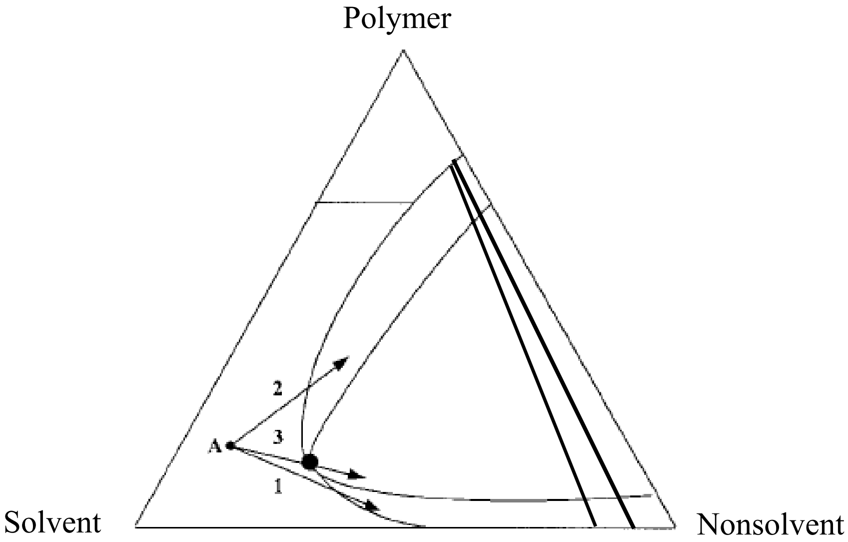

Path 1: Nucleation and growth (Polymer Rich Phase)

Path 2: Nucleation and growth (Polymer lean phase)

Path 3: Spinodal Decomposition

A : Initial composition of system.

Figure 2.9 Schematic representation of phase separation process [Ismail and Yean, 2003].

In the ternary-phase diagram, the corners of the triangle represent pure components (polymer, solvent and nonsolvent), the axes of the triangle represent binary combinations, and any point within the triangle represents a ternary component [Witte et al., 1996]. Essential elements of ternary-phase diagram consist of a binodal curve and a spinodal curve, a critical point, tie lines, and a glassy region [Ismail and Yean, 2003]. The binodal curve delimitates the two-phase region, polymer rich and lean phases. These two phases are in equilibrium and connected by the tie lines. The spinodal curve represents a line where all possible fluctuations (such as the addition of more solvent, the change of temperature) lead to instability. The binodal curve and the spinodal curve enclose a demixing boundary. The point where binodal and spinodal meet is referred to as the critical point [Machado, 1999; Ismail and Yean, 2003].

The ternary phase diagram can be divided into a homogeneous region and a region representing a liquid-liquid demixing gap by the binodal curve. In the homogeneous region, all three components (i.e., polymer, solvent, and nonsolvent) are miscible. The liquid-liquid demixing gap is reached when a sufficient amount of nonsolvent is added into the solution. An unstable region is enclosed by the spinodal curve. A metastable area, where phase separation by nucleation and growth takes place, exists between the spinodal and the binodal at low polymer concentrations, and a second metastable area is at higher polymer concentrations [Witte et al., 1996; Machado, 1999; Ismail and Yean, 2003].

Phase transformation of an originally homogeneous solution is usually brought about by varying the temperature or composition of the solution [Cheng et al., 1999]. A coagulation path in the ternary-phase diagram can represent changes in state and composition of the ternary system during membrane formation, which depends on the interactions between the components, the size and location of the miscibility gap, as well as the boundary between the demixing regions [Ismail and Yean, 2003]. Two different types of phase transition can be distinguished: (1) Liquid-liquid demixing: the completely miscible solution crosses the binodal boundary, i.e., from a stable homogeneous solution region into a two-phase region. (2) Solid-liquid demixing (crystallization of polymer, from homogeneous region to glassy region, or from unstable region to glassy region): a hypothetical boundary is located in the diagram since the viscosity of polymer solution increases to a certain value, the molecule motion of polymer will be limited, and then the membrane structure is fixed [Young and Chen, 1991 a]. Liquid–liquid demixing results in the typical cellular morphology with pores from polymer-lean phase surrounded by the membrane matrix from the polymer-rich phase. Solid–liquid demixing is from crystallizable segments of the polymer to form membranes by linking of particles. It is a slow process in comparison to liquid–liquid demixing because of the time needed for orientation of the polymer molecules, both for nucleus formation and for growth [Cheng et al., 2001]. Solid-liquid demixing may also contribute to pore formation especially in solutions containing crystallizable polymers such as cellulose acetate and poly(vinylidene fluoride). Liquid-liquid phase separation should be considered for solutions of both amorphous and crystallizable polymers [Nunes and Inoue, 1996].

For the liquid-liquid demixing, the homogeneous solution separates into two liquid phases either by nucleation and growth or spinodal decomposition, depending on the kinetic path in the phase diagram [Nunes, 1997]. Since the two phases are in equilibrium, their compositions are located at the ends of the tie line containing the starting solution. However, for the solid-liquid demixing, nucleation and growth are dominating and the two phases in equilibrium are the pure polymer crystal and the surrounding polymer-lean solution [Cheng et al., 1999].

Nucleation and growth is the expected mechanism when a system leaves the thermodynamically stable conditions and slowly enters the metastable region of the phase diagram between the binodal and the spinodal curves. Dispersed nuclei are formed and become stable if the activation energy for nuclei formation is higher than their surface free energy. Nucleation and growth is usually a slow process. Spinodal decomposition takes place in a fast quench into the two-phase region limited by the spinodal curve or even in a slower transition crossing the metastable region near the critical point. In this case, the phase separation starts with concentration fluctuations of increasing amplitudes, giving rise to two continuous phases, as shown in Figure 2.10, with a characteristic periodic interphase distance (d). In the later stages of phase separation, even for spinodal decomposition, phase coalescence may lead to a matrix/dispersed phase morphology. If the process is “frozen” early enough by a mobility change, a morphology with high interconnectivity is obtained [Nunes and Inoue, 1996].

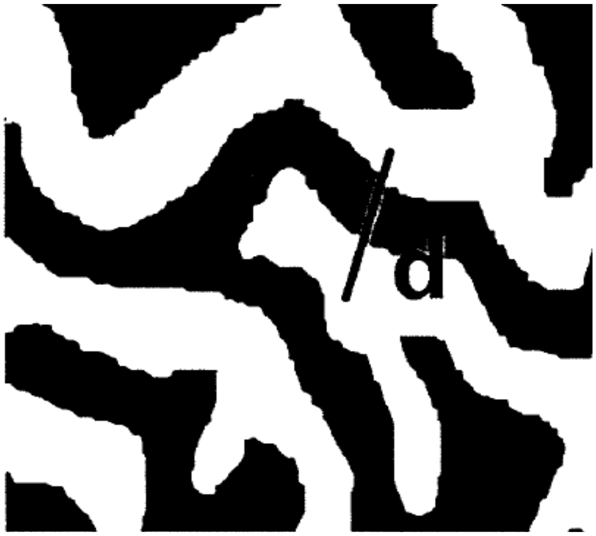

Figure 2.10 Schematic of co-continuous structure [Nunes and Inoue, 1996].

Two types of nucleation and growth can be envisioned to arise from the phase separation process. When demixing is started somewhere below the critical point, nucleation and growth of the polymer-rich phase occur in polymer-lean phase. Low-integrity powdery agglomerates would be produced. Hence, nucleation and growth of polymer-rich phase are not practical in membrane formation [Ismail and Yean, 2003]. On the other hand, when demixing is started somewhere above the critical point, polymer-lean phase is nucleating and growing in polymer-rich phase. The polymer-lean phase forms porous structure while the polymer-rich phase results in solid matrix of membrane. Occasionally, nucleated droplets of polymer-lean phase would grow into macrovoids if the diffusion flow of solvents from the surrounding polymer solution into the nuclei was larger than the diffusion flow of nonsolvents from the nuclei to the surrounding polymer solution [Ismail and Yean, 2003]. As long as the surrounding around the nuclei is stable, which means that no new nuclei are being generated in front of the existing ones and no gelation takes place in the freshly formed nuclei, nuclei growth will continue [Mulder, 1991]. However, the macrovoids, which are conical or spherical voids embedded within the membrane, are undesirable sites of mechanical weakness. Possible failures such as compaction or collapse of the membrane structure may occur when being applied to high-pressure driven separation processes [Zeman and Fraser, 1994; Lai et al., 1999].

Spinodal decomposition occurs in the unstable region of the spinodal envelope that leads to a bicontinuous and interconnected network structures. Eventually, solidification of the polymer-rich phase occurs in the glassy region by gelation, or crystallization that interrupts the phase separation process. Hence, the ultimate structure of the membrane is completely formed.

In addition to the recognition of regions where different phase separation mechanisms take place, in order to predict the membrane morphologies, one must know how the polymer solution, in contact with a non-solvent bath, changes its composition with time and where it enters the two-phase region. Reuvers and Smolders [Cited by Hao and Wang, 2003] measured the time that it takes before liquid–liquid demixing occurs by light transmission experiments on an immersed casting solution. It is shown that the liquid–liquid demixing process in polymer solutions during membrane formation may proceed in two different ways, instantaneous demixing and delayed demixing. Instantaneous demixing means that the membrane is formed immediately after immersion in the nonsolvent bath, whereas it takes some time before the ultimate membrane is formed in the case of delayed demixing [Mulder, 1991]. This can be illustrated by the relationship between the light transmittance and the immersion time shown in Figure 2.11 [Van´t Hof et al., 1992].

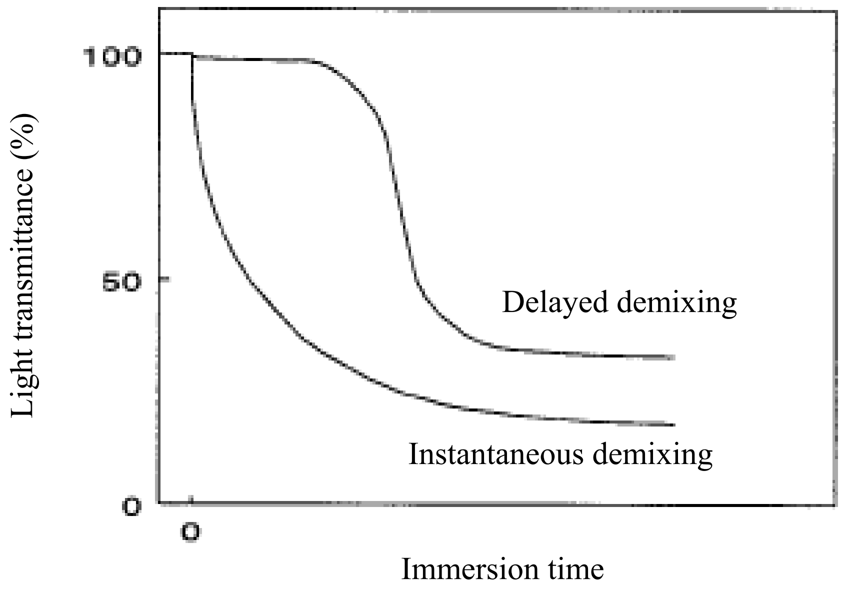

Figure 2.11 Light transmittances as a function of immersion time [Van´t Hof et al., 1992].

Two types of demixing processes, which can lead to different membrane structures, can be distinguished by the composition path of the cast polymer film at the very moment of immersion (at t<1 second, shown in Figure 2.12). The composition path gives the concentration at any point in the film at a particular moment. For any other time another compositional path will exist [Mulder, 1991].

Because diffusion starts at the film/bath interface, the change in composition is first noticed in the upper part of the film. This change can also be observed from the composition paths given in Figure 2.12. Point t gives the composition at the top of the film while point b gives the bottom composition. Point t is determined by the equilibrium relationship at the film/bath interface $\mu_i(film) = \mu_i(bath)$. The composition at the bottom is still the initial concentration in both examples. In Figure 2.12, for the instantaneous demixing, places in the film beneath the top layer t have crossed the binodal curve, indicating that the liquid-liquid demixing starts immediately after immersion. In contrast, for delayed demixing, all compositions directly beneath the top layer still lie in the one-phase region and are still miscible. No demixing occurs immediately after immersion. After a certain period of time, compositions beneath the top layer will cross the binodal curve and the liquid-liquid demixing will start to occur. The two different demixing processes can result in different membrane morphologies [Mulder, 1991].

Membranes formed by instantaneous demixing have a porous top layer and an open-cell macrovoid-like or sponge-like support layer. Such membranes generally show size exclusion capabilities and are used in microfiltration and ultrafiltration processes. The spinodal decomposition is responsible for the rapid phase separation [Hao and Wang, 2003]. Membranes formed by delayed demixing tend to have a dense skin and are appropriate for uses in gas separation, pervaporation and reverse osmosis, where dense membrane structures are needed [Shimizu et al., 2002]

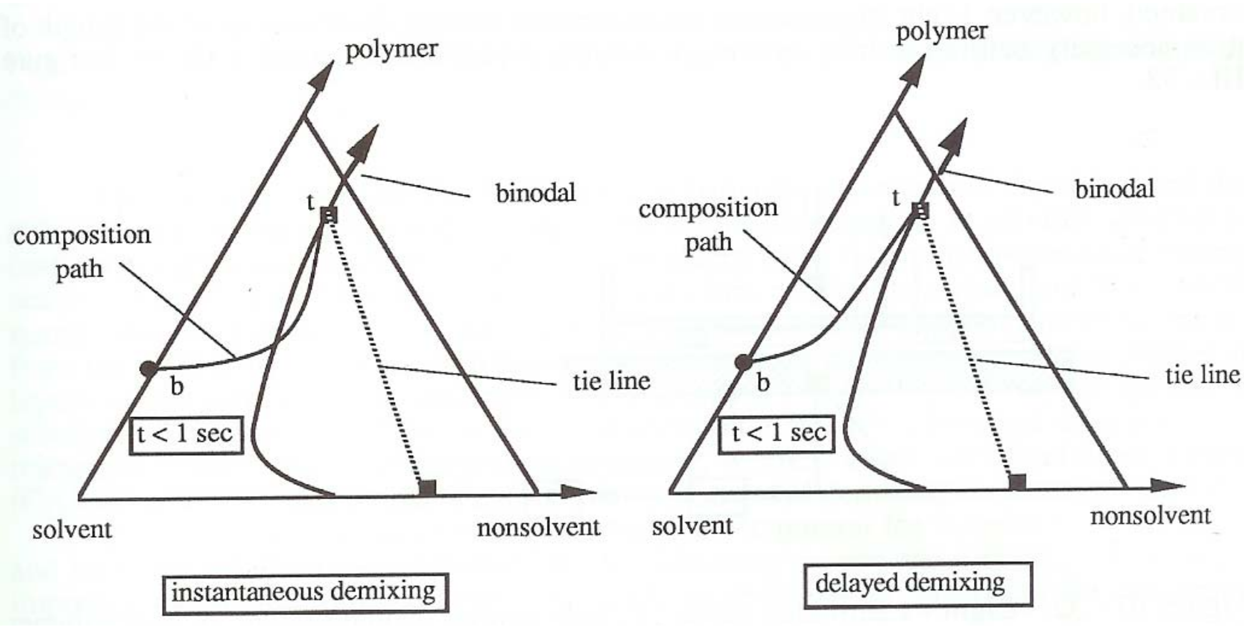

Figure 2.12 Precipitation paths in instantaneous (a) and delayed (b) demixing; t, the top of the cast film; b the bottom of the cast film [Mulder, 1991].

2. Kinetic aspect of membrane formation

An important feature of the microporous membranes fabricated via dry/wet phase inversion method is a relatively denser "skin" on the porous support layer. For microfiltration and ultrafiltration applications, the skin layer provides the permselectivity whereas the porous support layer contributes strength [Patsis and Henriques, 1999]. Besides the thermodynamics, the kinetic effects also play an important role in determining the formation of microporous structure. The skin and macroviod formation are influenced by: a) the solvent evaporation in the dry step, b) the solvent-nonsolvent exchange rate in the wet step – polymer precipitation, and c) the additive leaching rate if additives are present in the polymer solution.

1) Dynamics of the solvent evaporation in membrane formation

Relatively few experimental investigations on solvent evaporation have been reported, and the experimental work have been concerned with cellulose acetate/acetone solution [Castellari and Ottani, 1981; Krantz et al., 1986; Tsay and Mchugh, 1991] and polyetherimide (PEI)/ NMP or DMAc solution systems [Huang and Feng, 1995]. A few theoretical models were developed to describe the solvent evaporation, but no reliable predictions of the solvent evaporation rate have been made.

Quantitative data on solvent evaporation rates corresponding to cellulose actate/acetone films cast under different conditions were reported by Sourirajan and Kunst for the first time [1970]. The first evaporative model was proposed by Anderson and Ullman [1973]. Their assumptions include semi-infinite film thickness, constant surface concentration, negligible film shrinkage, and isothermal mass transfer. Some of these assumptions were relaxed in the model of Castellari and Ottani [1981], who considered finite film thickness, uniform film shrinkage, and variable surface concentration. Their numerical analysis indicated that for a given composition of the casting solution, there was an optimum evaporation time for the formation of the skin layer, depending on the evaporation temperature and the composition of the atmosphere.

It should be pointed out that in these models, a self-diffusion coefficient was utilized in the mass transfer equations. Krantz et al. [1986] modified the models by incorporating a semi-empirical correlation for the binary-diffusion coefficient and a proper description of the mass transfer into the ambient gas phase. Tantekin-Ersolmaz derived the first binary evaporative model, which considered coupled heat and mass transfer and were only valid for a short period of evaporation [Cited by Altinkaya and Ozbas, 2004]. In a subsequent study, Shojaie et al. presented a fully predictive nonisothermal model that incorporates excess volume of mixing effects and a correlation for the binary diffusion coefficient. The theoretical values were in good agreement with the experiment data [Cited by Altinkaya and Ozbas, 2004].

2) Dynamics of the polymer precipitation

It is known that the formation of a microporous membrane results from the solvent-nonsolvent exchange. A relative denser skin layer forms at the initial stage of the polymer precipitation, and the thickness of skin layer grows with time [Patsis and Henriques, 1999]. Unfortunately, experimental and theoretical investigations of the solvent-nonsolvent exchange rate during polymer precipitation have been lacking. The existing work was carried out based on the ternary systems that constitute cellulose acetate solutions or poly(methyl methacrylate) (PMMA) solutions and a nonsolvent without any additives.

Currently, there are two approaches to investigate the dynamics of phase separation. One approach is known as cast-leaching experiment: the dynamics of the phase separation are studied by monitoring the composition of the coagulation bath. Altena et al. [1985] determined the diffusion coefficient and analyzed the diffusion coefficient. It was found that the outflow of a solvent from a polymer solution into a coagulation bath was essentially a pseudobinary solvent–nonsolvent diffusion process. The work of Patsis et al. [1990] and Kim et al. [1996] found that the outflow of the solvent from a polymer solution could be described by Fickian diffusion, no matter whether the nonsolvent was stirred or not. This implies that the mass transfer of small molecules in a polymer solution was the control step.

The other approach is to use an optical microscopy to monitor the front of the phase-separated region [Li and Jiang, 2005; Kim et al. 1996]. One important conclusion is that the gel front propagated with the square root of time ($t^{1/2}$) up to 60% of the film thickness. Furthermore, the results from experiments using some advanced techniques, such as the dark-ground optical technique and reflected light images, also proved that the mass transfer and gel formation were diffusion related. The solvent diffusion and the gelation front could be quantified by the diffusion coefficients.

Based on diffusion induced phase separation, Cohen et al. [1979] proposed a model to explain the formation of the skin layer. The essence of their model was the dependence of the chemical potentials on the composition in a ternary nonsolvent-solvent-polymer system. This model was in good agreement with the experimental data and could describe the systems up to the point of initial skin formation.

Anderson and Ullman [1973] derived mathematical expressions for the outflow of solvents from the polymer solutions. They predicted and observed the “lag time”, which was related to the delayed responses of polymer precipitation to the changes of solvent concentrations. Because the model was too complicated, Patsis et al. [1990] developed a model describing the growth of the skin layer and related it to the solvent nonsolvent exchange and the polymer type. Cheng et al. [1996] proposed a simplified “solution–diffusion” model to estimate the polymer concentration at the coagulation bath-gel interface, and the experimental results indicated that different solvent-nonsolvent systems contribute to different membrane structures.

2.3 Characterization of microporous membranes

The microporous membranes can be characterized in many ways, depending on the parameters needed. Two types of characterization parameters for porous membranes can be distinguished: a) structure-related parameters: pore size, pore size distribution, effective surface porosity, morphology; b) permeation-related parameter: molecular weight cut-off.

2.3.1 Mean pore size and effective surface porosity

Mean pore size and effective surface porosity are two important parameters determining the flux through the membrane. The gas permeation method is frequently used to determine the mean pore size and the effective surface porosity of membranes.

Mechanisms accounting for the transport of a gas across a microporous membrane are Knudsen diffusion and Poiseuille flow. The properties of Knudsen to the Poiseuille flow are governed by the ratio of the pore radius (r) to the mean free path (λ) of the gas molecules [Pandey and Chauhan, 2001]. The mean free path, which is the average distance that the diffusing molecule travels between two successive collisions [Imdakm and Matsuura, 2004], is given by

$$\lambda = \frac{kT}{\sqrt{2}\pi D^2 p} \qquad (2.2)$$

where k is the Boltzman constant, T is the temperature, D is the diameter of the gas molecule, and p is the pressure.

If $r/\lambda >> 1$, the Poiseuille flow predominates, and the gas flux (Q_{vis}) through the pore can be described by [Pandey and Chauhan, 2001]:

$$Q_{vis} = \frac{r^2 (P_1^2 - P_2^2)}{16 l \mu RT} \qquad (2.3)$$

where l is the effective pore length, μ is the gas viscosity, R is the universal gas constant, P_1 and P_2 are the gas pressure on the feed side and the permeate side, respectively.

If $r/\lambda << 1$, the Knudsen flow happens [Pandey and Chauhan, 2001]. The gas flux can be described by the following expression:

$$Q_{knu} = \frac{8r(P_1 - P_2)}{3l(2\pi MRT)^{1/2}} \tag{2.4}$$

where M is the molecular weight of the gas.

Gas permeation through a nonporous membrane is governed by the solution-diffusion [Koros and Fleming, 1993]. For a microporous membrane, the solution–diffusion contribution to the overall flux is often negligible. The total gas permeation through the membrane is the combination of Poiseuille flow and Knudsen flow. The permeance of a gas through the microporous membrane can be obtained by [Wang et al., 1999]:

$$J_{total} = \frac{F_{total}}{A\Delta P} = \varepsilon \frac{1}{lRT}\left[\frac{r^2}{8\mu}\overline{P} + \frac{2r}{3}\left(\frac{8RT}{\pi M}\right)^{1/2}\right] \tag{2.5}$$

or

$$J_{total} = K\overline{P} + \mathrm{c} \tag{2.6}$$

where ε porosity, $K = \frac{r^2\varepsilon}{8\mu RTl}$, $c = \frac{2}{3}(\frac{8RT}{\pi M})^{1/2}\frac{1}{RT}\frac{r\varepsilon}{l}$, $\overline{P} = (P_1 + P_2)/2$, F_{total} the gas permeation flowrate, A membrane area and ΔP the pressure difference between the permeate side and the feed side. The values of K and c can be obtained from the slope and the intercept of the J_{total} versus $\overline{P}$ plot [Liu, 2003]. Therefore, the mean pore radius can be determined by equation 2.7:

$$r = \frac{16}{3}(\frac{K}{c})\left(\frac{8RT}{\pi M}\right)^{1/2}\mu \tag{2.7}$$

The surface porosity ε and the effective pore length l cannot be evaluated individually, but their ratio ε/l can be found from

$$\frac{\varepsilon}{l} = \frac{8\mu RT}{r^2} K \tag{2.8}$$

2.3.2 Pore size distribution

The pore size distribution is also important for microporous microfiltration and ultrafiltration membranes. Figure 2.13 is a schematic of the pore size distribution of a microporous membrane [McGuire et al., 1995].

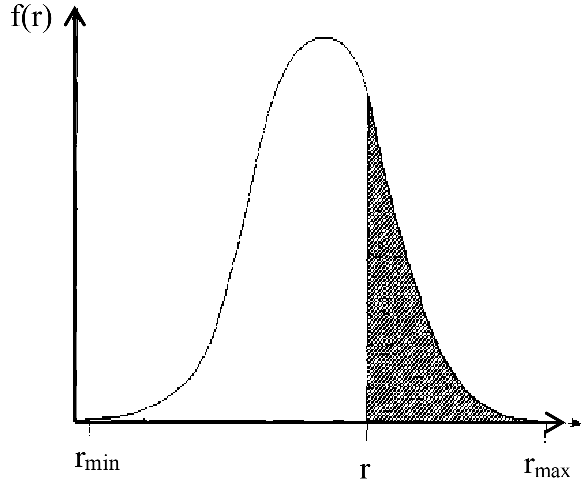

Figure 2.13 Illustration of pore size distribution. The shaded area represents the number fraction of pores in the membrane between *r* and r_{max} [McGuire et al., 1995].

The main methods used to determine pore size distribution are gas-liquid displacement, mercury porosimetry, electron microscopy, adsorption-based methods, thermo-porometry, and permporometry [Cuperus and Smolders, 1991].

In the present study, the gas-liquid displacement method was used. This method is based on the fact that a pressure is needed to force a non-wetting liquid to flow through the pores of a membrane; the gas pressure differential across the membrane should be able to overcome the capillary force caused by the surface tension of the liquid [Shao et al., 2004]. This force can be calculated by equation 2.9:

$$\Delta P = \frac{2\gamma \cos\theta}{r} \qquad (2.9)$$

where γ *is* the surface tension of the liquid, θ is the contact angle of the liquid on the inner surface of the pore, and r is the radius of the cylindrical pore. This equation suggests that if a wetting liquid penetrates the membrane pores, an elevated gas pressure will be necessary to open the pores gradually [Piątkiewicz et al., 1999; Shao et al., 2004]. In order to simplify the mathematical treatment, all the pores of comparable sizes can be grouped. The radius of *i*th group of pores is represented by r_i, and the corresponding porosity is represented by ε_i.

Assume that N+1 (N: number of pore groups) groups of pores have been opened at a certain gas pressure, and the (N+1)th group is being opened. The radius of pores currently being opened can be estimated by equation 2.9, and the porosity can be calculated from equation 2.10 [Shao et al., 2004]:

$$\varepsilon_{N+1} = \frac{J^c - \sum \frac{\varepsilon_i}{RTL}\left[\phi_i D_K + (1+\phi_i)\left(\frac{\pi}{4} D_K + \frac{r_i^2}{8\mu}\overline{P_{N+1}}\right)\right]}{\frac{1}{RTL}\left[\phi_{N+1} D_K + (1-\phi_{N+1})(\frac{\pi}{4} D_K + \frac{r_{N+1}^2}{8\mu}\overline{P_{N+1}})\right]} \qquad (2.10)$$

where superscript C means “current”, D_K is the Knudsen diffusion coefficient, which can be described by $D_K = \frac{2r_i}{3}\sqrt{\frac{8RT}{\pi M}}$. ϕ_i is the contribution of Knudsen diffusion in this group of pores, which can be written as $\phi_i = \frac{1}{1+2r_i/\lambda_i}$.

The initial porosity ε_i can be obtained by assuming the summation term in the nominator of equation 2.10 to be zero. When only the Hagen-Poiseuille regime occurs, which means $\phi=0$, a simpler equation can be obtained [Shao et al., 2004]:

$$\varepsilon_{N+1} = \frac{8RT\mu L * \frac{J_C}{P_{N+1}} - \sum_{1}^{N} \varepsilon_i r_i^2}{r_{N+1}^2} \qquad (2.11)$$

Then the total porosity of a membrane can be obtained by following equation.

$$\varepsilon_t = \sum \varepsilon_i \tag{2.12}$$

Thus, the pore size distribution is defined as

$$f(r_i) = \frac{\sum_{1}^{i} \varepsilon_i}{\varepsilon_t} \tag{2.13}$$

2.3.3 Membrane morphology

The morphology of microporous membranes is a three-dimensional structure, which is complex, diverse, and irregular. It can be studied by scanning electron microscopy (SEM) in terms of the cross-section, the top layer and bottom layer (or inner and outer surfaces of hollow fiber membranes) [Márquez-Rocha et al., 2001; Khayet et al., 2002; Khayet, 2003]. In addition, the porosity and the pore size distribution can be estimated from the SEM photographs [Mulder, 1991].

2.3.4 Molecular weight cut-off

Microporous membranes only permit the passage of the solutes whose molecules are smaller than the pores [Malaisamy et al., 2002]. Because the molecular size increases with an increase in molecular weight, the microporous membranes can be characterized by testing the rejection of various solutes of different molecular weights [Hernández et al., 1996]. The molecular weight cut-off (MWCO) of a membrane, which is the molecular weight of a molecule that is rejected at 90%, can provide the separation characteristics of microporous membranes via size exclusion [Snir et al., 1996; Comerton et al., 2009]. MWCO has been widely used to rate microporous membranes.

2.4 Surface modification of PVDF membrane

2.4.1 Surface modification methods:

As discussed before, PVDF is one of the most popular hydrophobic membrane materials. The PVDF membranes have been widely used in microfiltration and ultrafiltration due to their high mechanical strength, excellent thermal and chemical stability. However, the hydrophobic nature of its surface limits its application. For instance, the protein fouling, which results from the hydrophobicity of PVDF membranes, often causes severe decrease of the flux [Su, 2008].

Methods that can hydrophilize the PVDF membranes are: a) chemical treatment (e.g., chemical dehydrofluorination with alkaline solutions) [Stengaard, 1988]; b) coating method (e.g., dipping or spraying water-soluble polymers or amphiphilic materials) [Liu et al., 2006]; c) surface grafting (e.g., grafting hydrophilic monomer onto hydrophobic polymers via pulsed plasma, corona discharge, ozone treatment, gamma radiation and electron beam irradiation) [Liu et al., 2006].

Both the coating method and surface grafting method have shortcomings. The coated surface layers of membrane are removable; especially they are often sensitive to the pH of the solution. Grafting can lead to reduced permeability [Ying et al., 2002]. In light of this, the chemical modification of the PVDF membranes may be a promising technique. It may be based on reactions involving the elimination of F$^-$ units and the formation of the C=C double bonds along the polymer backbone [Stengaard, 1988; Zhao and Urban, 1999]. Stengaard [1988] used the alkaline treatment as the pretreatment for grafting selected hydrophilic polymers onto PVDF UF membrane. Ross et al. [2000] used concentrated sodium hydroxide to modify PVDF films. A possible mechanism that was proposed by Brewis et al. [1996] and discussed by Ross et al. [2000] is:

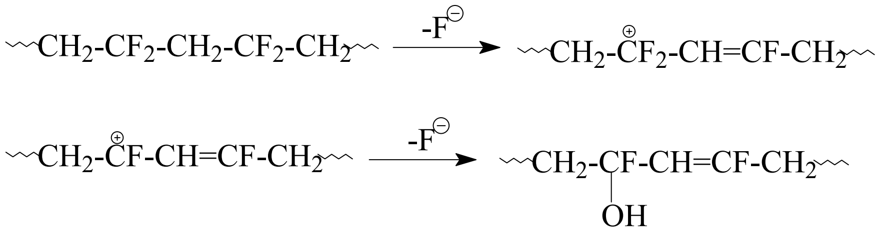

$$\sim CH_2\text{-}CF_2\text{-}CH_2\text{-}CF_2\text{-}CH_2\sim \xrightarrow{-F^{\ominus}} \sim CH_2\text{-}\overset{\oplus}{C}F_2\text{-}CH{=}CF\text{-}CH_2\sim$$

$$\sim CH_2\text{-}\overset{\oplus}{C}F\text{-}CH{=}CF\text{-}CH_2\sim \xrightarrow{-F^{\ominus}} \sim CH_2\text{-}\underset{OH}{C}F\text{-}CH{=}CF\text{-}CH_2\sim$$

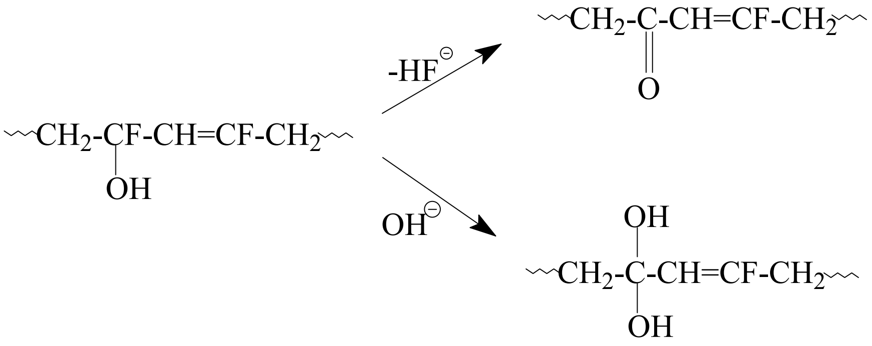

2.4.2 Techniques for molecular structure analysis

The techniques that are used to analyze the reaction mechanism are: X-ray photoelectron spectroscopy (XPS), mass spectrometry (MS) and Fourier-transform infrared (FT-IR) spectroscopy.

XPS provides chemical state information as well as a quantitative surface chemical analysis. The technique itself involves bombarding the sample with X-rays in ultra high vacuum. The X-rays cause the sample to emit photoelectrons, which result in the yielding of the XPS spectrum. Shifts in the peaks obtained represent differences in the chemical structure of the sample [Ross et al., 2000].

Mass spectrometry (MS) is a relatively simple concept: a compound is ionized, then the ions are separated by a mass analyzer based on the mass/charge ratio of each ion unit, and the number of ions with same mass/charge "unit" is recorded as a spectrum, which provide information to analyze molecular size and structure [Silverstein et al., 2005].

Fourier-transform infrared (FT-IR) spectroscopy is another efficient tool for the study of molecular structure. Because an organic molecule can absorb and convert the infrared radiation of frequencies into the energy of molecular rotation, an IR spectrum can offer the information of the entire molecule. Although it is true that certain groups of atoms give rise to bands at or near the same frequency, it still provides useful information to analyze the structure of molecules [Silverstein et al., 2005].

2.5 Membrane processes for water treatment and purification

2.5.1 Pressure-driven membrane processes

Microfiltration, ultrafiltration, nanofiltration and reverse osmosis are four widely used pressure-driven membrane technologies for water treatment and purification.

Reverse osmosis can separate small molecular weight solutes such as inorganic salts and glucose from water [Mulder, 1991]. It is a well established process and has been applied in desalination of brackish water or sea water [Leiknes, 2009]. Nanofiltration is a relatively new process that uses membranes with pores larger than those in RO membranes. But it is small enough to retain many organic compounds such as sugars [Cheryan, 1998]. Ultrafiltration is typically used to separate macromolecules from solutions. Solutes with molecular weights of a few thousand Daltons can be retained. Microfiltration is usually used to separate suspensions and emulsions in the "micron" range. Ultrafiltration and microfiltration membranes are microporous, and the solute rejection is achieved by depth filtration and screen filtration [Baker, 2004].The transport of water is proportional to the transmembrane pressure [Mulder, 1991; Cheryan, 1998].

2.5.2 Membrane distillation: thermally driven membrane process

1. Introduction membrane distillation process

Membrane distillation (MD), which is based on the vapor liquid equilibrium, is a relatively new and growing process in water treatment. It is a thermally driven process. In MD, a hydrophobic membrane is used. It acts as a physical support for the vapor/liquid interface, and prevents the liquid solution from entering the pores. The transport of vapor is achieved by diffusion from the interface to the permeate side through the hydrophobic pores [Bruggen and Vandecasteele, 2002].

Compared to the pressure-driven processes, MD is more efficient for removing non-volatile compounds from water in terms of solute rejection, because its operating pressures are usually on the order of a few atm, and theoretically, all non-volatile constituents can be rejected completely. Pressure-driven processes have not shown such capability to achieve high rejection rate [Lawson and Lloyd, 1997].

2. Membranes required in MD process

Microporous membranes can be used in MD. Hence, hydrophobic microfiltration and ultrafiltration membranes can be appropriate choices. MD membranes can be fabricated from any hydrophobic polymers such as polypropylene, polytetrafluoroethylene, polyethylene and PVDF [Banat and Simandl, 1996].

When selecting a membrane, the following must be considered: (1) good permeability, (2) strong hydrophobicity, (3) low thermal conductivity and good thermal stability, (4) excellent chemical resistance [Lawson and Lloyd, 1997].

3. Membrane distillation configurations

The driving force in MD is the pressure difference between the liquid/vapor interface and the permeate side. The low pressure at permeate side can be provided by the following four methods [Lawson and Lloyd, 1997; Martinez, 2002; Khayet, 2004; Ei-Bourawi et al., 2006]:

(1) A liquid at low temperature is maintained in direct contact with the membrane (i.e. direct contact membrane distillation, DCMD). The transmembrane temperature difference induces a vapor pressure difference.

(2) A stagnant air gap provides a condensing surface separated from the membrane (i.e. air gap membrane distillation, AGMD).

(3) A cold inert gas sweeps the permeate side and carries the vapor away (i.e. sweeping gas membrane distillation, SGMD).

(4) A vacuum is applied in the permeate side (i.e. vacuum membrane distillation, VMD).

Among all those configurations, DCMD has the simplest operation because the condensation is carried out inside the membrane module. VMD usually exhibits a higher permeation flux. AGMD generally exhibits a lower permeation flux, because of a new heat and mass transfer resistance due to the presence of the air gap. But the introduction of air gap can reduce considerably heat loss. SGMD exhibits higher permeation flux and separation efficiency than DCMD and AGMD. However, the energy loss is very high in SGMD, because it is quite difficult to recover the heat [Ei-Bourawi et al., 2006].

4. Applications of membrane distillation

The MD process has potential applications in desalination, water degassing, removal of traces of highly volatile solutes, and separation of alcohol-water mixtures [Bandini et al., 1992; Banat and Simandl, 1994; Bandini and Sarti, 1999; Izquierdo-Gil and Jonsson, 2003; Cabassud and Wirth, 2003; Li and Sirkar, 2005]. More detailed application areas of MD processes in water treatment and purification are summarized in Table 2.1 [Ei-Bourawi, 2006].

Each one of these four processes has its benefits and disadvantages for a given application. MD is currently considered to be a promising alternative technology. Its technical feasibility has been demonstrated at bench scale in laboratory with synthetic and real seawater [Hanemaaijer et al., 2006].

Table 2.1 MD processes and applications studied in laboratory [Ei-Bourawi, 2006].

Application area	MD configuration			
	DCMD	AGMD	SGMD	VMD
Pure water production from brackish water and seawater	✓	✓	✓	✓
Nuclear industry (water recovery)	✓			
Textile industry (wastewater treatment)	✓			✓
Chemical industry (removal of VOCs from water, separation of aqueous mixtures such as alcohol/water mixtures)	✓	✓	✓	✓
Pharmaceutical and biomedical industries (removal of water from blood and protein solutions, wastewater treatment)	✓			
Food industry and areas where high temperature are not favorable	✓	✓		✓

Chapter 3

Thermodynamics and kinetics involved in membrane formation from PVDF by the phase inversion method

---

3.1 Introduction

PVDF offers many advantages as a separation membrane material. It is a semicrystalline polymer containing crystalline and amorphous phases. The crystalline phase provides thermal stability, while the amorphous phase provides the desired membrane flexibility. Also, credits should be directed to its excellent chemical stability against corrosive chemicals and organic compounds including acids, alkaline, strong oxidants, and halogens [Kong and Li, 2001]. Thus, PVDF-based membranes are widely used in many processes.

Although PVDF membranes have been widely used, efforts are still required to improve the fabrication procedure to produce high performance membranes. Physical blending, chemical grafting and surface modification are methods that have been investigated [Yan et al., 2006]. A blend of PVDF and poly(methyl methacrylate) (PMMA) was used to fabricate asymmetric UF membranes. The addition of PMMA increases both pore size distribution in number of pores with sizes of 10–30 nm and the size of finger-like cavities [Nunes and Peinemann, 1992]. Besides PMMA, other polymers, such as poly(methyacrylate) (PMA) [Pralay, 1998], poly(vinylacetate) (PVAc) [Yan et al., 2006], were also used to improve PVDF membrane properties. Although the addition of these hydrophilic materials can improve certain properties of the membranes, it also reduces the mechanical strength. In this study, in order to find good PVDF materials for membrane fabrication, various grades of PVDF polymers developed by Arkema were evaluated.

Since PVDF has a low critical surface tension (about 25 dynes/cm), the penetration of the coagulant (water) into the nascent membrane during membrane formation by the phase inversion is restricted. Thus, the coagulation rate and the rate of solidification of nascent membranes are slow due to weak interactions between the coagulant (water) and the polymer. Therefore, considerable difficulties were encountered in preparing porous asymmetric PVDF hollow fiber membranes. An effective method to improve hollow fiber formation and properties is the use of suitable additives [Wang et al., 2000]. The additives can be broadly categorized into (1) polymeric additives such as poly(vinyl pyrrolidone) (PVP) and poly(ethylene glycol) (PEG), (2) weak nonsolvents such as glycerol, (3) weak cosolvents such as ethanol and acetone, and (4) low-molecular-weight inorganic salts such as lithium chloride (LiCl) and lithium perchlorate ($LiClO_4$) [Yeow et al., 2004]. The effects of these additives on the resulting PVDF membrane morphology have been reported. The additives tested to date include PVP [Deshmukh and Li, 1998], PEG [Feng et al., 2006], polystyrene sulfonic acid [Uragrami et al., 1980], ethanol [Shih, 1980], lithium chloride (LiCl) [Tomaszewska, 1996], and lithium perchlorate ($LiClO_4$) [Yeow et al, 2005]. The addition of PVP and PEG has been reported to favor macrovoid formation in the fabrication of PVDF membranes. However, difficulties arose in completely washing out the polymer additives from the membranes prepared. In contrast to polymer additives, small molecular inorganic additives can easily diffuse out during the membrane formation and washing process [Wang et al., 2000]. Lithium chloride is an interesting inorganic additive for membrane fabrication because it interacts strongly with certain solvents and can form complexes with the carbonyl groups in such solvents as dimethylformamide (DMF), dimethylacetamide (DMAc) and *N*-methyl-2-pyrrolidone (NMP) via the ion–dipole interaction. The strong LiCl–solvent interaction may result in a more favorable membrane morphology [Lee et al., 2002]. Therefore, LiCl was used as an additive in this study.

Microporous PVDF membranes are mainly prepared by controlled phase separation of polymer solutions via immersion precipitation. Thermodynamic studies, which can determine the phase separation data, and kinetic studies on the solvent evaporation in the dry process and the solvent–nonsolvent exchange in the polymer precipitation are essential to understand and control the membrane structures [Matsuyama et al., 2000]. As discussed before, there are some studies on the thermodynamics that had been carried out, but little work was reported on the kinetics of the phase separation.

The objective of this study was to evaluate the newly developed specialty PVDF materials by investigating thermodynamic and kinetics involved in membrane formation. The thermodynamics were studied by measuring the cloud points of the polymer solution systems. The kinetics experiments were carried out by determining the solvent evaporation rate from the membrane surface, the solvent-nonsolvent exchange rate and the additive leaching rate during the dry and wet steps of phase inversion. Filtration experiments were conducted as well to examine the effects of kinetics on the performance of microporous PVDF membranes.

3.2 Experimental

3.2.1 Materials and chemicals

Different grades of poly(vinylidene fluoride) (PVDF) (Kynar 741, 761, 461, 2851, and RC-10186) were provided by Arkema Inc. They were used after thorough drying at 70^{o}C for 48 h. N-methyl-2-pyrrolidone (NMP) purchased from Sigma-Aldrich Chemical was used as the solvent. Lithium chloride (LiCl) supplied by J. T. Baker Chemical was used as the additive. Deionized water was used as the nonsolvent.

3.2.2 Thermodynamic experiment: turbidimetric titration

The cloud points of polymer solutions provide the equilibrium phase separation data about polymer precipitation. They were determined at 25^{o}C by the turbidimetric titration method, which is illustrated in Figure 3.1.

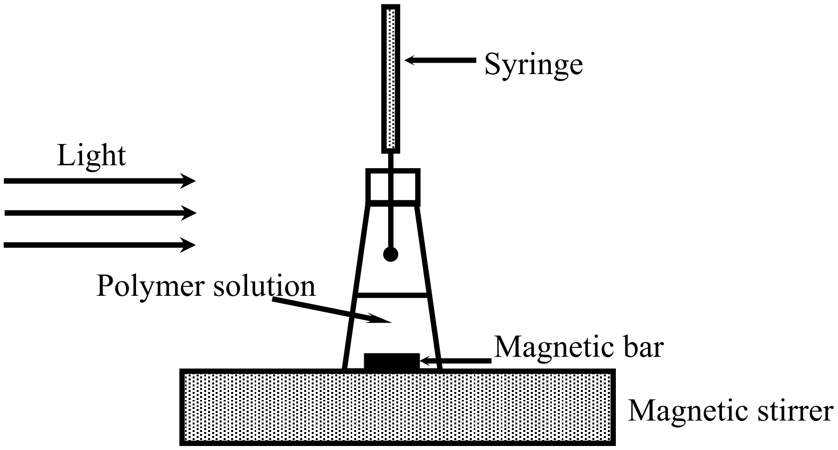

Figure 3.1 Schematic of turbidimetric titration setup.

The PVDF was dissolved in NMP at a predetermined concentration. When LiCl was added, it was dissolved in NMP before mixing with PVDF. The PVDF solution was titrated with deionized water (nonsolvent) using a 0.1-ml syringe until turbidity appeared. The turbidity was easily recognized by visual observation. During the titration procedure, the polymer solution was agitated with a magnetic bar. For polymer solutions with low viscosities, the cloud point for the titration was easy to determine. For polymer solutions with high viscosities, the mixing of the polymer solution and water was enhanced by heating the sample at an elevated temperature (60 – 80°C); if the turbidity was not observed after the sample was cooled down to 25°C, more water was added. To reduce solvent loss due to evaporation, small mouth glassware was utilized, and rubber septa were used to isolate the samples.

3.2.3 Kinetic experiment: solvent evaporation and polymer precipitation

a) Solvent evaporation experiment

The solvent evaporation data were obtained by measuring the change of the weight of cast films with time via an electronic analytical balance with an accuracy of ±0.001 g. The polymer solution with a predetermined composition was cast on a glass plate, and then the cast film and the glass plate, was put into an oven. Evaporation occurred under constant temperatures and constant air circulation.

b) Polymer precipitation

The kinetic data on the polymer precipitation were obtained by measuring the solvent-nonsolvent exchange rate and the additive (if present) leaching rate.

The film was cast onto a glass plate at room temperature. Then the film and the glass plate were put into a deionized water bath. A mixer was used to keep the concentrations of LiCl and solvent uniform in the water bath. The variation of LiCl concentration in the water bath was measured by monitoring the conductance of the water bath with an Inolab Conductivity Meter. The small amount of solvent present in the water bath did not affect the conductance of the bath. So the LiCl concentration in the water bath could be determined from the conductance readings.

To determine the solvent-nonsolvent exchange rate during the polymer precipitation, the change of solvent concentration in the gelation bath was measured with time using a Total Organic Carbon Analyzer (TOC-500, Mandel Scientific). The solvent concentration in the water bath could be determined from the TOC readings. A micro-syringe was used to take samples from the gelation bath.

3.2.4 Preparation of microporous membranes and filtration experiments

a) Microporous membrane preparation

The PVDF solution with a predetermined composition was cast onto a glass plate, and then the cast film and the glass plate were immediately put in an oven that provided a constant temperature and constant air circulation condition. After a certain period of time, the film and the glass plate were immersed into a deionized water bath (coagulation bath) and eventually the membrane was solidified. In order to remove the NMP solvent residues from the membranes completely, the membranes were kept in deionized water.

b) Filtration experiments

A flat sheet membrane cell system consisting of a peristaltic pump (Cole-Parmer, model 7553-80) and a solution reservoir was used to conduct the filtration experiments. All the microporous membranes were subjected to pure water pressurization under a pressure of 0.10 MPa for 1 h before the pure water permeation flux was determined.

The feed solution for filtration tests was aqueous Dextran (MW: 266,000) solution with a concentration of 1000 ppm. The feed solution was circulated through the feed side of the membrane cells for about 1 h at a flow rate of 10.4 L/h under a transmembrane pressure of 0.1 MPa. Both the permeate and the retentate were recycled to the solution reservoir. The concentrations of the feed and the permeate were measured using a Total Organic Carbon

Analyzer. The system was flushed completely with deionized water after each run. Figure 3.2 is the schematic of the filtration system.

The pure water permeation flux (J_{pwp}) was calculated by the equation 3.1:

$$J = \frac{V}{A \cdot \Delta t} \tag{3.1}$$

where V is the quantity of permeate, A is the membrane area, and Δt is the filtration time. The rejection rate (R_{rej}) is calculated by:

$$R_{rej} = \left(1 - \frac{C_p}{C_f} \right) \times 100\% \tag{3.2}$$

where C_p and C_f (ppm) are the Dextran concentrations of permeate and feed solutions, respectively.

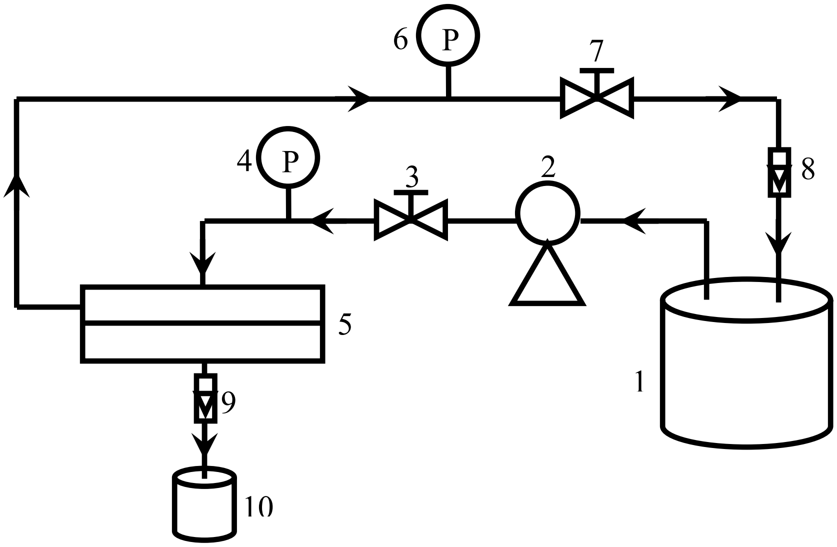

Figure 3.2 Schematic of filtration set-up.

1 solution reservoir; 2 peristaltic pump; 3, 7 valve; 4, 6 pressure gauge; 5 filtration cell; 8, 9 flow meter; 10 collector.

3.3 Results and discussion

3.3.1 Thermodynamics of polymer precipitation

The different PVDF solutions studied were comprised of NMP/PVDF/water with and without LiCl additives. Their equilibrium phase separation data are shown in Figures 3.3 – 3.7. It was very difficult to obtain homogeneous Kynar 461 solutions. The RC10186 solutions were more viscous than solutions of other grades of PVDF at the same concentrations, and it was difficult to get the equilibrium phase separation data at high concentrations (≥ 25 wt%).

As shown in Figures 3.3–3.5, the equilibrium phase separation data for Kynar 461, 2851 and RC10186 systems were found to shift towards the corners representing water when additive (LiCl) was added to the solutions. The shift of equilibrium phase separation data indicates that the presence of LiCl tended to enhance the affinity of the system to water and thus the water tolerance of the polymer solutions, which would decrease the solvent-nonsolvent exchange rate due to stronger salt/polymer interaction.

When the equilibrium phase separation data shifted away from the PVDF-solvent axis toward the water corner, the liquid-liquid demixing gap decreased and the polymer-lean phase was enhanced. During the polymer precipitation, the polymer-lean phase was nucleating and growing in the surrounding polymer-rich phase, which formed the solid structure of the membrane, while the polymer-lean phase lead to the porous structure [Ismail and Yean, 2003]. Occasionally, nucleated droplets of polymer-lean phase will grow into macrovoids, when the diffusive flow of solvents from the surrounding polymer solution into the nucleated droplets of polymer lean phase was greater than the diffusive flow of nonsolvent from the nucleated polymer lean phase to the surrounding polymer solution [Ismail and Yean, 2003]. However, the macrovoids, which are conical or spherical voids embedded within the membrane, are undesirable, because it results in mechanical weakness. Mechanical failures such as compaction or collapse of the membrane structure will occur when the membranes are under high-pressures [Zeman and Fraser, 1994; Lai et al., 1999]. Therefore, the addition of additive to Kynar 461, 2851 and RC10186 solutions might not be particularly suitable for membrane fabrication based on the thermodynamics.

Figures 3.6 and 3.7 show that the presence of LiCl did not have any significant impact on the equilibrium phase separation data for Kynar 761 and 741 solutions. This suggests that the interactions between LiCl and Kynar 761 and 741 were weak and the additive did not contribute significantly to the formation of membrane structure. The difference between the additive/polymer interactions perhaps resulted from the differences among the polymer chain structures. Compared to the other three materials, the homogenous regions of Kynar 741 and 761 solutions in the phase diagram were smaller and the liquid-liquid demixing gaps were larger. This implied that Kynar 741 and 761 solutions did not tolerate water as strongly as the other three polymers. This favors the formation of the polymer rich phase and helps reduce the polymer lean phase, which will enhance the mechanical strength of the membranes fabricated. Therefore, Kynar 761 and 741 are more suitable for membrane preparation.

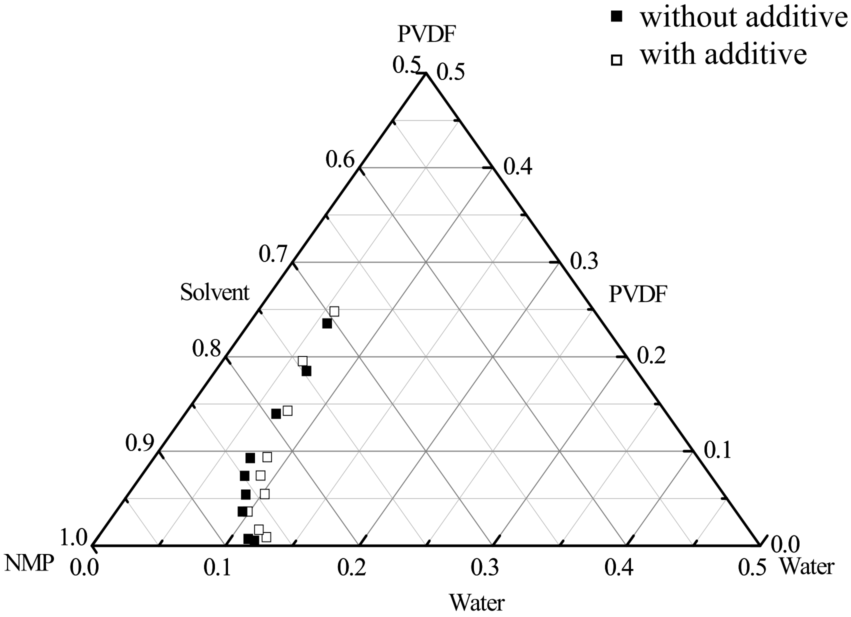

Figure 3.3 Phase diagram for PVDF (Kynar 461)/solvent (NMP)/water systems. Mass ratio PVDF:LiCl=5:1.

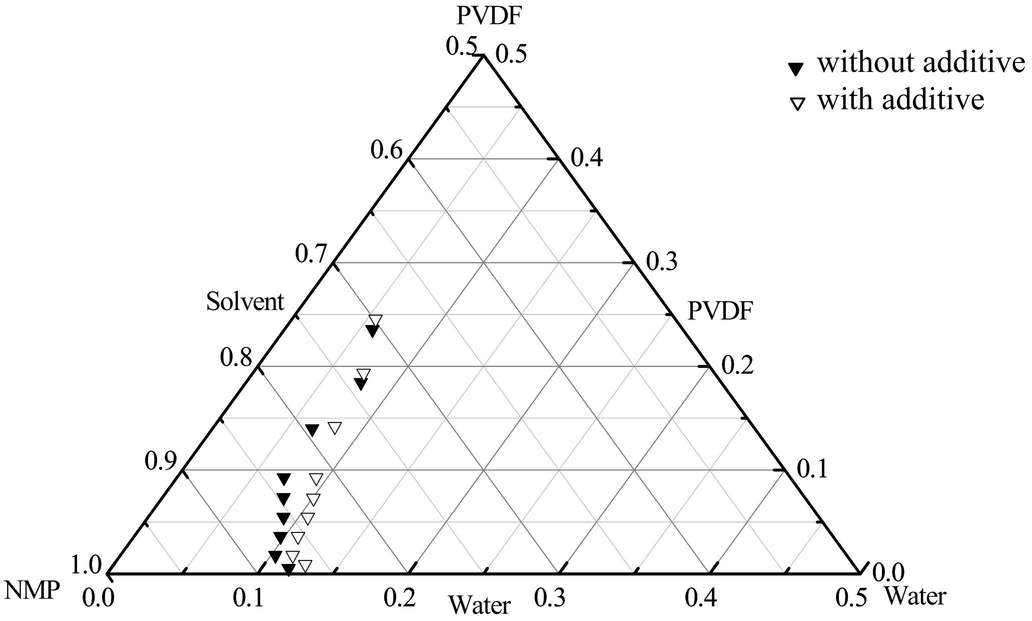

Figure 3.4 Phase diagram for PVDF (Kynar 2851)/solvent (NMP)/water systems. Mass ratio PVDF:LiCl=5:1.

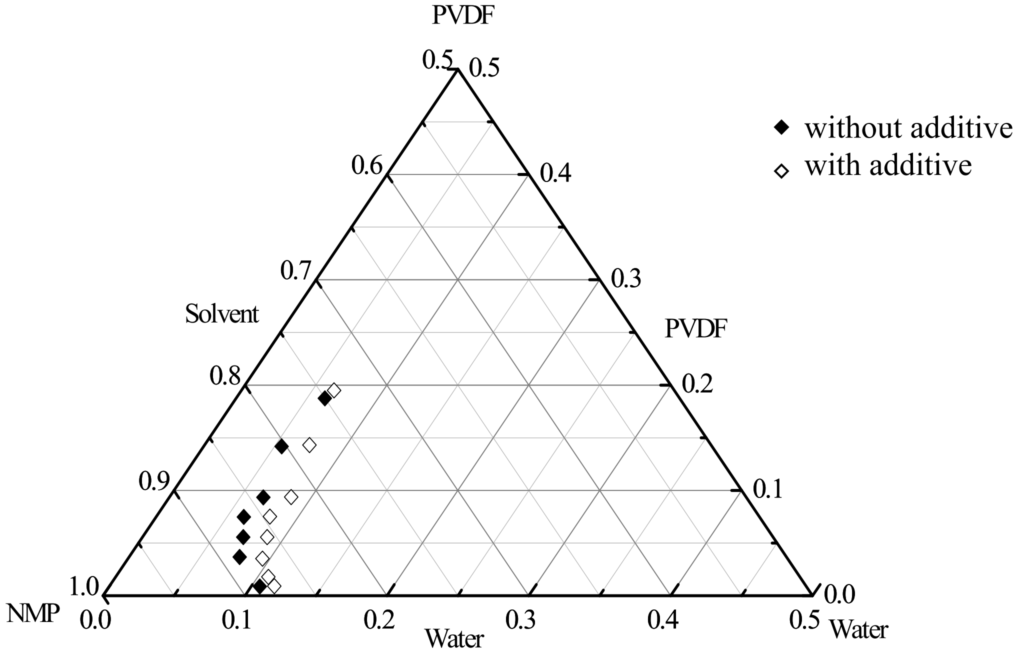

Figure 3.5 Phase diagram for PVDF (Kynar RC10186)/solvent (NMP)/water systems. Mass ratio PVDF:LiCl=5:1.

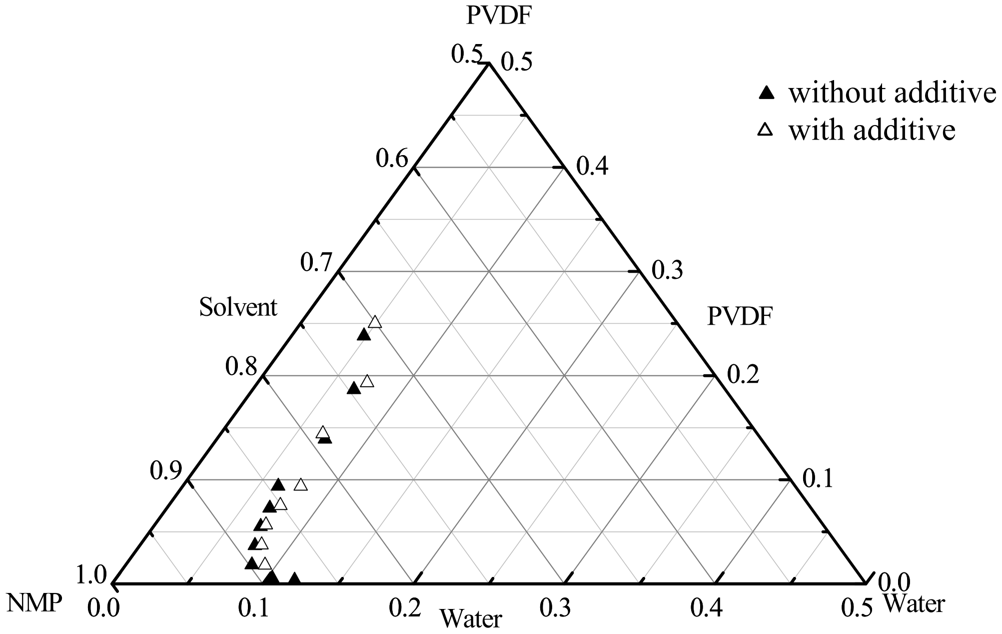

Figure 3.6 Phase diagram for PVDF (Kynar 761)/solvent (NMP)/water systems. Mass ratio PVDF:LiCl=5:1.

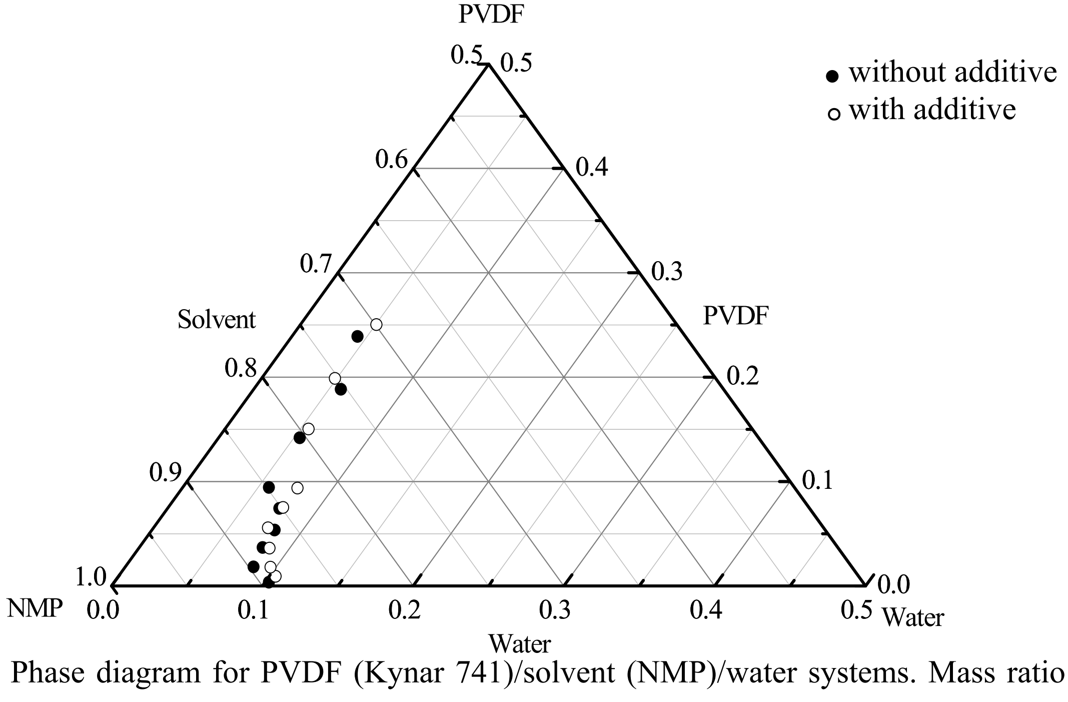

Figure 3.7 Phase diagram for PVDF (Kynar 741)/solvent (NMP)/water systems. Mass ratio PVDF:LiCl=5:1.

3.3.2 Kinetics pertinent to formation of microporous membranes

3.3.2.1 Kinetics of solvent evaporation

The development of membrane technology is to a large extent attributed to the invention of the asymmetric membrane. This membrane consists of a very thin, relatively dense skin layer supported by a more open porous sublayer, which provides the mechanical strength of the membrane, while the permeability and selectivity are governed by the skin layer [Castellari and Ottani, 1981]. Based on applications, the characteristics of a membrane (such as the thickness of the skin layer, the pore size and the pore size distribution of the pores and the thickness of the porous sublayer) can be tuned by adjusting the preparation conditions [Altinkaya and Ozbas, 2004]. Considering that partial solvent evaporation is involved in the dry/wet phase inversion process, an understanding of solvent evaporation in the early stage is important. In this study, the effects of film-casting thicknesses, casting temperatures, and types of PVDF materials on the solvent evaporation rate, which will influence the formation of the skin layer and the porous substrate, were investigated.

Figure 3.8 shows the relationship between solvent evaporation from cast films and the evaporation time. In the Figure, $(W_0 - W_t)/(W_0 - W_\infty)$ is a fraction representing solvent loss due to evaporation, with W_t being the weight of the cast film and the glass plate at time t, W_0 being the value of W_t at time $t=0$; and W_∞ being the value of W_t when the solvent was completely evaporated. The numbers in the legend mean PVDF grade (number code) - evaporation temperature (^{o}C) - thickness of cast films (μm). For example, 741-50-62 signifies solvent evaporation at 50^{o}C using Kynar 741 with a membrane thickness of 62 μm.

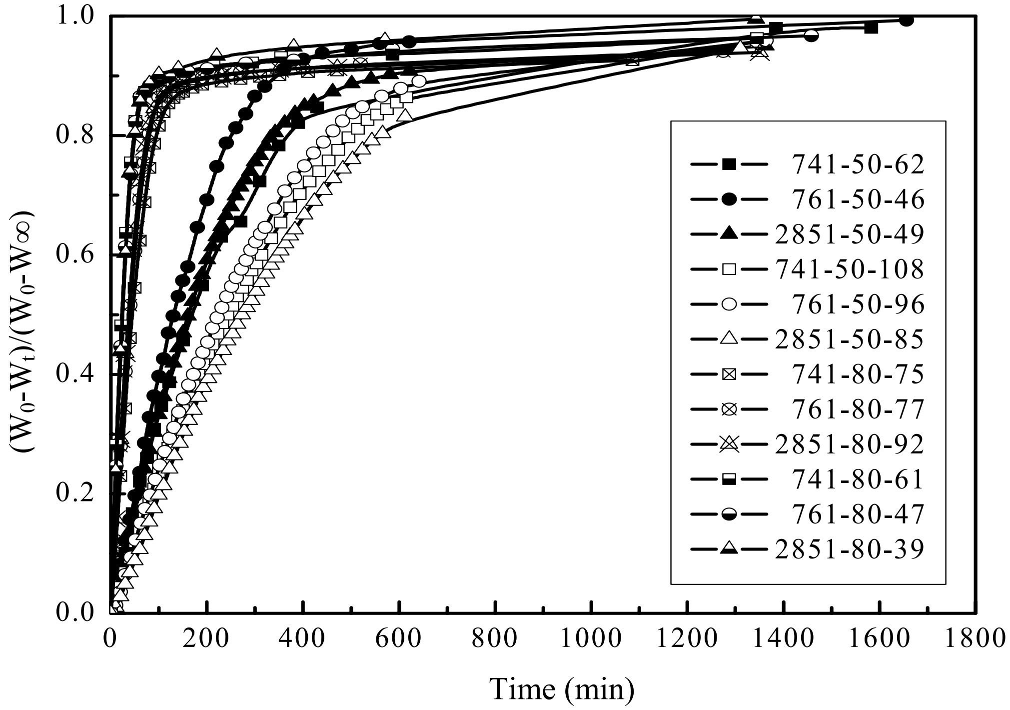

Figure 3.8 Experimental data on solvent evaporation at 50^{o}C and 80^{o}C. Composition of casting solution (wt%): PVDF:NMP:LiCl=18:3.6:78.4.

Based on the shape of the curves in Figure 3.8 and the model proposed by Krantz et al. [1986], the following postulations can be made. At time zero, a liquid/gas interface was created when a cast film was exposed to the gas phase. The solvent (initially at the concentration of dope solutions) began to evaporate into the gas phase. This lowered the solvent concentration (C_g) at the liquid/gas interface and caused diffusion of solvent to the interface from below, thus setting up a concentration profile shown in Figure 3.9. In the initial period, the solvent concentration in the liquid surface of cast film was much higher. As solvent evaporated, the solvent concentration of cast film decreased, and so did the concentration (C_g) of solvent at the liquid/gas interface. As a result, the driving forces for the solvent diffusion and evaporation decreased. Hence, the evaporation rate decreased as time went by. When the solvent concentration of the cast film dropped to a critical level, the film started to solidify [Huang and Feng, 1995], which would increase the mass transfer resistance within the film significantly. This is another reason for the sharp decrease in the evaporation rate. Figure 3.8 also shows that the cast film solidified faster when the evaporation temperature was higher. This was because the diffusion rate and evaporation rate of solvent were increased, and then the solvent loss from the film surface was compensated much faster by solvent diffusion from the film interior to the surface.

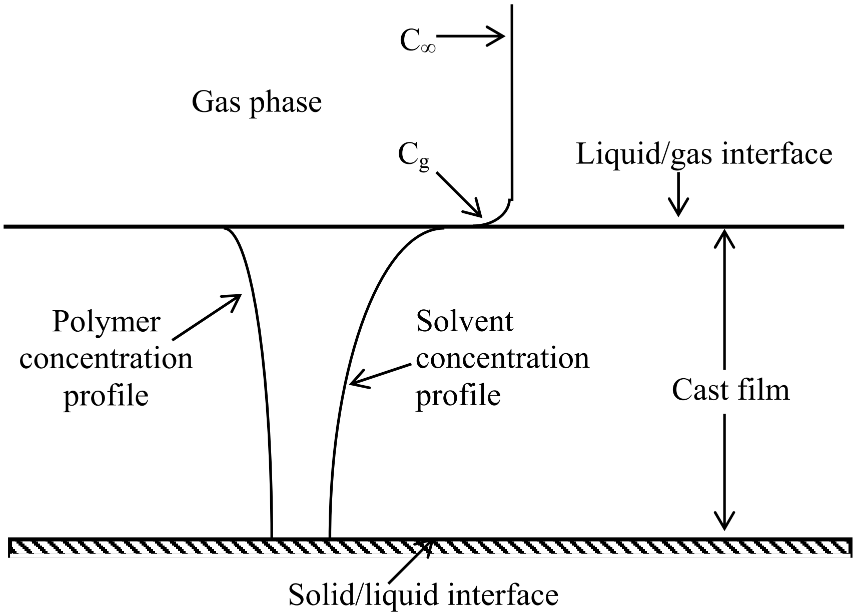

Figure 3.9 Schematic of solvent evaporation from a cast film [Krantz et al., 1986].

In order to describe the evaporation rate quantitatively, an empirical equation proposed by Huang and Feng [1995] is used to investigate the kinetic behavior of solvent evaporation under different circumstances (different types of polymer solution, different evaporation temperatures and different thicknesses of the cast film),

$$\frac{W_0 - W_t}{W_0 - W_\infty} = 1 - \exp(-bt^{\mathrm{m}}) \tag{3.3}$$

where *b* and *m* are two empirical parameters. From equation 3.3, the following equation was developed by Huang and Feng [1995],

$$log[-ln(\frac{W_t - W_\infty}{W_0 - W_\infty})] = m\, log\, t + log\, b \tag{3.4}$$

which suggests a linear relationship between $log[-ln(\frac{W_t - W_\infty}{W_0 - W_\infty})]$ and *log t* with a slope of *m* and an intercept of *log b*. This is shown in Figure 3.10. It is of practical interest to quantify solvent evaporation at the early stage of the membrane formation. The linear parts in Figure 3.10 indicate that equation 3.3 is valid to describe the solvent evaporation for PVDF membrane preparation by the dry/wet phase inversion method.

Castellari and Ottani [1981] proposed that the mass transfer within the cast film for the evaporation step was the combination solvent diffusion and polymer contraction. The mutual diffusion coefficient for the solvent-polymer system depended on temperature and molecular weight [Resi et al., 2005]. The temperature dependence of diffusion coefficient was demonstrated by Figures 3.8 and 3.10. Both figures illustrate that an increase in the evaporation temperature will increase the solvent evaporation rate from the gas/liquid interface significantly due to the increase of solvent diffusion rate within the cast film. Further discussion about the role of the solvent evaporation in the membrane preparation will be addressed later.

The thickness of the cast film also had an impact on the solvent evaporation rate. As shown in Figures 3.8 and 3.10, the solvent evaporated faster from thinner films, and it took a shorter period of time for the film to start solidification. The types of polymer did not seem to influence the solvent evaporation, implying that the difference among these new PVDF polymers was insignificant as far as solvent evaporation was concerned.

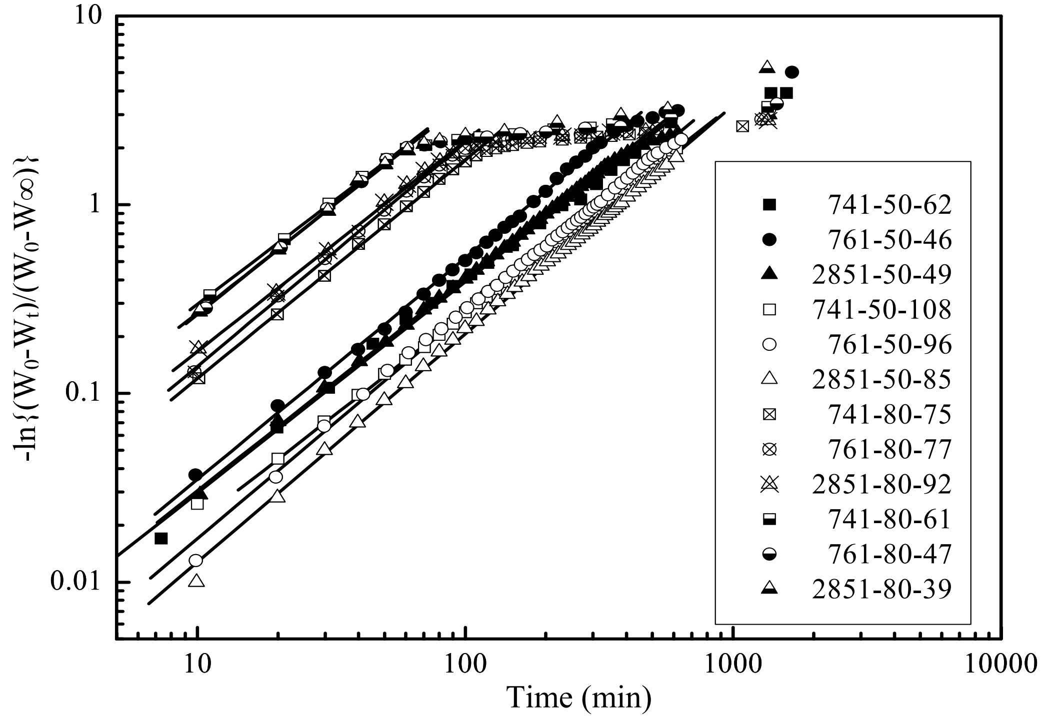

Figure 3.10 Logarithmic plot of $-ln\{(W_0 - W_t)/(W_0 - W_\infty)\}$ vs time for the data shown in Figure 3.8.

The effects of evaporation temperature and film thickness can also be evaluated by the empirical parameters: *m* and *b*, whose numerical values are given in Table 3.1. It is found that the values of *b* tends to increase when the evaporation temperature is raised and/or the thickness of cast film is decreased. This means that the sooner the solvent loss reaches the critical point for film solidification to occur, the higher the value of *b* [Huang and Feng, 1995]. However, the parameter *m* is not influenced by the evaporation temperature, the thickness of cast film or the type of the polymer. *m* might be a parameter related to the type of solvent or the polymer solution concentration. Hence, further investigation on parameter *m* is necessary, in order to obtain a clearer understanding about how the evaporation process affects the membrane formation.

Table 3.1 Empirical parameters *m* and *b* under different conditions.

Membrane	*m*	*b* (min^{-m})
741- 50 - 62	1.12	2.26-e3
761-50 - 46	1.17	2.34-e3
2851-50- 49	1.13	2.28-e3
741- 50-108	1.11	1.63-e3
761- 50 - 96	1.20	1.08-e4
2851-50 -85	1.21	7.90-e4
741- 80 - 75	1.16	8.28-e3
761- 80 - 77	1.19	9.04-e3
2851-80 -92	1.12	1.28-e2
741- 80 - 61	1.08	2.49-e2
761- 80 -47	1.15	1.86-e2
2851-80 -39	1.12	2.02-e2

3.3.2.2 Kinetics of polymer precipitation

The dynamics of wet phase inversion were characterized by the solvent-nonsolvent exchange rate and the additive leaching rate, which could give information concerning the development of morphology and the structure of the membrane. Faster solvent-nonsolvent exchange and additive leaching rates are an indication of porous structure of the membrane, and a sharp decrease in the rate with time is an indication of structural gradient in the membrane [Huang and Feng, 1995].

The solvent-nonsolvent exchange rate and the leaching rate of additive LiCl from the cast polymer film was determined by measuring the concentration of solvent and additive in the coagulation bath. For easy comparison, the relative concentration (C_t/C_∞) was used, where C_t and C_∞ denote the concentrations of the solvent or additive in coagulation bath at time *t* and at infinite time, respectively. It should be pointed out that after being immersed in the coagulation bath, the cast film soon peeled off from the glass plate, then the solvent-nonsolvent exchange and the additive leaching started on both sides of the film.

As illustrated in Figures 3.11 and 3.12, the solvent-nonsolvent exchange rate and LiCl leaching rate were high in the early stage of polymer precipitation and then slowed down. The reasons are: 1) as solvent diffused and LiCl leaches from the gelled polymer layer, the concentration differences of both NMP and LiCl between the gelled polymer layer and gelation bath decrease. Because of the reduced driving force, the solvent-nonsolvent exchange rate and LiCl leaching rate decrease; 2) the mass transfer resistance to solvent-nonsolvent exchange and LiCl leaching increase with the formation of gelled polymer layer during the polymer precipitation [Liu, 2003].

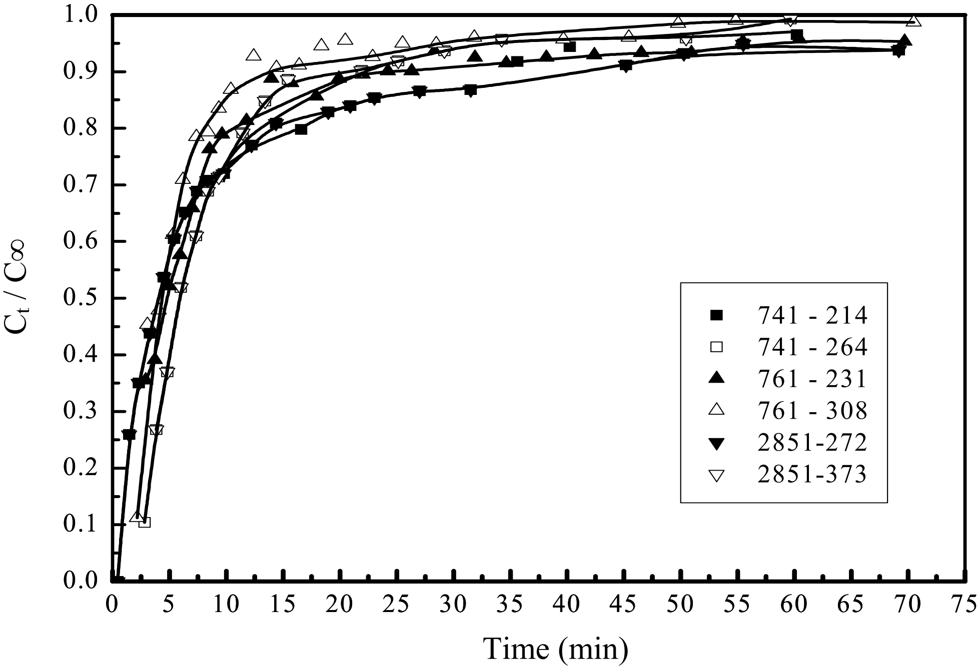

Figure 3.11 Solvent-nonsolvent exchange curve during polymer precipitation.

Composition of casting solution (wt%), PVDF:NMP:LiCl=18:3.6:78.4. Nonsolvent, water. Temperature, 20°C. The numbers in the legend mean PVDF grade-thickness of cast films (μm). For example, 741-214 means Kynar 741 and film thickness 214 μm.

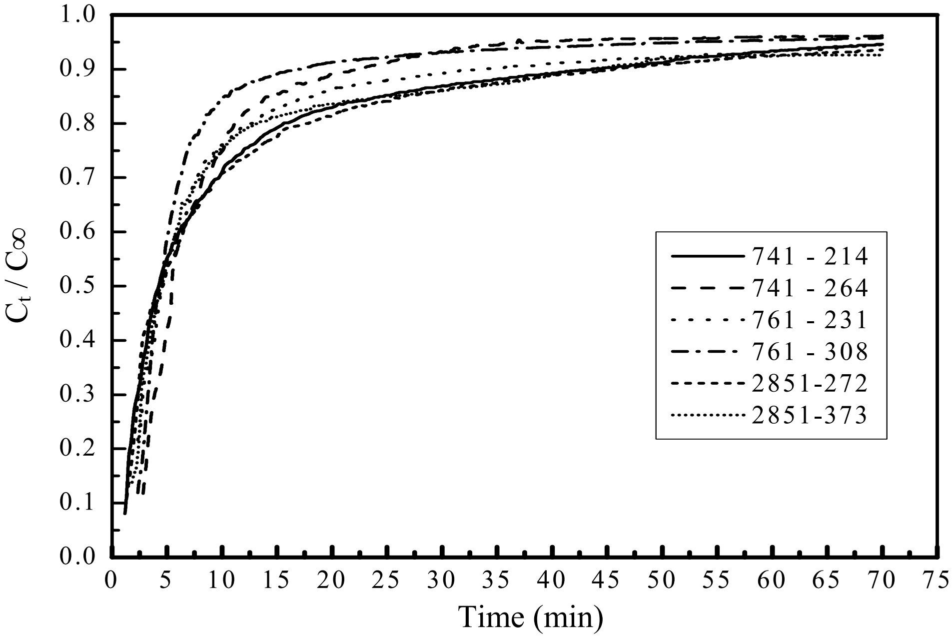

Figure 3.12 Leaching rate of LiCl during polymer precipitation. Experimental conditions were the same as those shown in Figure 3.11.

There were "time lags" in the nonsolvent and solvent exchange and the LiCl leaching processes at the early stage of the phase inversion. There are two possible reasons for the existence of the "time lag". Firstly, the locations for taking coagulation solution samples and the probe (dip-cell) for conductance measurement were not exactly on the membrane surface, so it took time for NMP and LiCl molecules to leach from the film and reach that location [Huang and Feng, 1995]. Another reason is that the "time lag" corresponding to the interval between initial polymer/nonsolvent contact and the time t_o, at which the solvent first diffuses through the skin (which may be regarded as the diffusion layer) into the nonsolvent region [Patsis and Henriques, 1990]. However, although the concentrations measured were not the actual concentrations at the film surface, the curves are still valid to show the qualitative trends because the probe was fixed at a given position near the film surface.

A mathematical model was developed by Patsis and Henriques [1990] for the formation of membranes by immersion precipitation method based on the following assumptions:

1) Only the solvent and nonsolvent diffusion perpendicular to the film surface need to be considered;

2) Initial skin formation results almost exclusively from diffusion of water into the system;

3) A quasi-stationary diffusion state is established almost instantaneously;

4) The pores, which control diffusion of solvent and nonsolvent, are those closest to the polymer/nonsolvent interface;

5) Nonsolvent volume remains essentially constant.

The following equation was proposed [Patsis and Henriques, 1990],

$$C_t = \frac{\sqrt{2}AC_oD_s}{V\sqrt{\alpha_1\widehat{C}_{ns}D_{ns}}}\cdot t^{0.5} - \frac{\sqrt{2}AC_0D_s}{V\sqrt{\alpha_1\widehat{C}_{ns}D_{ns}}}\cdot t_o^{0.5} \qquad (3.5)$$

where D_{ns} is the diffusion coefficient of nonsolvent, D_s is the diffusion coefficient of the solvent, α_1 is termed the "compaction factor" describing the level of polymer film contraction after the precipitation, C_o is the initial mole fraction of solvent on the surface of the film, C_t is the mole fraction of solvent in the coagulation bath at time t, $\widehat{C}_{ns}$ represents the concentration of pure nonsolvent, A is the area of the film, V is the fixed volume of nonsolvent into which the solvent diffuses, t_o is the lag time that is the time at which the solvent first diffuses into the nonsolvent region.

In our experiment, additive was added to the solution. After the membrane was immersed in the gelation bath, the solvent-nonsolvent exchange and the additive leaching began to occur on both sides of the cast film. The concentrations (C_∞) of the solvent or the additive in the coagulation bath at infinite time could be determined easily. Hence, by replacing the term C_o with C_∞, the following equation was obtained

$$C_t / C_\infty = \frac{\beta A D_m}{V\sqrt{\alpha_1 \widehat{C}_{ns} D_{ns}}} \cdot t^{0.5} - \frac{\beta A D_m}{V\sqrt{\alpha_1 \widehat{C}_{ns} D_{ns}}} \cdot t_o^{0.5} \tag{3.6}$$

where D_m is the diffusion coefficient of the small molecules (i.e., solvent and additive), β is a parameter accounting for the concentration term.

Equation 3.6 suggests that a plot of C_t / C_∞ versus $t^{0.5}$ will yield a straight line, and this is shown in Figures 3.13 and 3.14. It can be found that the concentrations of small molecules (i.e., solvent and additive) had a linear relationship with the square root of time ($t^{0.5}$) up to 85% of the precipitation process, which indicates that the mass transfer process in the cast film was indeed diffusion controlled during the wet phase inversion process.

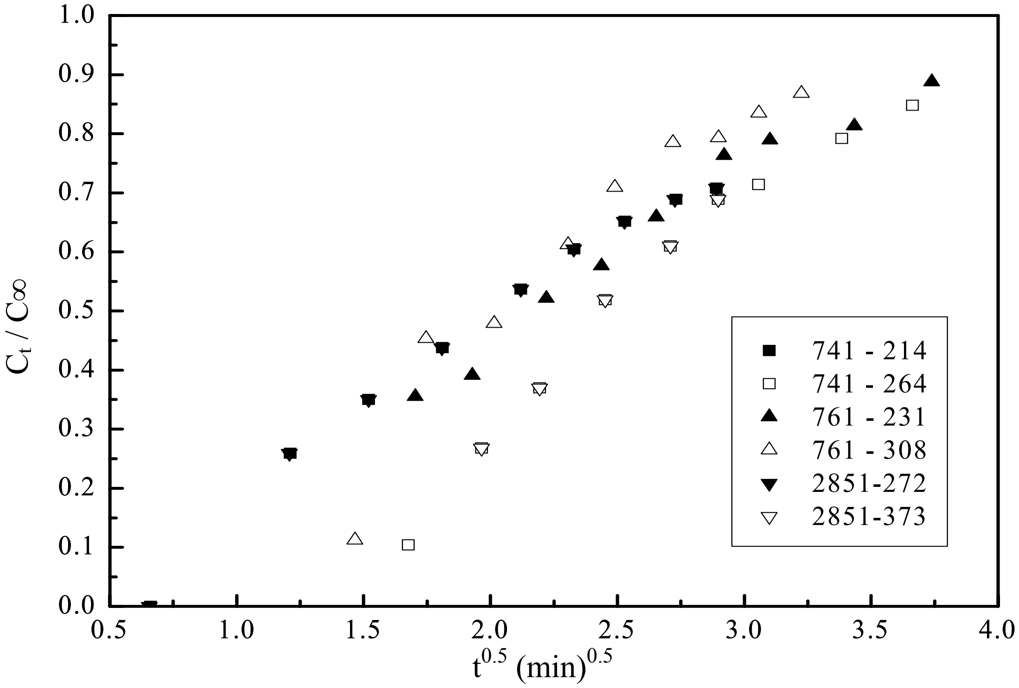

Figure 3.13 Solvent concentration in the coagulation bath vs. square root of time. Experimental conditions were the same as those shown in Figure 3.11.

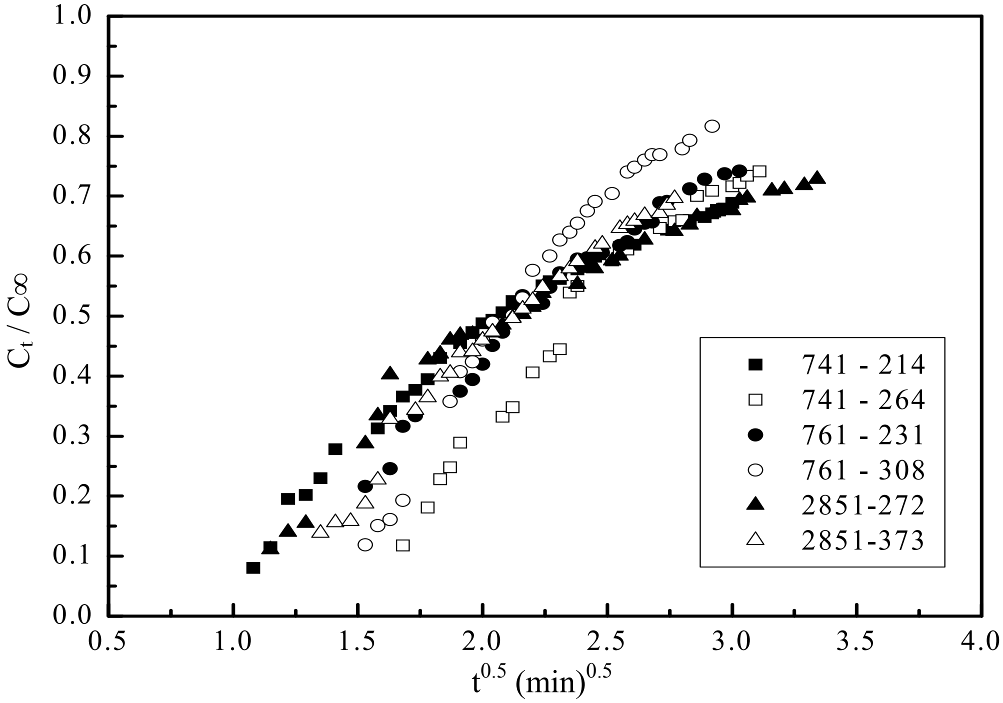

Figure 3.14 Concentration of LiCl in the coagulation bath vs. square root of time. Experimental conditions were the same as those shown in Figure 3.12.

The slopes of the lines in Figures 3.13 and 3.14 for solvent-nonsolvent exchange and LiCl leaching are listed in Tables 3.2 and 3.3, respectively. It is very clear that the value of the slope is higher when the film cast from same polymer solution is thicker. It can be explained as following: when the cast film is thicker, more sponge-like structure in the membrane will be developed. Therefore, the "compaction factor" α will be lower, resulting in a larger value of slope. On the other hand, when the cast film is thinner, macrovoid-like porous structure will be fully developed, and the "compaction factor" α is higher, which tends to reduce the slope.

As discussed before, the slopes of cast films with approximately same thicknesses should not be affected by the polymer types, because the molecular weight of the polymer does not affect the mutual diffusion coefficient significantly. However, because water and additive LiCl were involved in the phase inversion processes, the diffusion of small molecules (i.e., solvent and LiCl) will be different. The numerical values of the slopes show that the LiCl leaching and the solvent-nonsolvent exchange in different polymer solutions are rather different. For Kynar 761, the solvent-nonsolvent exchange rates were lower than the LiCl leaching rates. For Kynar 741, the solvent-nonsolvent exchange and additive leaching rates were not much different. For Kynar 2851, the solvent-nonsolvent exchange rates were higher than the LiCl leaching rates. These indicate that the polymers-solvent interactions and polymer-additive interactions are different for different PVDF polymers, presumably due to their different structures. This agrees with the findings from the thermodynamic investigation. It should be pointed out that the values of the slopes for membrane 741-264 precipitation (solvent: 0.38; LiCl, 0.43) are higher than the values of membrane 2851-272 precipitation (solvent 0.31; LiCl 0.26). This means that the solvent nonsolvent exchange and LiCl leaching occurred more rapidly in Kynar 741 solutions than in Kynar 2851 solutions. This can be attributed to the fact that Kynar 2851/NMP solutions have better tolerance to water, especially when LiCl was present in the solutions. This supports the conclusions that were drawn in the previous thermodynamic study. A further analysis of the effects of polymer structure on the interactions which needs detailed knowledge of the polymer structures will be carried out by Arkema Inc.

It is also noted in Figures 3.13 and 3.14 that the straight lines all intersect with the $t^{0.5}$ axis due to the existence of lag time as discussed before. The lag time for each polymer precipitation process is given in Tables 3.2 and 3.3. It shows that the thicker the membranes, the longer the lag time. Clearly, this agrees with physical reasoning that the mass transfer resistance to solvent-nonsolvent exchange and LiCl leaching is bigger in thicker films. The solvent-nonsolvent exchange has a shorter lag time than the LiCl leaching for Kynar 761, while the opposite is observed for Kynar 2851. For Kynar 741, the lag times for the solvent-nonsolvent exchange and the additive leaching are not very different. These also indicate that the polymers-solvent interactions and polymer-additive interactions are different for different PVDF polymers, presumably due to their different structures. It should be pointed out that the lag times for membrane 741-264 precipitation (solvent: 1.5 min; LiCl, 1.6 min) were higher than the values of membrane 2851-272 precipitation (solvent 0.22 min; LiCl 0.090 min). This is because Kynar 2851 solutions have a better affinity to water, especially when

LiCl was present in the solutions. Therefore, the solvent-nonsolvent exchange and LiCl leaching from the film can be initiated easily.

Table 3.2 Slopes of linear fitting and lag time for solvent-nonsolvent exchange.

Membrane	Slope ($\min^{-0.5}$)	Lag time (min)
741 - 214	0.31	0.23
741 - 264	0.38	1.5
761 - 231	0.28	0.13
761 - 308	0.39	0.67
2851-272	0.31	0.22
2851-373	0.46	1.9

Table 3.3 Slopes of linear fitting and lag time for LiCl leaching from the cast film.

Membrane	Slope ($\min^{-0.5}$)	Lag time (min)
741 - 214	0.29	0.24
741 - 264	0.43	1.6
761 - 231	0.35	0.61
761 - 308	0.52	1.4
2851-272	0.26	0.090
2851-373	0.40	0.83

3.3.3 Formation of microporous membranes

The selectivity of microporous membrane is offered by the skin layer, which also governs the membrane permeability. The formation of skin layer is affected by solvent evaporation and polymer precipitation, and so the permeability and selectivity of microporous membranes can be tuned by controlling the evaporation and precipitation conditions.

The permeability and selectivity of microporous membranes were characterized by pure water permeability (J_{PWP}) and Dextran 266,000 rejection rate (R_{rej}), respectively. Figures 3.15 to 3.18 illustrate that the membrane selectivity increases and the permeability decreases with an increase in the partial evaporation temperature and time. When the solvent evaporation time is long enough, the membrane permeability decreases substantially because of the dense structure of the membrane formed. The membrane produced will have a high selectivity. In fact, dense films are prepared conventionally by complete evaporation of the solvent from the cast film.

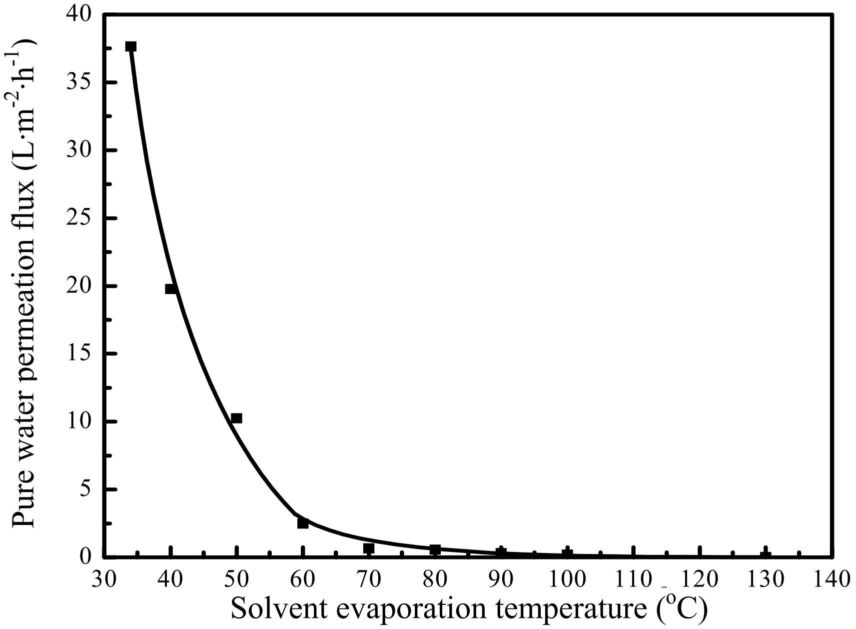

Figure 3.15 Effect of partial evaporation temperature on membrane permeability. Evaporation time 15 min.

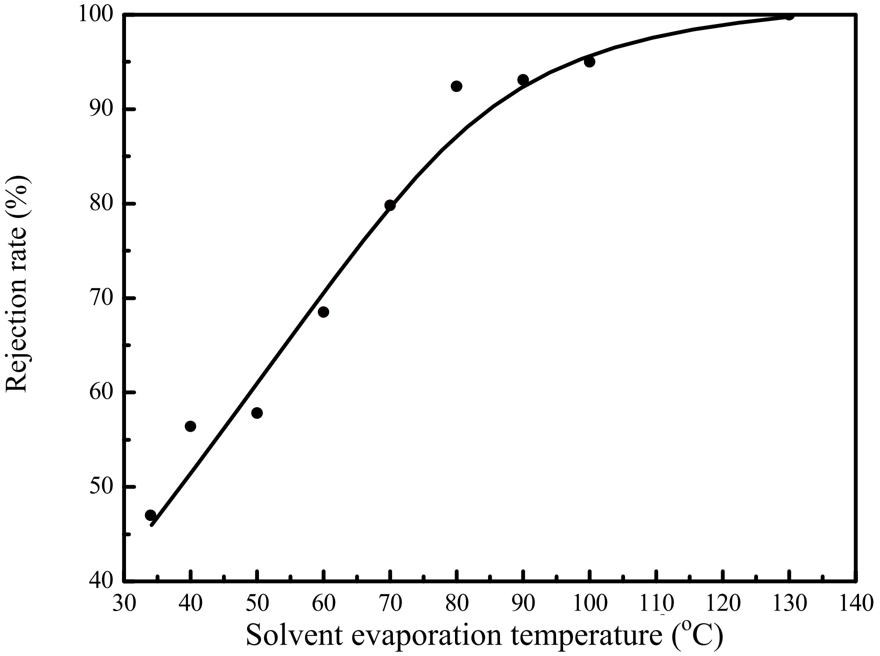

Figure 3.16 Effect of partial evaporation temperature on membrane selectivity. Evaporation time 15 min.

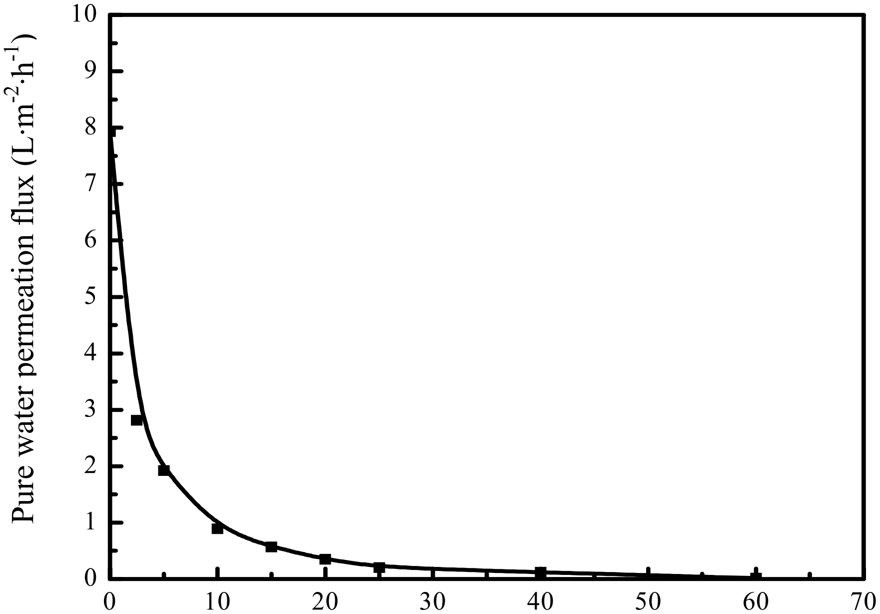

Figure 3.17 Effect of partial evaporation time on membrane permeability. Solvent evaporation temperature 80°C.

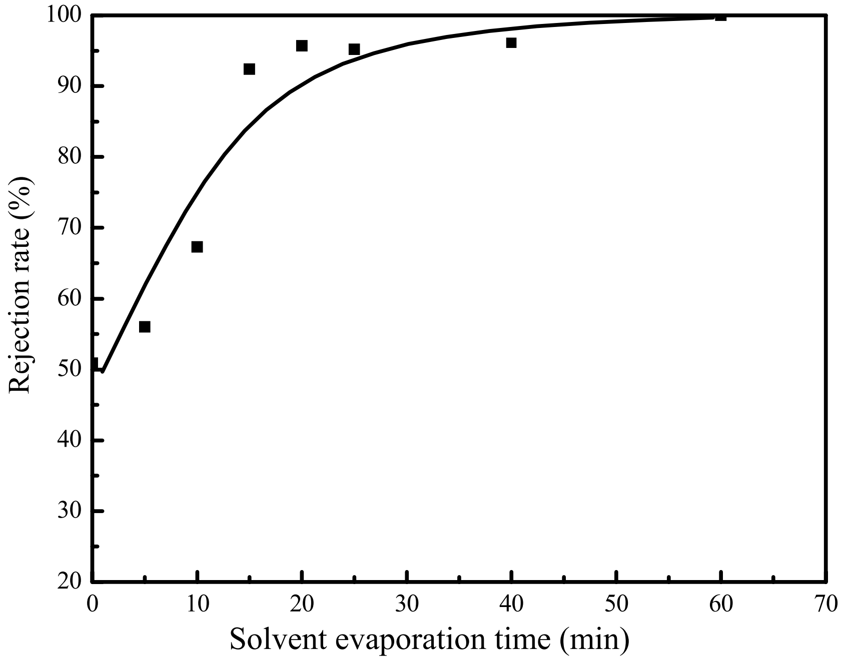

Figure 3.18 Effect of partial evaporation time on membrane selectivity. Solvent evaporation temperature 80°C.

As discussed in section 3.3.2.1, the polymer concentrations at the surface and in the bulk of the cast film increases with time during solvent evaporation. Due to the solvent evaporation, the polymer concentration at the surface is higher than in the bulk. A higher evaporation temperature, after partial evaporation of the solvent, also results in a higher polymer concentration on the film surface. When the cast film is placed into the gelation bath for polymer precipitation, the polymer rich phase becomes more concentrated and polymer lean phase tends to be leaner. This would lead to a denser skin layer as well as smaller pores and a lower porosity in the sublayer.

The impacts of solvent evaporation on membrane permeability and selectivity were also investigated for polyetherimide from a kinetic perspective by Huang and Feng [1995]. It was reported that the gelled polymer layer, which formed immediately at the interface between the film and the gelation medium right after the cast film contacted with the gelation bath, formed the skin layer. The gelled polymer layer also acts as a barrier to the solvent-nonsolvent exchange and LiCl leaching. A denser gelled polymer layer limited the solvent-nonsolvent exchange rate, which causes a denser sublayer.

3.4 Conclusions

The equilibrium phase separation diagrams for PVDF/NMP/water system with and without LiCl were determined. Studies on solvent evaporation in the dry "step" and the solvent-nonsolvent exchange and the additive leaching during polymer precipitation were also carried out. The following conclusions can be drawn:

The thermodynamic stability of the polymer solution was influenced by the type of polymer. The effects of LiCl on the thermodynamic stability depended on the type of the polymer solutions. The addition of LiCl to Kynar 461, 2851 and RC 10186 solutions enhanced the water tolerance and the thermodynamic stability of the solutions, but there was no significant impact on the thermodynamic stability of the polymer solutions containing Kynar 761 and 741.

The solvent evaporation in the early stage was described quantitatively. It was demonstrated that the evaporation temperature and the film-casting thickness affected the solvent evaporation rate significantly; however, the type of PVDF did not affect the solvent evaporation rate. The polymer precipitation studies showed that the mass-transfer involved in the additive leaching and solvent-nonsolvent exchange during the precipitation process was diffusion controlled, and the type of PVDF did have impacts on the precipitation kinetics. By controlling the solvent evaporation and polymer precipitation conditions, microporous membranes with certain permeability and selectivity could be prepared by the dry/wet phase inversion method.

Chapter 4

Fabrication of PVDF hollow fiber membranes

4.1 Introduction

Hollow fiber membranes have three major advantages over flat sheet membranes: 1) hollow fibers have much larger ratio of membrane area to volume, and hence higher productivity per unit volume of membrane module; 2) they are self-supporting, which can be back-flushed for liquid separation; 3) they have good flexibility in operation [Chung, 2000]. A lot of studies have been performed to improve the properties of PVDF membranes, but most of the work is limited to the flat sheet membranes prepared by the wet phase inversion method or the dry/wet phase inversion method. There is a need to study the fabrication of PVDF hollow fiber membranes. The preparation of hollow fiber membranes is a complicated process involving various parameters (e.g. dope extrusion rate, air gap, take-up speed, nature of the internal and external coagulants, internal coagulant flow velocity, etc.), which are expected to affect the properties of fabricated membranes [Khayet et al., 2002]. Another problem encountered during hollow fiber fabrication is related to the viscosity of the spinning solution. Dilute polymeric solutions can be cast on a flat support surface to form a flat membrane with mechanical integrity. A relatively high viscosity is often required during hollow fiber spinning, because the nascent fiber is retained as a result of the solution viscosity, and the formation of unstructured macrovoid in the fiber walls needs to be eliminated [Cabasso et al., 1976]. On the other side, a high viscosity will restrict the mass transfer kinetics during the polymer precipitation. There are two approaches that may be employed to adjust and/or control the viscosity of a polymer solution: 1) control the molecular weight of the polymer or the polymer concentration of the dope solution; 2) use suitable solvents based on the solubility data. In addition, in some cases, to add additive into the spinning solution can affect the viscosity of the casting solution [Liu, 2003].

In this study, the specialty PVDF materials (Kynar 741, 2851, 761 and RC10214) newly developed by Arkema were employed to fabricate hollow fiber membranes using the dry/wet phase inversion method with or without additive LiCl. The effects of spinning parameters (i.e., dope extrusion rate, internal coagulant flow velocity and take-up speed) on the dimension and morphology of the hollow fiber membranes were investigated.

4.2 Experimental

4.2.1 Materials and chemicals

PVDF polymers (Kynar 741, 2851, 761, and RC10214) were provided by Arkema. They were used after thorough drying in vacuum at 70°C for 48 h. Reagent grade isopropanol was supplied by the Chemistry Store at University of Waterloo. Nitrogen gas was supplied by Praxair Inc.

4.2.2 Fabrication of PVDF hollow fiber membranes

To prepare PVDF solutions, a predetermined amount of NMP and PVDF were mixed in a 1-liter flask. When LiCl was used as an additive, it was dissolved in NMP first before being mixed with PVDF. The solutions were heated to 60°C to facilitate the dissolution of polymer. During this process, the flask was sealed to eliminate the solvent loss. Then the PVDF solution was transferred into a stainless steel dope tank and kept in the tank for ca. 36 h to remove the air bubbles entrapped in the solution.

All hollow fiber membranes were fabricated via the dry/wet phase inversion method. The fabrication equipment is illustrated in Figure 4.1. The dope extrusion rate was controlled by the pressure of pressurized nitrogen gas. The internal coagulant was delivered to the centre tube of the spinneret (size: 1.0/0.5 mm OD/ID) with a high precision metering pump. This is shown in Figure 4.2. The inner wall of the nascent fiber was solidified by the internal coagulant. The spinneret was installed above the coagulation bath so the solvent could partially evaporate from the outer wall of the fiber in air before entering the external coagulant bath. Then the solvent-nonsolvent exchange occurred on the outer wall of the fiber, and asymmetric hollow fiber membrane was obtained. During the coagulation, most of the LiCl leached out of the fiber. However, in order to remove the LiCl and the NMP residues completely, the membranes were kept in deionized water bath for at least 7 days. Finally, the membranes were dried at ambient conditions.

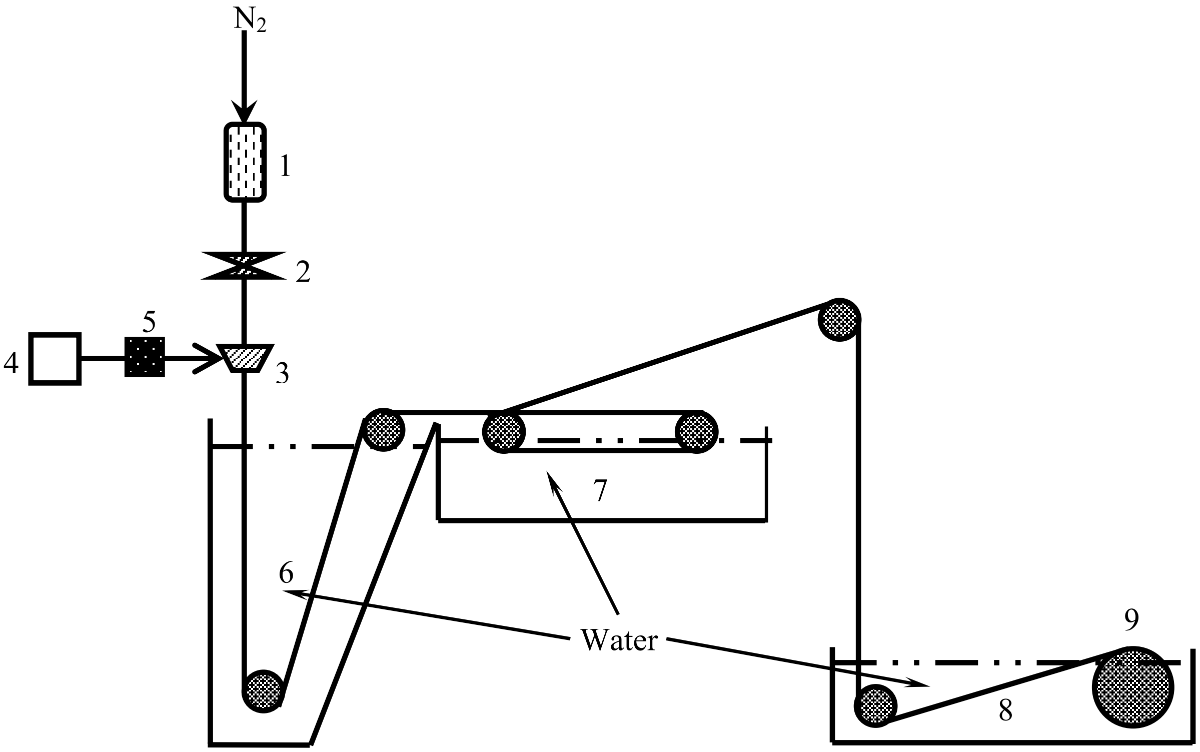

Figure 4.1 Schematic of a dry-wet spinning process.

1 solution tank; 2 dope solution filter; 3 spinneret; 4 internal coagulant tank; 5 high precision metering pump; 6 external coagulation bath; 7 washing bath; 8 fiber collecting bath; 9 fiber take-up drum.

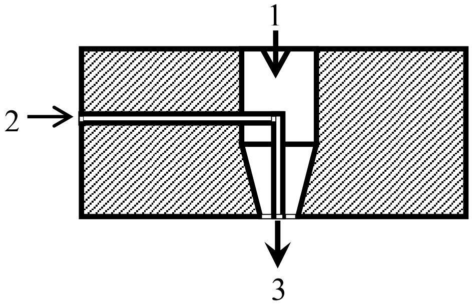

Figure 4.2 Schematic structure of the tube-in-orifice spinneret.

1 dope solution entry port; 2 internal coagulant entry; 3 extrusion orifice.

4.2.3 Characterization of hollow fiber membranes

The inner and outer diameters of the fibers were measured with a microscope (Cole-Parmer, Model 3894).

The average pore size and the other structural parameters were determined with the gas permeation method. The pore size distribution was determined by the gas-liquid displacement method recently developed in our lab.

The gas permeation method: The membrane modules were assembled with dried hollow fibers, as shown in Figure 4.3. One end of the hollow fiber was sealed with epoxy, and the other end was open. The gas permeation experiments were carried out at room temperature. Nitrogen was fed to the shell side of the module at given pressures. Figure 4.4 illustrates the schematic of the set-up. The pressure of permeate side was 1 atm. The nitrogen permeation rate was determined with a bubble flow meter. The permeance data were used to determine the mean pore size and the effective porosity based on the discussion made in 2.3.1.

The gas-liquid displacement method: the experimental set-up for gas-liquid displacement was essentially the same as the one used for gas permeation experiment. The hollow fibers were soaked in isopropanol which filled the pores of the fiber walls due to the capillary force. Nitrogen was fed to the bore side to displace the isopropanol and the gas pressure was increased stepwise with an increment of around 5 psi. The gas flow rates through the fully open pores at different pressures were measured. All the pores were considered to be opened when the permeance increased linearly with an increase in the pressure differential across the membrane. Each run was completed within 30 min to minimize the membrane swelling caused by isopropanol.

To investigate the morphology of the hollow fiber membranes, the membranes were examined with a Scanning Electron Microscope (Jeol JSM 6460). To prepare the membrane samples for examination under SEM, the membranes were immersed in liquid nitrogen and fractured. After sputter coating with gold, the membrane samples were examined.

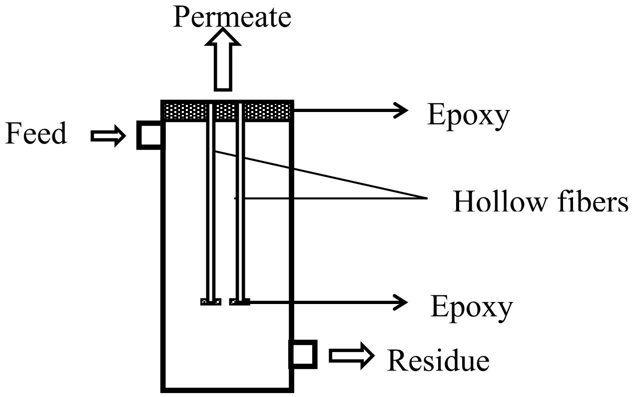

Figure 4.3 Schematic of a hollow fiber module.

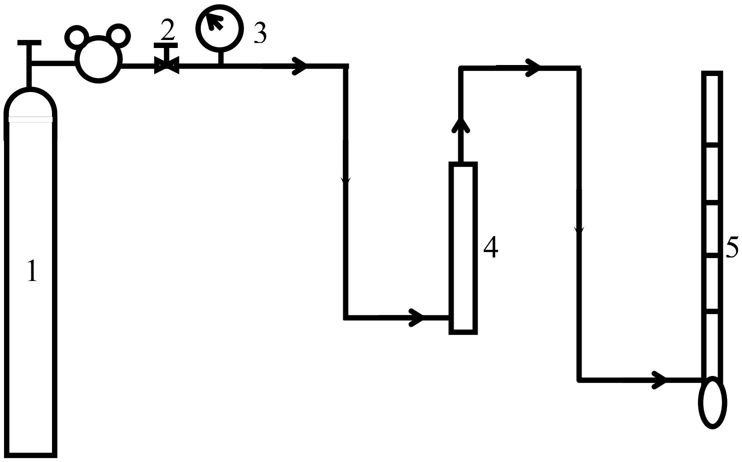

Figure 4.4 Schematic of the gas permeation setup.

1 nitrogen cylinder; 2 pressure regulator; 3 pressure gauge; 4 hollow fiber membrane module; 5 bubble flow meter.

4.3 Results and discussion

4.3.1 Effects of spinning parameters on the membrane porous structure

4.3.1.1 Effects of dope extrusion rate

The spinning speed determines the productivity of hollow fiber membrane manufacturing. A variation in the spinning speed directly affects the rheology of the spinning solution flowing through a spinneret, subsequently the fiber structure and separation performance. An understanding of the effect of fluid rheological behavior within the spinneret on the hollow fiber membrane formation is important for a large-scale hollow fiber production. The effects of dope extrusion rate on membrane formation were investigated here.

The effects of dope extrusion rate on the outer diameter and wall thickness of the hollow fiber walls are shown in Figures 4.5 and 4.6. When the dope extrusion rate increased, both the outer diameter and wall thickness increased. The effects of dope extrusion rate on the mean pore radius and ε/l of the membranes, which are shown in Figures 4.7 and 4.8, were much more complicated. When the dope extrusion rate increases, the extrusion shear rate will increase. This will lead to a decrease in the polymer solution viscosity. A low viscosity of the polymer solution will lead to a loose membrane structure, and thus wall thickness and outer diameter will increases, and the mean pore radius should increase [Aptel et al., 1985; Liu, 2003]. However, Figure 4.7 shows that the mean pore radius tends to be constant when the shear rate is high enough; while Figure 4.8 shows that the mean pore radius continues to decrease with an increase in the dope extrusion rate when LiCl was used as an additive. With an increase in the wall-thickness, the solvent-nonsolvent exchange rate during membrane formation decreases. This causes a decrease in pore size. Therefore, if the effects of shear rate and the mass transfer resistance to solvent-nonsolvent exchange were equivalent, the mean pore radius would not change. If the effect of mass transfer resistance to solvent-nonsolvent exchange overwhelms the effect of shear rate, the mean pore radius of the membranes will decrease. The different trends between Figures 4.7 and 4.8 are caused by the presence of additive LiCl that will increase the thermodynamic stability of polymer solution.

Other explanations have been reported to explain the effects of dope extrusion rate on membrane structure. One explanation is that an increase in the dope extrusion rate will result in an enlargement of the miscibility gap that results in faster phase inversion. The system will be destabilised very quickly, causing a steeper polymer concentration gradient at the membrane surface. The polymer rich phase tends to be more concentrated while the polymer lean phase tends to be leaner, thereby forming a denser structure [Idris et al., 2002]. Later on, Ismail et al. [2006] proposed that: as the dope extrusion rate increases, the polymer chains tend to align themselves better and pack more closely to each other. The chain packing introduced by shear will decrease the pore size. The aligning of polymer chains as well as the loose structure will help increase the porosity of the membranes.

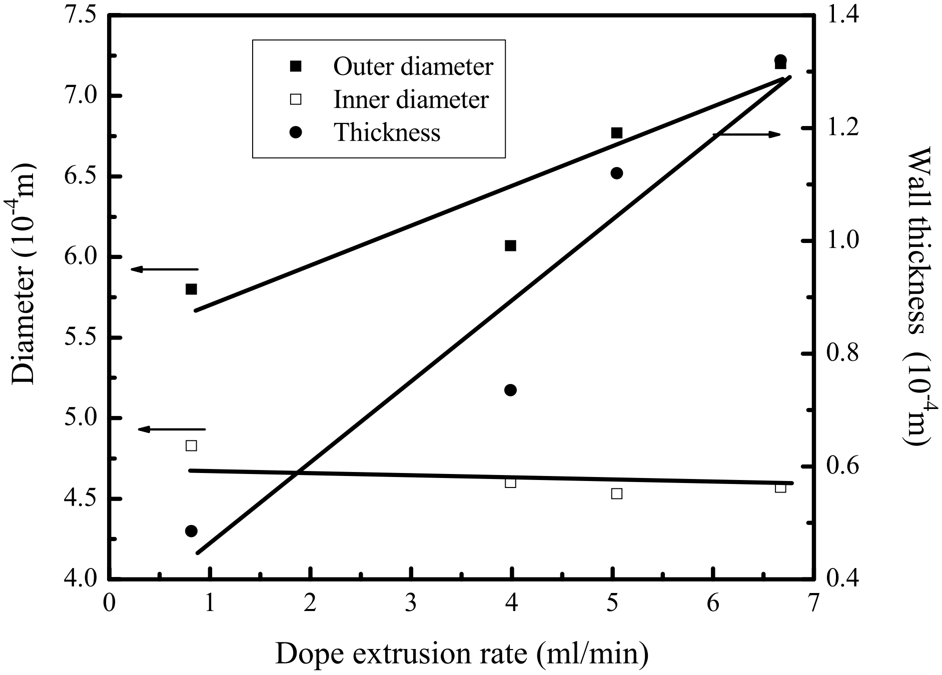

Figure 4.5 Effect of dope extrusion rate on the fiber dimensions. Dope solution, Kynar 2851:NMP=82:18 wt%. Base line spinning conditions: air gap, 7.9 cm; relative humidity, 50 %; room temperature, 23°C; outer coagulant temperature, 16°C; take-up speed, 5.92 m/min; internal coagulant flow velocity: 6.11 m/min.

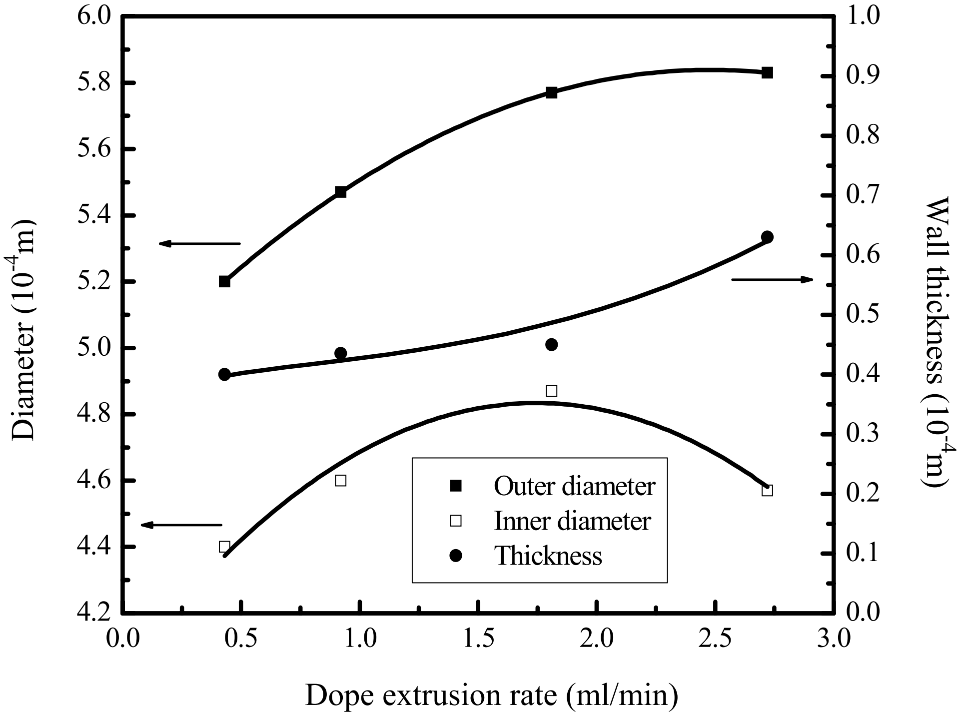

Figure 4.6 Effect of dope extrusion rate on the fiber dimensions. Dope solution, Kynar 2851:NMP:LiCl=78.4:18:3.6 wt%. Base line spinning conditions: air gap, 7.7 cm; relative humidity, 30 %; room temperature, 23°C; outer coagulant temperature, 16°C; take-up speed, 5.92 m/min; internal coagulant flow velocity, 6.11 m/min.

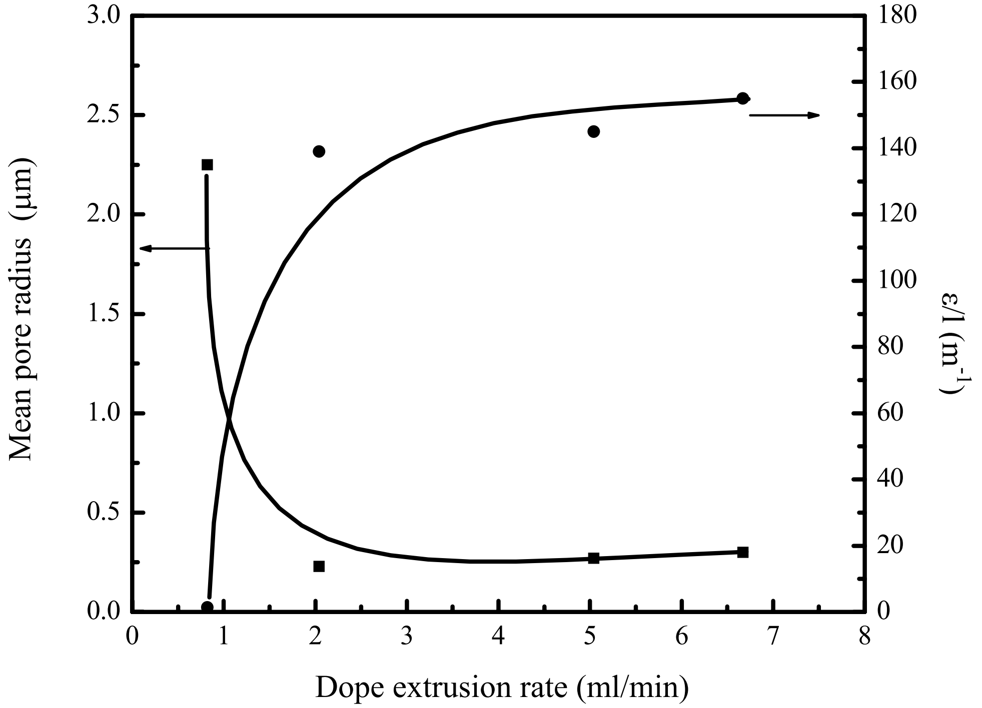

Figure 4.7 Effect of dope extrusion rate on the pore size and ε/l of membranes. Other spinning conditions were the same as those shown in Figure 4.5.

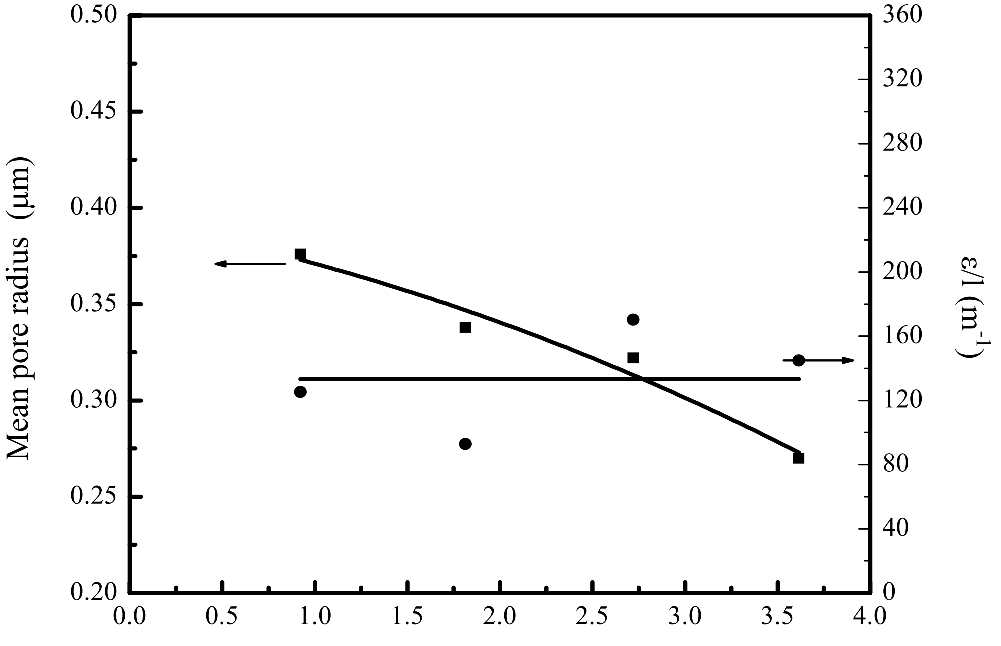

Figure 4.8 Effect of dope extrusion on the pore size and ε/l of membranes. Other spinning conditions were the same as those shown in Figure 4.6.

4.3.1.2 Effects of internal coagulant flow velocity

During the dry/wet phase inversion fabrication process, the use of an internal coagulant not only gives a stress to open the hollow fiber but also offers nonsolvent to exchange with the solvent from the inner wall of the nascent fiber. When the internal coagulant flow velocity increases, the liquid pressure in the axial direction is increased. Therefore, the outer diameters and the inner diameters of the hollow fibers will increase and the wall thickness will decrease. This is shown in Figures 4.9 – 4.12.

The internal coagulant can be used to fine-tune the structure of the hollow fibers, which have an impact on the membrane permeability. The solvent-nonsolvent exchange at the interface between polymer solution and the nonsolvent starts right after the nascent fiber leaves the spinneret and contacts the internal coagulant in the bore side of the fiber. When the internal coagulant flow velocity is increased, more nonsolvent will be supplied, which enhances the solvent-nonsolvent exchange. The enhanced nonsolvent inflow will accelerate the formation of more open porous membrane structure [Yeow et al., 2005]. Therefore, the mean pore size increases, while the effective surface porosity decreases. This is shown in Figures 4.13 – 4.14, where the mean pore size is shown to increase with an increase in the velocity of inner coagulant, whereas the opposite is found true for ε/l.

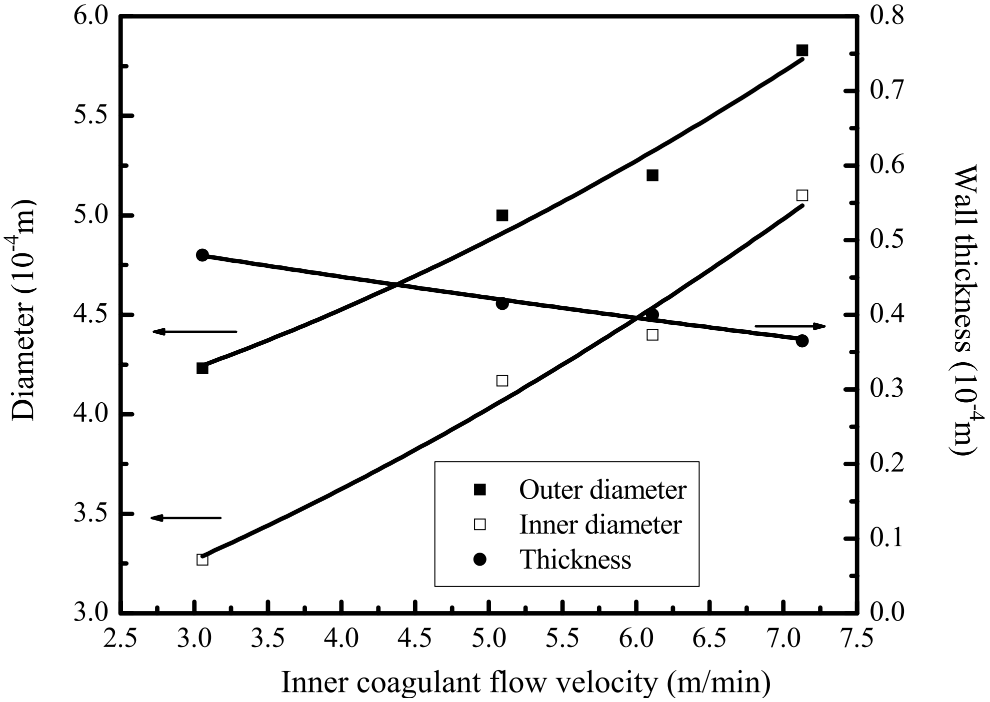

Figure 4.9 Effect of internal coagulant flow velocity on the hollow fiber dimensions. Dope solution, Kynar 2851:NMP:LiCl=78.4:18:3.6 wt%. Base line spinning conditions: air gap, 8.7 cm; relative humidity, 30%; room temperature, 23°C; outer coagulant temperature, 16°C; take-up speed, 5.92 m/min; dope extrusion rate, 0.43 m/min.

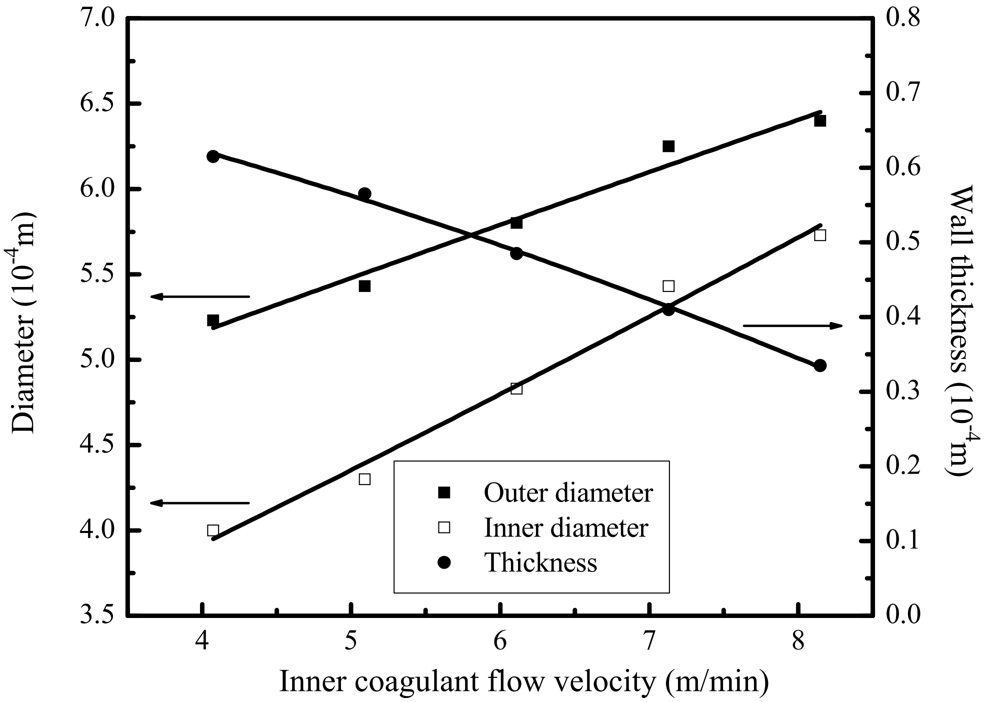

Figure 4.10 Effect of internal coagulant flow velocity on the hollow fiber dimensions. Dope solution, Kynar 2851:NMP=82:18 wt%. Base line spinning conditions: air gap, 7.9 cm; relative humidity, 50 %; room temperature, 23°C; outer coagulant temperature, 16°C; take-up speed, 5.92 m/min; dope extrusion rate, 0.82 ml/min.

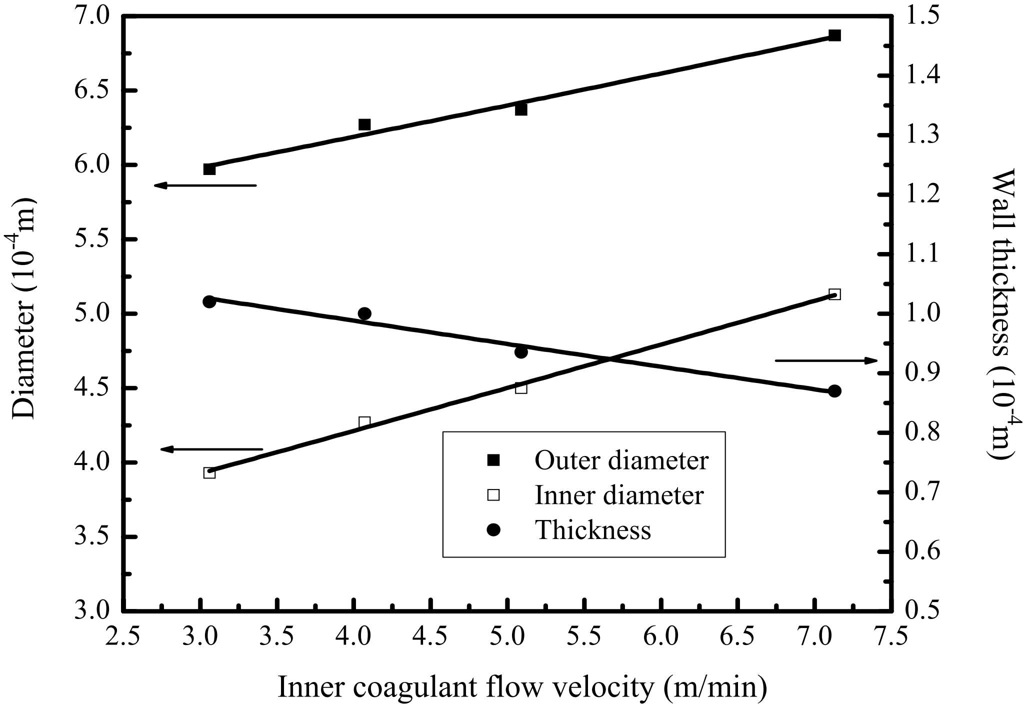

Figure 4.11 Effect of internal coagulant flow velocity on the hollow fiber dimensions. Dope solution, Kynar 741:NMP=82:18 wt%. Baseline spinning conditions: air gap, 7.8 cm; relative humidity, 42 %; room temperature, 23°C; outer coagulant temperature, 16°C; take-up speed, 5.92 m/min; dope extrusion rate, 2.53 ml/min.

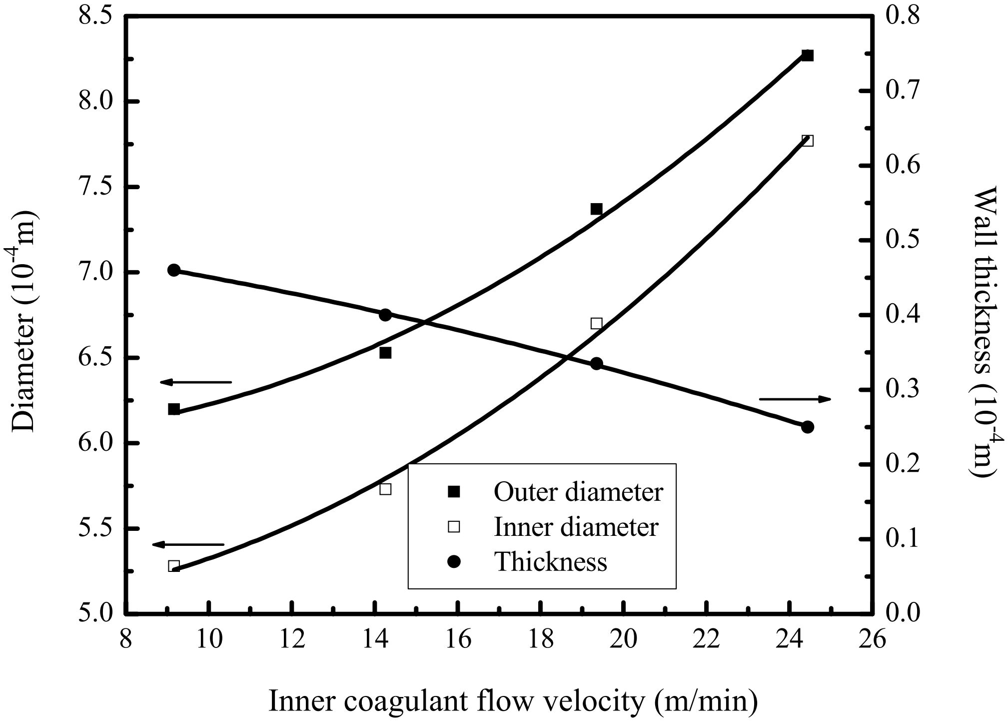

Figure 4.12 Effect of internal coagulant flow velocity on the hollow fiber dimensions. Dope solution, Kynar 741:NMP:LiCl=78.4:18:3.6 wt%. Base line spinning conditions: air gap, 7.8 cm; relative humidity, 21 %; room temperature, 22°C; outer coagulant temperature, 16°C; take-up speed, 5.92 m/min; dope extrusion rate, 0.73 ml/min.

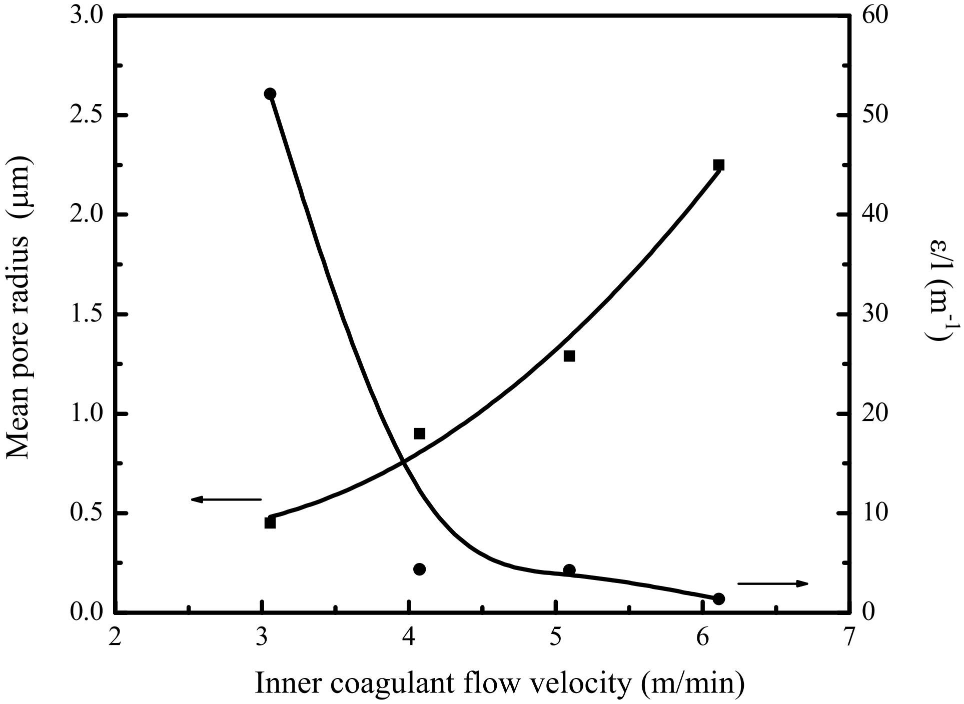

Figure 4.13 Effect of internal coagulant flow velocity on the pore size and ε/l of membranes. Other spinning conditions were the same as those shown in Figure 4.10.

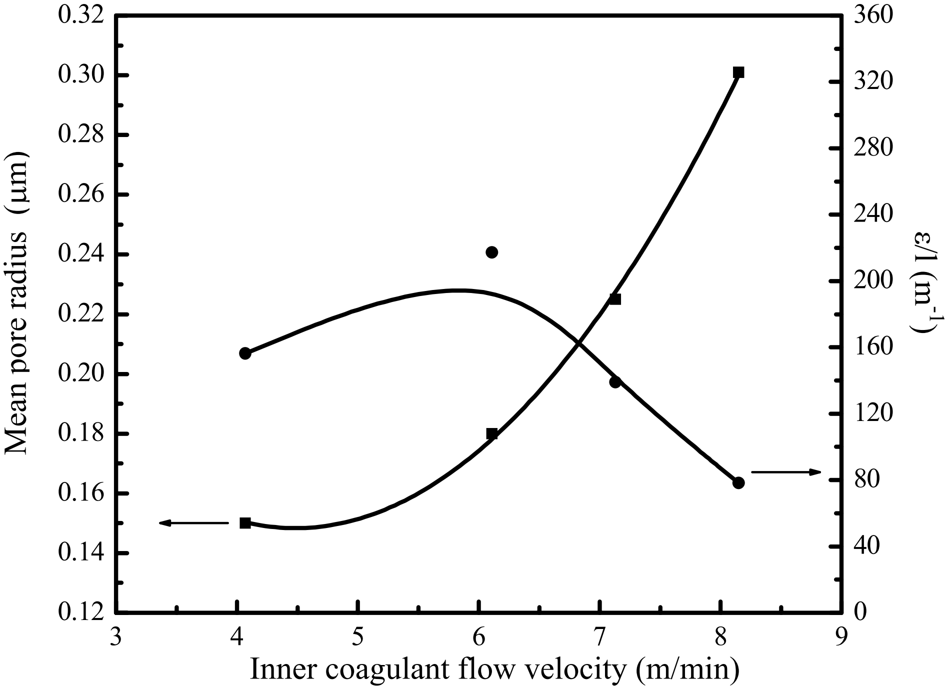

Figure 4.14 Effect of internal coagulant flow velocity on the pore size and ε/l of membranes. Other spinning conditions were the same as those shown in Figure 4.11.

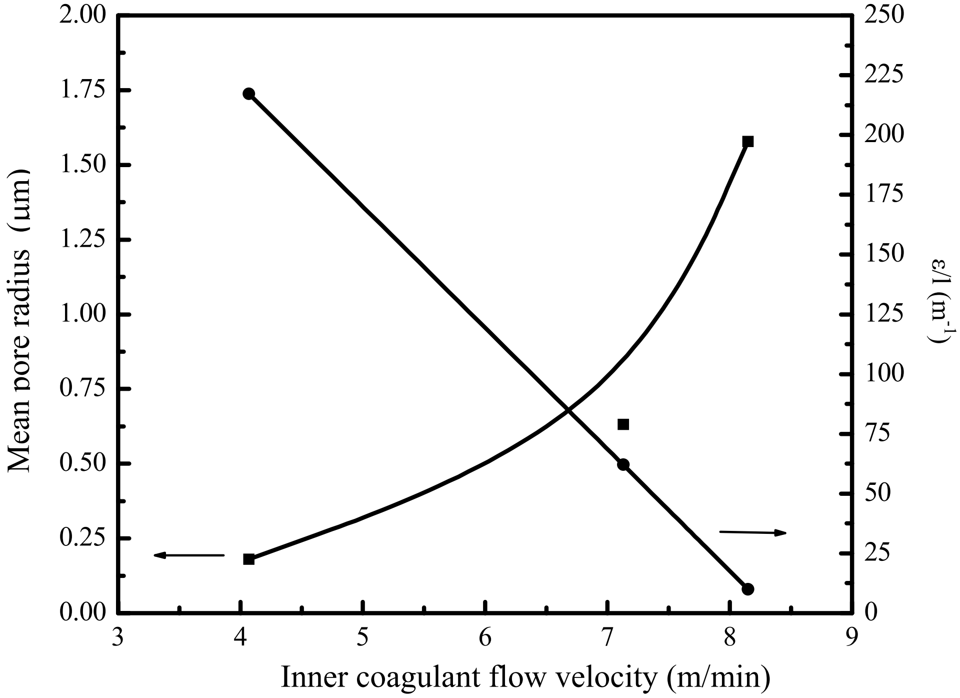

Figure 4.15 Effect of internal coagulant flow velocity on the pore size and ε/l of membranes. Other spinning conditions were the same as those shown in Figure 4.12.

4.3.1.3 Effects of take-up speed

Figures 4.16 – 4.18 show the effect of the take-up speed on the outer diameter, inner diameter and wall thickness of the hollow fibers. It can be seen that the diameter of the hollow fibers decrease with an increase in the take-up speed. This can be attributed to the orientation of the polymer molecules. It was reported that the molecular chains in the hollow fiber would be more oriented when the take-up speed was increased [Chou and Yang, 2005]. The volume between the polymer chains decreases, which results in hollow fibers with smaller diameters. However, it is interesting that the fiber wall thickness was only slightly affected.

A higher take-up speed will tend to stretch the fibers, leading to more porous morphology and structure, as shown in Figures 4.19 and 4.20. When the fiber take-up speed was increased, there was a force exerted along the extrusion direction [Liu, 2003]. The contact surface area per volume of polymer solution was increased and the solvent-nonsolvent exchange rate was enhanced. Consequently, bigger pores were formed in the wall of the fibers. As a result, the mean pore size increased and the porosity (ε) decreased. Obviously, resulting from the decrease in the porosity, the composite parameter (ε/l) will decrease as the take-up speed increases.

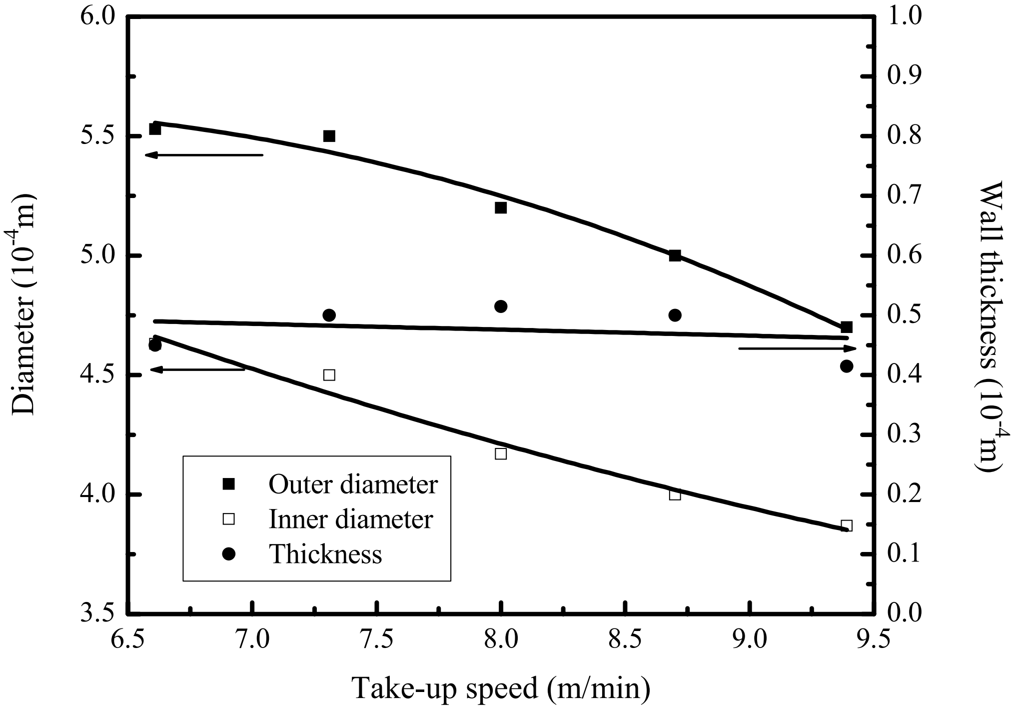

Figure 4.16 Effect of take-up speed on the fiber dimensions. Dope solution: Kynar 2851:NMP=82:18 wt%. Base line spinning conditions: air gap, 7.9 cm; relative humidity, 50 %; room temperature, 23°C; outer coagulant temperature, 16°C; internal coagulant flow velocity, 6.2 m/min; dope extrusion rate, 0.82 ml/min.

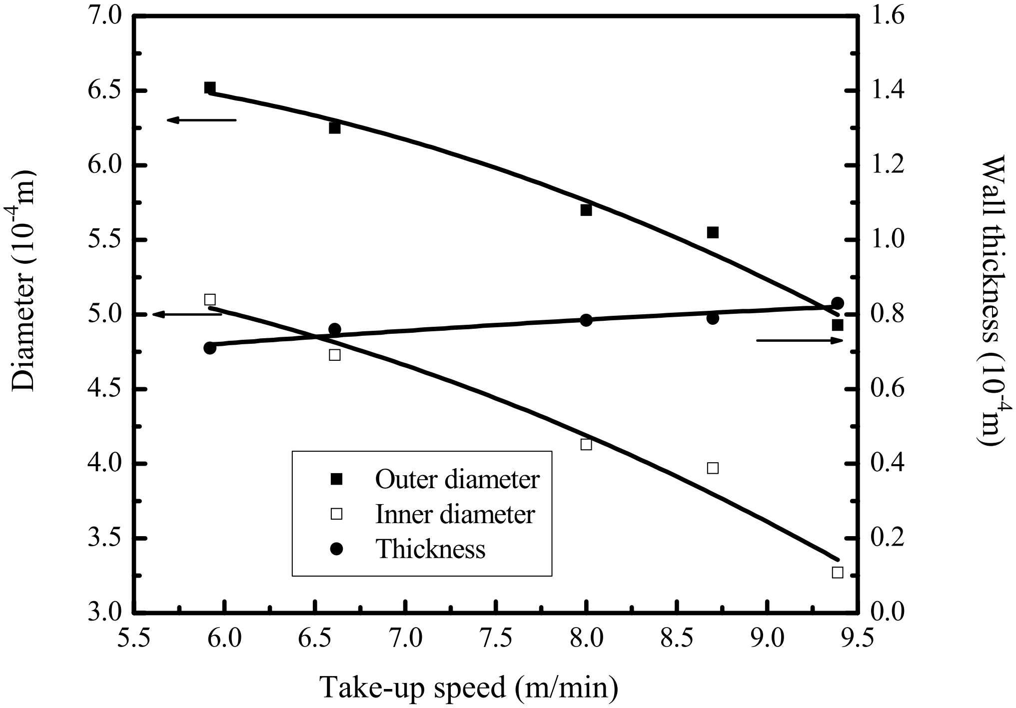

Figure 4.17 Effect of take-up speed on the fiber dimensions. Dope solution, Kynar 741:NMP=82:18 wt%. Base line spinning conditions: air gap, 7.8 cm; relative humidity, 42 %; room temperature, 23^{o}C; outer coagulant temperature, 16^{o}C; internal coagulant flow velocity, 6.11 m/min; dope extrusion rate, 2.53 ml/min.

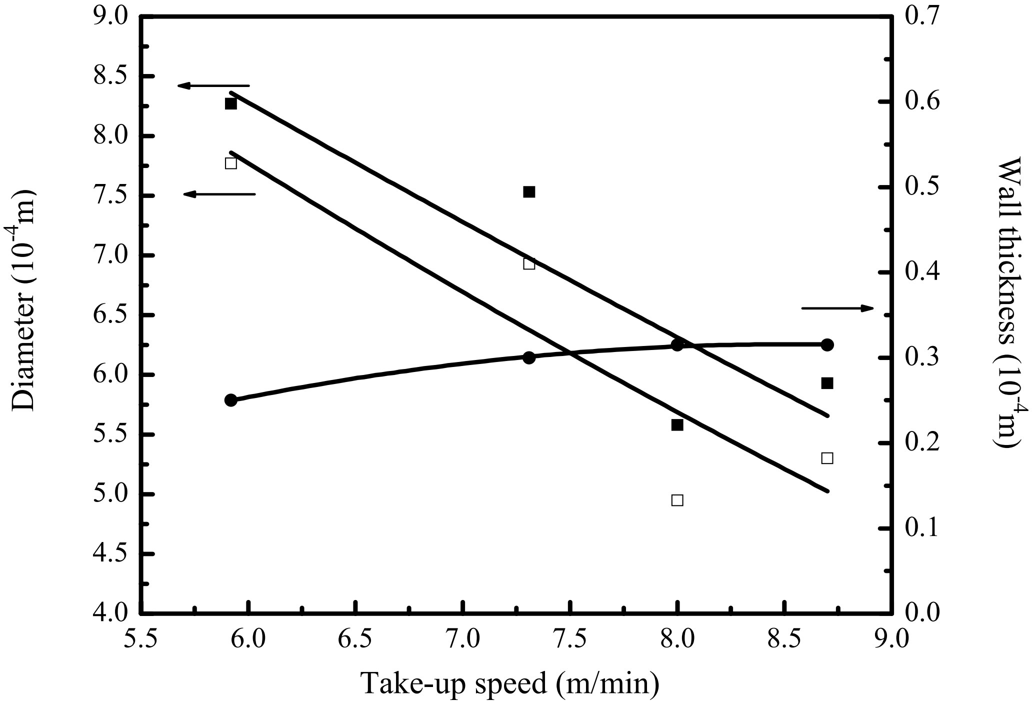

Figure 4.18 Effect of take-up speed on the fiber dimensions. Dope solution, Kynar 741:NMP:LiCl=78.4:18:3.6 wt%. Base line spinning conditions: air gap, 7.8 cm; relative humidity, 21 %; room temperature, 22^{o}C; outer coagulant temperature, 16^{o}C; internal coagulant flow velocity, 24.44 m/min; dope extrusion rate, 0.73 ml/min.

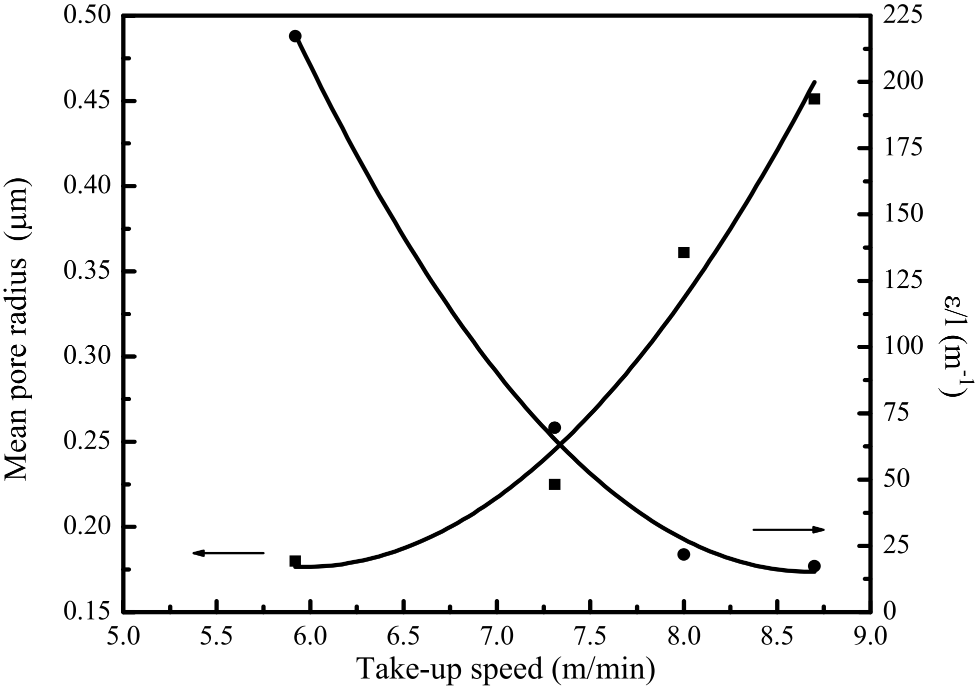

Figure 4.19 Effect of take-up speed on the pore size and ε/l of membranes. Other spinning conditions were the same as those shown in Figure 4.17.

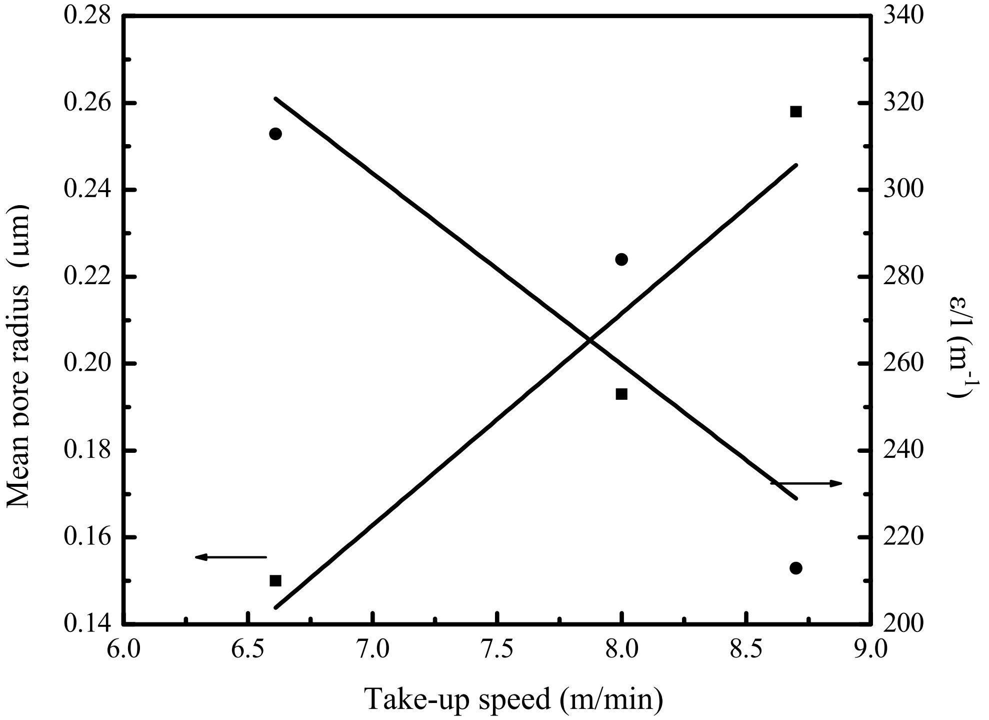

Figure 4.20 Effect of take-up speed on the pore size and ε/l of membranes. Other spinning conditions were the same as those shown in Figure 4.18.

4.3.1.4 Pore size distribution of the hollow fiber membranes

The pore size distribution of porous membranes is very important as it governs the permeability and selectivity [Lee et al., 1997]. The pore size distribution of the hollow fiber membranes was determined by the gas-liquid displacement method. The spinning conditions of fibers are summarized in Table 4.1. The relationship between the nitrogen flux and pressure for the various fibers is given in Appendix A. The corresponding pore size distributions of these fibers are shown in Figures 4.21 – 4.29. In general, these membranes have sharp pore size distributions, indicating that the pore sizes of hollow fiber membranes fabricated from Kynar 741 and 2851 are nearly monodisperse. Even distribution of pore sized is essential to achieve a sharp separation in ultrafiltration and microfiltration.

Table 4.1 Spinning conditions of the hollow fiber membranes 1–9.

Membrane	Dope composition (wt %)	Air gap (cm)	Relative humidity (%)	Take-up speed (m/min)	Internal coagulant flow velocity (m/min)	Dope extrusion rate (ml/min)
1	Kynar 741:NMP =82:18	7.8	42	5.92	4.07	2.53
2	Kynar 741:NMP =82:18	7.8	42	5.92	5.09	2.53
3	Kynar 741:NMP =82:18	7.8	42	5.92	8.15	2.53
4	Kynar 741:NMP =82:18	7.8	42	5.92	3.06	2.53
5	Kynar 741:NMP =82:18	7.8	42	8.70	6.11	2.53
6	Kynar 741:NMP:LiCl =78.4:18:3.6	7.8	21	8.70	14.26	1.19
7	Kynar 2851:NMP =82:18	7.9	50	5.92	6.11	3.99
8	Kynar 2851:NMP =82:18	7.9	50	5.92	6.11	6.67
9	Kynar 2851:NMP:LiCl =78.4:18:3.6	8.7	28-30	5.92	7.13	0.43

(Spinneret orifice size OD/ID, 1.0 / 0.5 mm; room temperature, 23^{o}C, outer coagulant temperature: 16^{o}C)

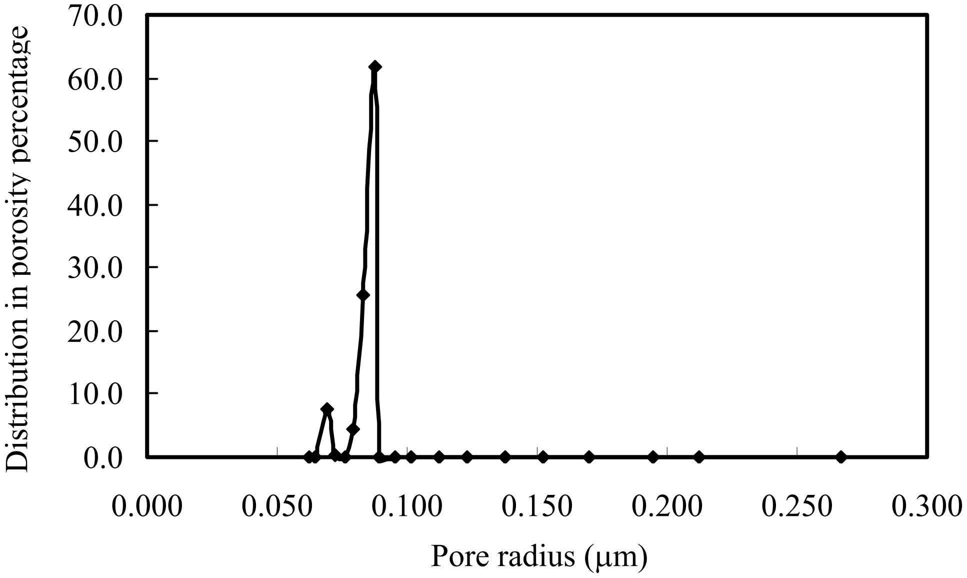

Figure 4.21 Pore size distribution of membrane 1.

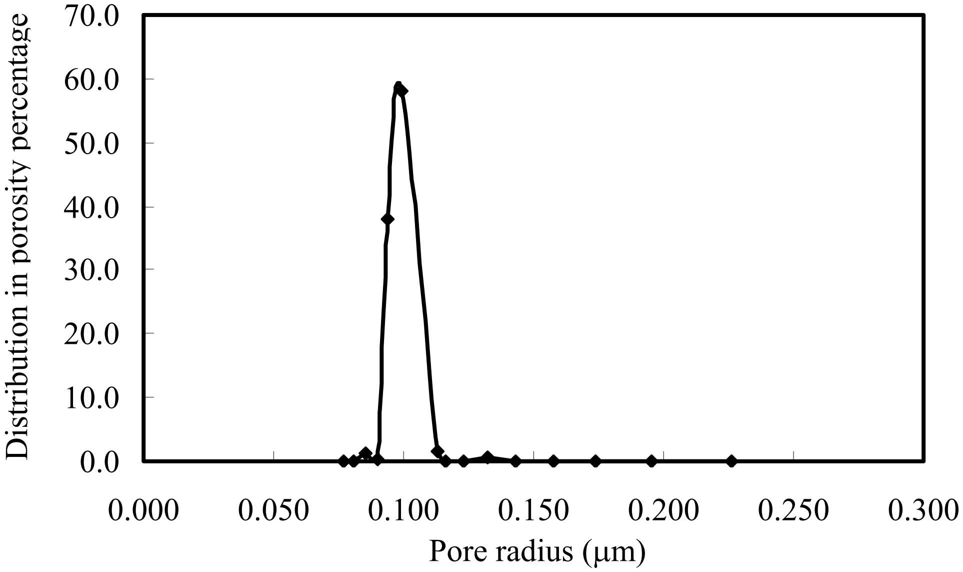

Figure 4.22 Pore size distribution of membrane 2.

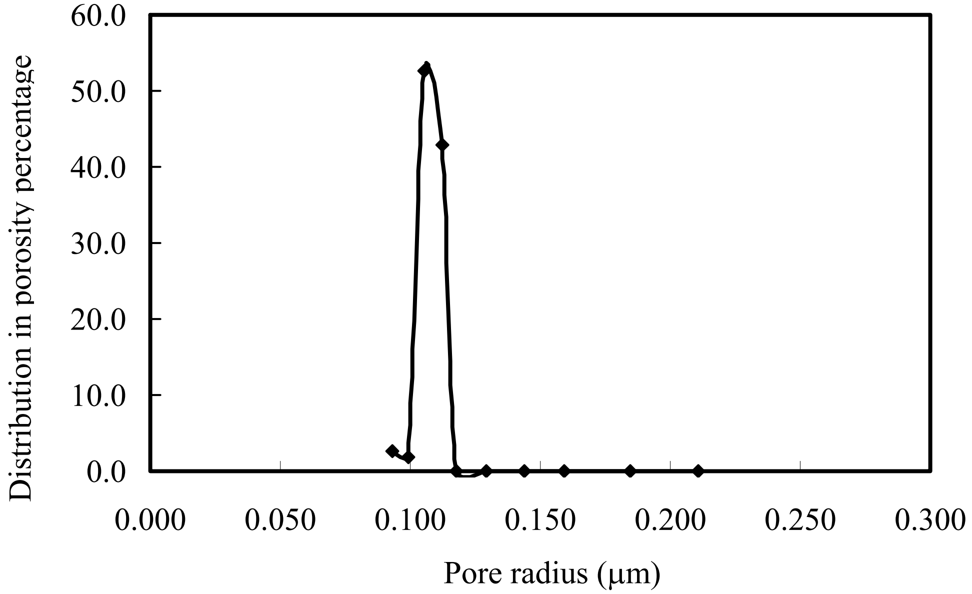

Figure 4.23 Pore size distribution of membrane 3.

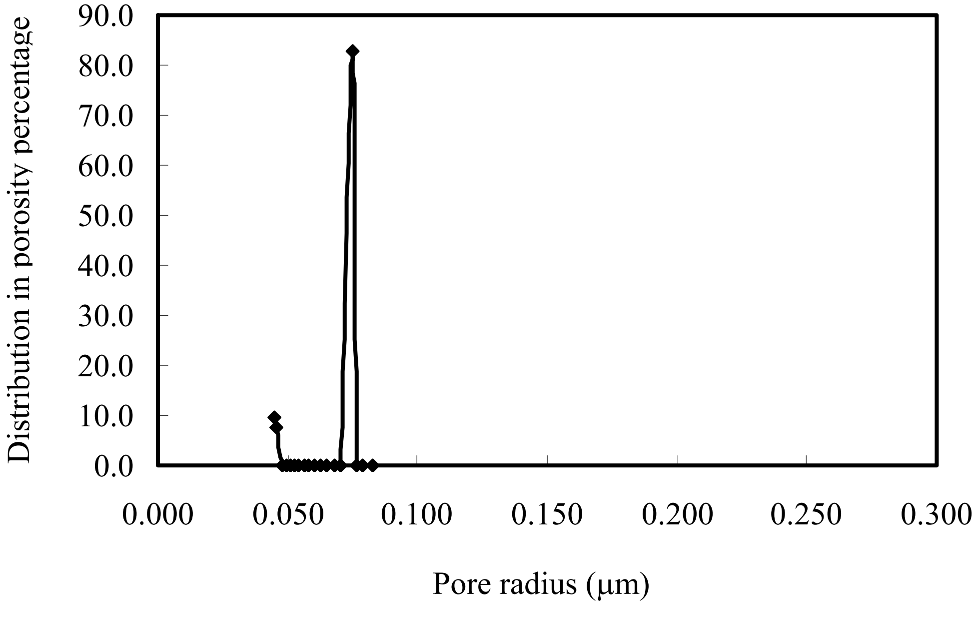

Figure 4.24 Pore size distribution of membrane 4.

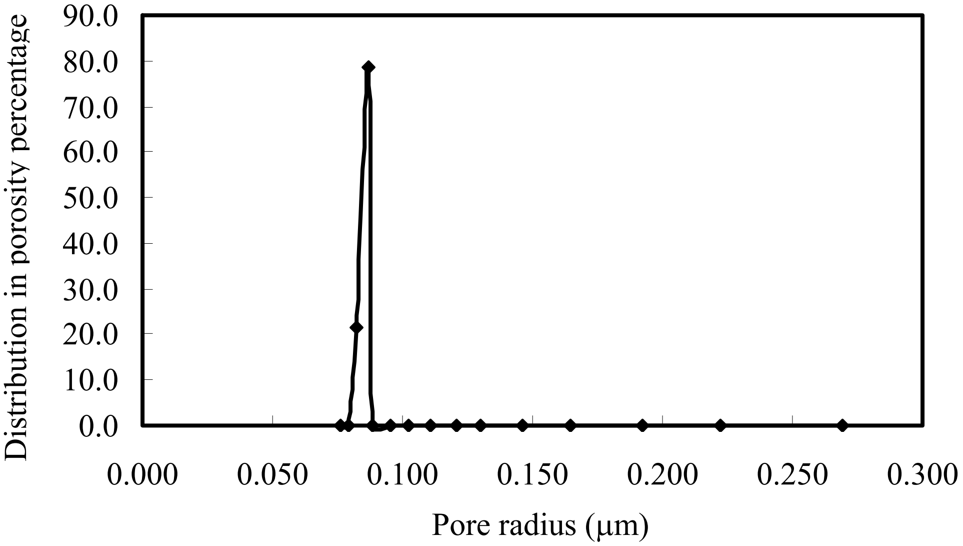

Figure 4.25 Pore size distribution of membrane 5.

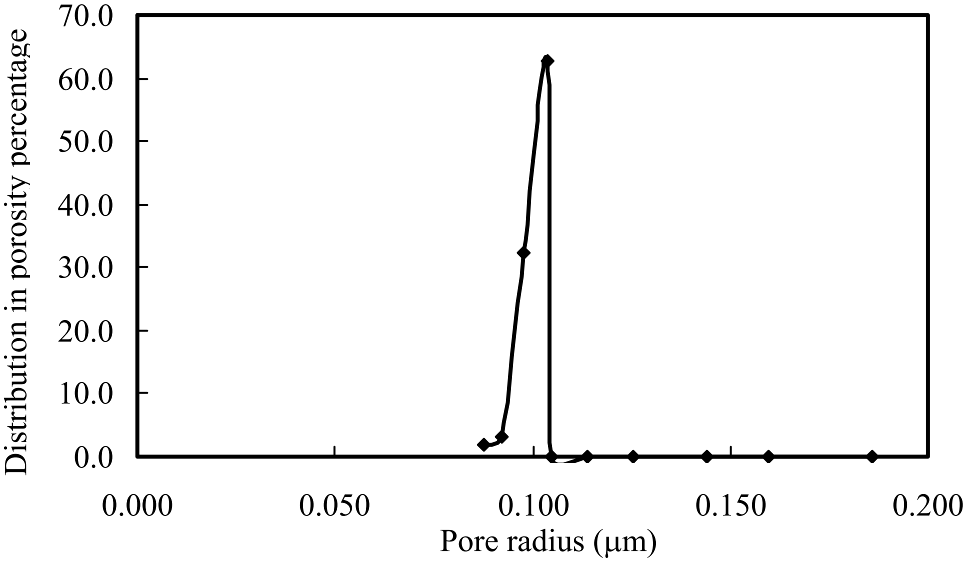

Figure 4.26 Pore size distribution of membrane 6.

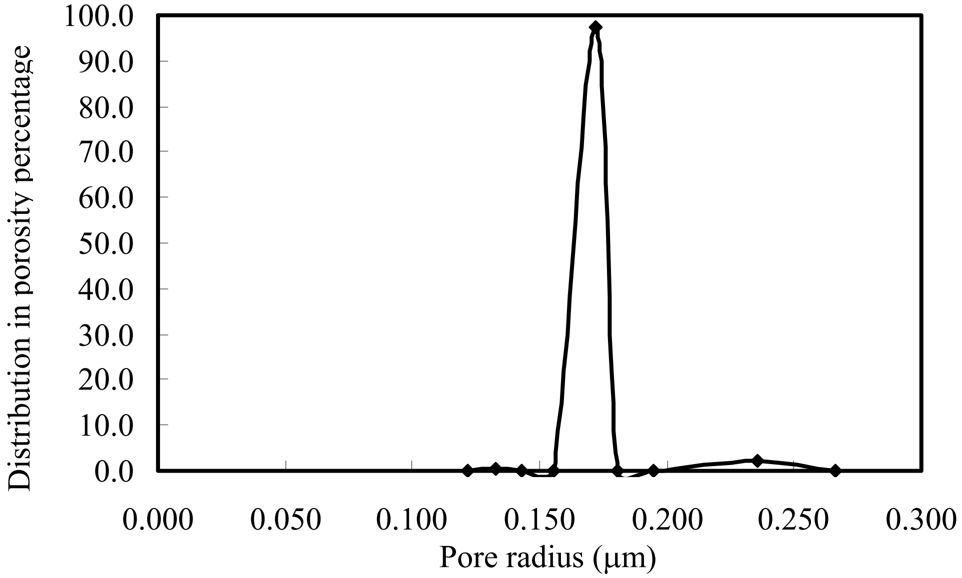

Figure 4.27 Pore size distribution of membrane 7.

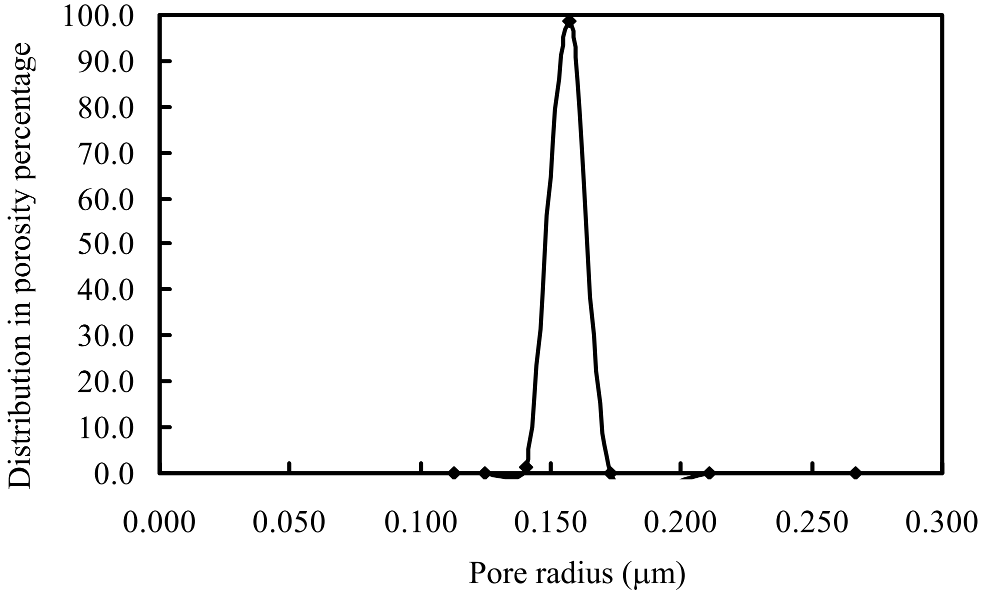

Figure 4.28 Pore size distribution of membrane 8.

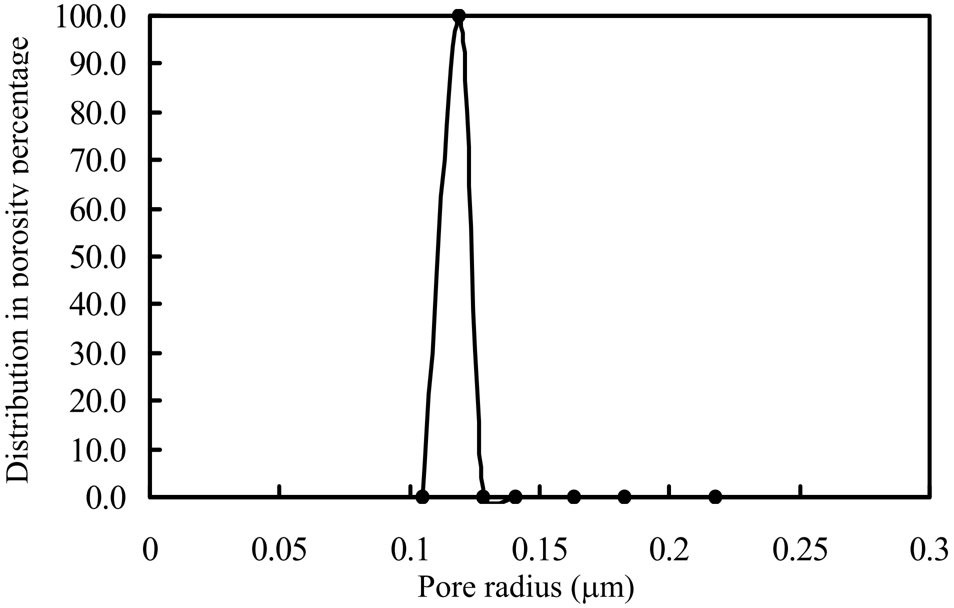

Figure 4.29 Pore size distribution of membrane 9.

4.3.2 Morphologies of the hollow fiber membranes

The microstructure and morphology of the PVDF membranes were examined under scanning electron microscope (SEM). Figure 4.30 shows the morphologies of the membranes (the spinning conditions of these membranes are listed in Table 4.2). From these pictures, it can be found that all the membranes exhibited a macrovoid structure near the surface, and a sponge-like structure in the middle of the fiber wall. The macrovoid structure resulted from fast solvent-nonsolvent exchange, while the sponge-like structure was attributed to the slower solvent-nonsolvent exchange. The macrovoids offer little resistance to fluid permeation but also lower the mechanical strength of the membrane. On the other hand, the sponge structure is mechanically strong, but it can increase the permeation resistance. Therefore, in selecting and formulating membrane fabrication conditions, both of these two aspects should be considered for specific applications [Liu, 2003].

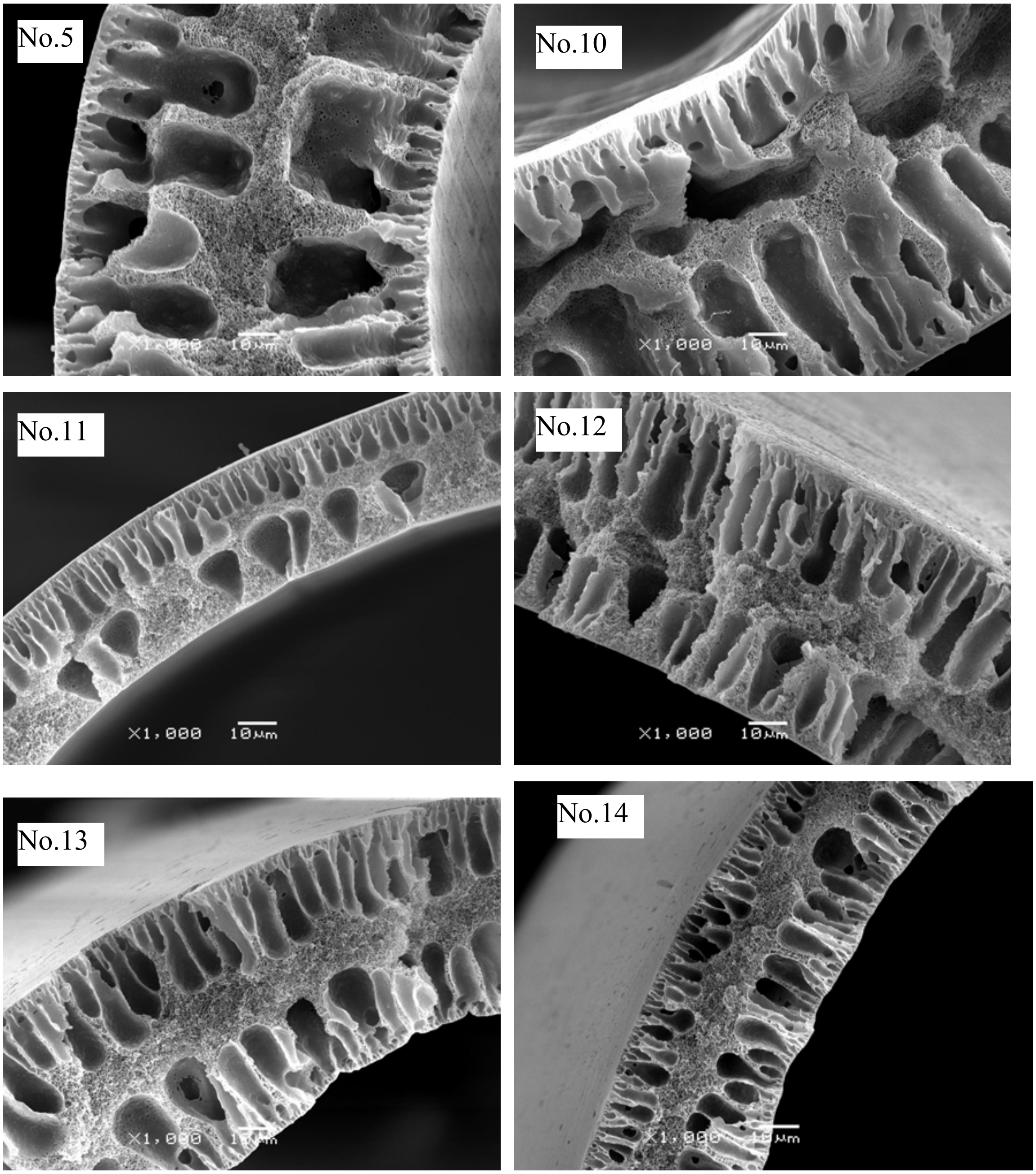

Figure 4.30 Morphologies of the cross-section of hollow fiber PVDF membranes.

Table 4.2 Spinning conditions of hollow fibers 10 – 14.

Serial number	Dope composition (wt %)	Air gap (cm)	Relative humidity (%)	Taken-up speed (m/min)	Internal coagulant flow velocity (m/min)	Dope extrusion (ml/min)
10	Kynar 741:NMP =82:18	7.8	42	5.92	6.11	2.53
11	Kynar 2851:NMP:LiCl =78.4:18:3.6	7.7	28-30	5.92	6.11	0.92
12	Kynar 2851:NMP:LiCl =78.4:18:3.6	7.7	28-30	5.92	6.11	2.72
13	Kynar 2851:NMP =82:18	7.9	50	5.92	3.06	0.82
14	Kynar 2851:NMP =82:18	7.9	50	5.92	6.11	0.82

(Spinneret orifice size OD/ID, 1.0 / 0.5 mm; room temperature, 23^{o}C, outer coagulant temperature: 16^{o}C)

As discussed in the thermodynamic and kinetic studies, for the membranes fabricated from Kynar 741, the use of additive LiCl did not have significant effect on the membrane formation. This means that the morphologies of membranes fabricated with or without LiCl additive will not be significantly different. The influence of LiCl on the morphologies of membrane fabricated from Kynar 2851 was illustrated in Figure 4.30. As shown in the morphology of membrane 14, there are finger-like structures near both the inner and outer surfaces of the hollow fibers when the membranes were fabricated from Kynar 2851 without LiCl. However, when LiCl was used as an additive, as shown in the morphology of membrane 11, there are some water-drop like, bigger than finger-like cavities near the inner wall of the hollow fibers. The morphology difference between those two types of membranes demonstrates the conclusion drawn in the thermodynamic section that the addition of LiCl in Kynar 2851/NMP solution could improve the water tolerance of the solution, which would lead to bigger pores in the membrane.

Membranes 11 and 12 were fabricated under a dope extrusion rate of 0.92 and 2.72 ml/min, respectively. It appears that the size of cavities in the inner wall decreases and the cavities were packed closer when the dope extrusion rate increases. This can be explained based on the rheological behavior of the dope solutions. When the dope solution extrusion rate is increased, the polymer chains tend to align themselves better, causing the polymer molecules to pack closer with a more orderly arrangement [Ismail et al., 2006]. The morphologies also illustrate that the porosity of membrane 12 was higher than the porosity of membrane 11. This is consistent with the gas permeation data shown in section 4.3.1.1.

Figure 4.30 shows that the porous structures of the outer walls of the membranes 11 and 12 are similar, in spite of the dope extrusion rates were different during the membrane fabrication. This should be attributed to the existence of air gap, which provided a period for solvent evaporation and favored the formation of the polymer rich phase at the outer surface of the nascent fiber. During the phase inversion in the coagulation bath, the polymer rich phase develops into a denser skin layer and limited the influence of molecular chain orientation on the porous structure of the outer wall.

The effect of internal coagulant flow velocity on the membrane morphology was illustrated by the SEM pictures as well. Membranes 13 and 14 were fabricated at an internal coagulant flow velocity of 3.06 and 6.11 m/min, respectively. As shown in Figure 4.30, membrane 14 has bigger cavities near the inner surface of the hollow fibers because an increase in the internal coagulant flow velocity will elevate the solvent-nonsolvent exchange rate.

As discussed before, the mean pore radius increases with an increase in the take-up speed. However, as shown in the morphologies of membranes 5 and 10, the macrovoid structure of membrane 10 would collapse if the take-up speed was too high.

4.4 Conclusions

The specialty PVDF materials newly developed by Arkema were used to fabricate hollow fiber membranes. The effects of parameters involved in the procedure for hollow fiber spinning on the dimensions and properties of the fibers were investigated. The porous structure of the membranes was characterized by the gas permeation method, gas-liquid displacement method and scanning electron microscope.

It was found that Kynar 741 and 2851 were most suitable for fabricating hollow fiber membranes. The membranes exhibited a macrovoid structure near the surface and a sponge-like structure in the middle of the fiber wall. The dimensions and properties of the membranes were affected by the dope extrusion rate, internal coagulant flow velocity and take-up speed effectively. With an increase in the dope extrusion rate, both the outer diameter and wall thickness increased. When the internal coagulant flow velocity increased, both the outer and inner diameters of the hollow fibers increased, but the fiber wall thickness decreased. In addition, increasing the internal coagulant flow velocity would increase the mean pore size and decrease the effective surface porosity. When the take-up speed increased, the diameters of the hollow fibers decreased, and membranes were more porous.

Chapter 5

Improving the hydrophilicity of PVDF membranes by amine treatment

---

5.1 Introduction

Poly(vinylidene fluoride) (PVDF) has attracted a lot of interests as a specialty polymer due to its excellent mechanical and chemical properties [Seiler and Scheirs, 1998; Malcolm, 1999]. PVDF membranes have been widely used in microfiltration and ultrafiltration. However, to some extent, their applications have been limited because of the hydrophobicity of the membrane.

One of the problems encountered is protein fouling, which occurs on the membrane surface and within the pores when they are exposed to protein-containing solutions [Mueller and Davis, 1996]. Another disadvantage caused by its hydrophobicity is potential leaking through the tubesheet in hollow fiber modules after use over a long period of time. In the manufacturing process, epoxies have been used as the adhesives to assemble membrane module. It is the adsorption and mechanical interlocking that account for the adhesion [Ellis B., 2006]. For the mechanical interlocking, the adhesion between an adhesive and substrate depends on the mechanical keying of the adhesive into substrate surface irregularities. The adsorption means that the adhesion achieved by the interaction between the pendent hydroxyl groups within the molecule of most epoxies and the hydroxyl groups on the membrane surface via hydrogen bond. The hydrophobic nature of PVDF membranes obstructs the formation of hydrogen bond, which affects the bonding of PVDF fibers by the epoxy potting.

Hence, PVDF membranes modified by chemical and physical methods to improve their surface hydrophilicity have recently been studied [Pasquier et al., 2000; Tarvainen et al., 2000; Kushida et al., 2001].

The C-F bond has very low surface energy, giving PVDF membrane high hydrophobicity [Deanin, 1972]. Alkaline treatment can eliminate F^- and improve the hydrophilicity of PVDF membrane. It was reported that the hydrophilicity could be improved by “flashing” the PVDF in concentrated caustic solutions (e.g., pH14), producing a hydrophilic surface layer [Ross, 2000]. It is commonly considered that the surface modification by alkaline degradation is based on the following reaction [Kise and Ogata 1983; Dias and McCarthy, 1985; Hahn and Percec, 1987; Crowe and Badyal, 1991; Cho and Song, 1995; Brewis et al., 1996; Owen, 1996]:

$$-(CH_2-CF_2)- + XOH \rightarrow -(CH=CF)- + XF + H_2O$$

where X = Li or Na. The primary process is the elimination of HF units and the formation of the C=C bonds along the polymer backbone. This mechanism is generally accepted; however, is proposed on the basis of rather limited experimental data. The polymer structure after alkaline treatment proposed by Ross et al. [2000] is illustrated as follows:

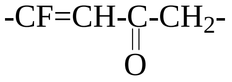

$$-CF=CH-\underset{\underset{O}{\|}}{C}-CH_2-$$

After the elimination reaction, if alkanolamines are added in an alkaline solution, the amine compound can be grafted onto the PVDF material, as suggested by Sterngaard [1998].

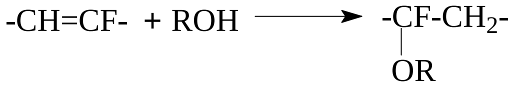

$$-CH=CF- + ROH \longrightarrow -\underset{\underset{OR}{|}}{C}F-CH_2-$$

It was also reported that fluoroelasters could be crosslinked with amines. The amine could displace a halogen substitute or act as a dehydrohalogenating agent. The following mechanism was postulated for the elimination of halogen in the crosslinking reactions [Pacioreck et al., 1960; Paciorek et al., 1962]:

$$-CF_2-CH_2-CFCl-CF_2- \xrightarrow{C_4H_9NH_2} -CF-CH=CF-CF_2-$$

This step can be followed by addition, which could take place according to two schemes:

Addition

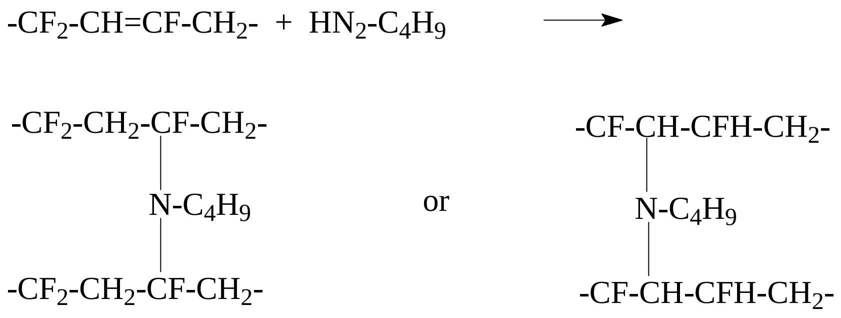

$$-CF_2-CH=CF-CH_2- \ + \ HN_2-C_4H_9 \longrightarrow$$

$$\begin{array}{c} -CF_2-CH_2-CF-CH_2- \\ | \\ N-C_4H_9 \\ | \\ -CF_2-CH_2-CF-CH_2- \end{array} \quad \text{or} \quad \begin{array}{c} -CF-CH-CFH-CH_2- \\ | \\ N-C_4H_9 \\ | \\ -CF-CH-CFH-CH_2- \end{array}$$

In this experiment, aqueous amine solutions were used to modify the PVDF membranes, with an objective of improving the hydrophilicity of the PVDF membranes. Contact angle studies and filtration tests were conducted to evaluate the effectiveness of the modification.

5.2 Experimental

5.2.1 Chemicals and materials

Poly(vinylidene fluoride) (Kynar 741) was provided by Arkema. It was used after thorough drying at 70 ^{o}C for 48 hr. N-methyl-2-pyrrolidone (NMP), purchased from Sigma Aldrich Chemicals, was used as the solvent. Monoethanolamine (MEA) was purchased from Fluka and Diethanolamine (DEA) was purchased from EM Science. 2-Amino-2-Methyl-1-propanol (AMP) was purchased from Aldrich Chemicals. Isopropanol was purchased from Caledon Laboratories. Dextran (MW 266,000) was obtained from Sigma Chemical.

The chemical structures of the amines are:

Monoethanolamine

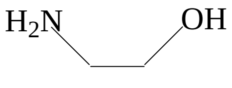

Diethanolamine

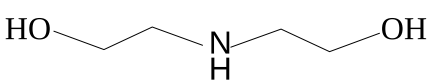

2-Amino-2-Methyl-1-Propanol

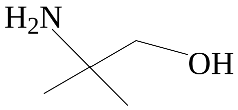

5.2.2 Preparation of PVDF membranes

Non-porous membranes: The PVDF solution with a predetermined composition (NMP:PVDF =18:82) was cast on a glass plate. And then the cast film and the glass plate were immediately put into an oven. Solvent (NMP) evaporated for 48 h under a constant temperature (80^oC) and constant humidity (25%). The air circulation conditions in the oven were maintained constant during the experiment.

Porous membranes: The PVDF solution with a predetermined composition was cast onto a glass plate. And then the cast film and the glass plate were immediately put into an oven that provides a constant temperature and constant humidity for 12 min. Then the membrane and the glass plate were put into a deionized water bath for 90 min, during which period the polymer precipitation occurred due to solvent-nonsolvent exchange. After the NMP solvent residue was removed completely, the membranes were kept in deionized water.

5.2.3 Amine treatment of PVDF membranes

The PVDF membrane was pre-treated with isopropanol to pre-swell the membrane to facilitate subsequent treatment by alcohol amine, and then washed with deionized water. The non-porous membrane was dried in an oven at 50^oC before being used.

The pretreated nonporous PVDF membranes were soaked into amine solutions for a given period of time. Then the membranes were washed with deionized water thoroughly, followed by drying at a constant temperature (50^oC). Similar procedure was used to treat the porous membranes.

5.2.4 Characterization of modified membranes

Fourier-transform Infrared (FT-IR) spectra of the PVDF membranes were obtained using a Bio-Rad FTS 3000 FT-IR spectrophotometer. Each spectrum was collected by cumulating 16 scans at a resolution of 2 wavenumbers.

The element percentage (C/F/O) of the membrane surface was tested by Energy Dispersive X-ray Analysis (EDAX) using a LEO 1530 electron microscope.

Water contact angles of the non-porous PVDF membranes were measured at 25 °C, using Half-Angle Measuring method (Contact Angle Meter: Cam-Plus Micro, Tantec Inc. Micro syringe: 1.5ml, Mitutoyo). For each angle reported, at least five sample readings from different surface locations were averaged.

To investigate the morphology of the membranes, the membranes were examined with a Scanning Electron Microscope (Jeol JSM 6460). To prepare the membrane samples for examination under SEM, the membranes were immersed in liquid nitrogen and fractured. After sputter coating with gold, the membrane samples were examined.

5.2.5 Filtration experiments

The filtration experiments had been discussed in Chapter 3. Usually, the flux recovery ratio was used to evaluate the antifouling property of membranes [Su et al., 2008]. In this research, the antifouling resistance was characterized by the ratio of permeation flux (J_{ps}) obtained with the aqueous Dextran solution (266,000; 1000 ppm) over the pure water permeation flux.

$$R_{af} = \frac{J_{ps}}{J_{pwp}} \tag{5.1}$$

5.3 Results and discussion

5.3.1 FT-IR and EDAX analysis of the PVDF membranes

The chemical structures of non-porous PVDF membranes were studied by FT-IR spectroscopy. The spectra with the functional group region 1400 – 4000 cm^{-1}, are shown in

Figure 5.1. The bonds appearing at 3025 and 2985 cm^{-1} resulted from the asymmetrical C-H stretching mode and symmetrical C-H stretching mode [Silverstein, 2005]. Compared to the spectra of the original membranes, new bands appeared at 1560 and 1645 cm^{-1} in the spectra of treated non-porous membrane. The appearance of those two strong stretching bonds indicates the formation of conjugated C=C and C=O double bonds along the polymer backbone of PVDF in the final product, which agrees with the mechanism proposed by Ross et al. [2000]. The following structure is suggested by Ross et al. [2000]:

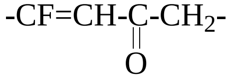

$$\text{-CF=CH-}\underset{\substack{\|\\ \text{O}}}{\text{C}}\text{-CH}_2\text{-}$$

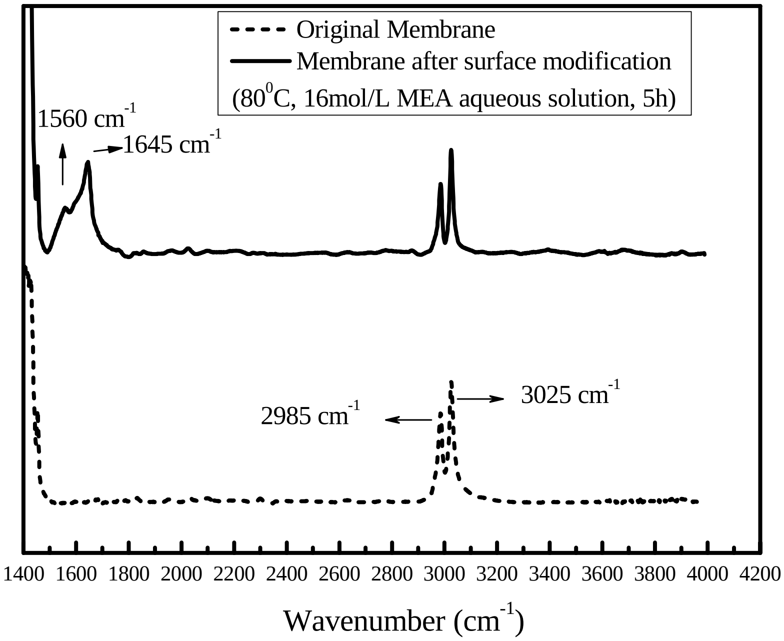

Figure 5.1 FT-IR spectra of non-porous PVDF in the 1400 - 4200 cm^{-1} region.

In order to evaluate how well the chemical modification took place, the elements analysis of membranes was conducted by the EDAX method. The experimental results are given in Table 5.1 (original EDAX spectra are given in Appendix B). The weight percentages of C/O/F at unmodified membrane surface were 61.7, 0.00 and 38.3 wt%, respectively. For the membrane modified with 16 mol/L MEA solution at 80^{o}C for 5 h, the contents of C/O/F are 75.4, 4.58 and 20.0 wt%, respectively. During the modification process, there was no loss of C atoms. Therefore, on the basis of the percentage of C atoms, whose number should be constant during the chemical treatment, the ratio of C/O/F in the membranes can be deduced from Table 5.1 and is listed in Table 5.2. These results demonstrated that some fluorine was eliminated during chemical treatment. And the elimination of fluorine indicated that the chemical treatment had the potential to increase the hydrophilicity of PVDF membranes.

Furthermore, the data in Table 5.2 reveal that the ratio between the F atoms eliminated and O atoms added in the modified membrane was around 5:1, which should have been 3:1 if only conjugated C=C and C=O double bonds appeared in the modified molecular structure. This difference might be attributed to the presence of other molecular structures of modified PVDF membrane, such as the “grafted structure” and “cross-linked structure” [Sterngaard, 1998; Pacioreck and Mitchell, 1960]. However, due to the limitations of FT-IR and EDAX methods to test the –OH, C-N, N-H groups and oxygen, nitrogen elements, the detailed structures of the modified PVDF can not be accurately determined by FT-IR and EDAX analysis.

Table 5.1 Element analysis by EDAX.

Element		Carbon	Oxygen	Fluorine
Original membrane	Weight percentage (wt%)	61.7	0.00	38.3
	Atomic percentage (At%)	71.8	0.00	28.2
Modified membrane$^{(a)}$	Weight percentage (wt%)	75.4	4.58	20.0
	Atomic percentage (At%)	82.4	3.76	13.8

Table 5.2 Element analysis based on Carbon.

Element	Carbon (Number of atoms)	Oxygen (Number of atoms)	Fluorine (Number of atoms)
Original membrane	100	0.00	39.3
Modified membrane$^{(a)}$	100	4.56	16.8
Change of atoms’ amount	0	4.56	-22.5

(a) 5 hours treatment by 16 mol/L MEA solution at 80^{o}C.

5.3.2 Contact angle studies: modification of non-porous PVDF membrane

5.3.2.1 One-variable-at-a-time experiments

As discussed before, the defluorination reaction is the primary reaction for the alkaline treatment and the amine “grafting”. For the defluorination, Brewis et al. [1996] and Ross et al. [2000] postulated a mechanism, which is shown below:

Step 1

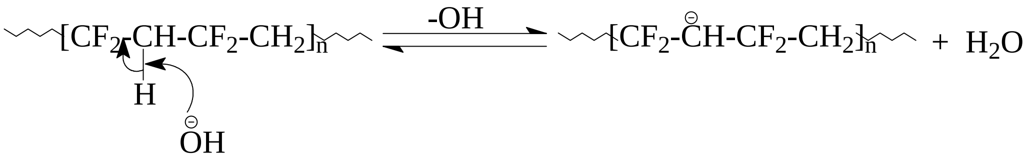

$$\sim[CF_2\text{-}\underset{H}{CH}\text{-}CF_2\text{-}CH_2]_n\sim \xrightleftharpoons{-OH} \sim[CF_2\text{-}\overset{\ominus}{C}H\text{-}CF_2\text{-}CH_2]_n\sim + H_2O$$

Step 2

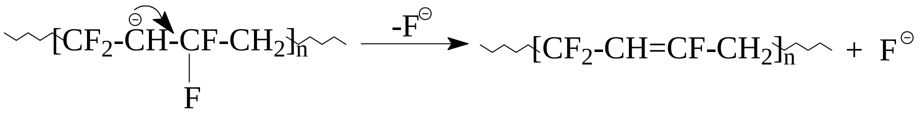

$$\sim[CF_2\text{-}\overset{\ominus}{C}H\text{-}\underset{F}{CF}\text{-}CH_2]_n\sim \xrightarrow{-F^{\ominus}} \sim[CF_2\text{-}CH{=}CF\text{-}CH_2]_n\sim + F^{\ominus}$$

Step 1 is deprotonisation of $-CH_2-$ groups in the chain; step 2 is an elimination reaction. Steps 1 and 2 may occur simultaneously in chain reaction:

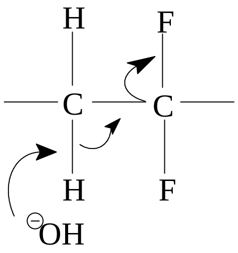

Based on this mechanism, it can be concluded that the alkalinity of the aqueous solutions and temperature will be important to the modification of PVDF membranes [Ross et al., 2000]. The hydroxyl ions, which initiated the reactions, were the product of the amines dissociation in water [Mahajani and Joshi, 1998],

$$AmH + H_2O \rightleftharpoons AmH_2^{+} + OH^{-}$$

In order to find out how the amine treatment can affect the hydrophilicity of PVDF membranes, different types of amines as well as different amine concentrations in MEA solutions were applied to modify the homogeneous PVDF membrane at different temperatures for certain time. The effects of modification on the relative hydrophilicity of the PVDF membranes were characterized by measuring the contact angle of the modified PVDF membranes. Contact angle has been widely used to characterize the polarity of polymers, but it is difficult to be applied on microporous PVDF membranes due to capillary forces within pores, dehydration of wet membrane, contraction in the dried state and restructuring of the surface [Liu et al., 2006]. Therefore, non-porous homogeneous PVDF membranes were used for investigation here.

Figure 5.2 illustrates that the contact angle of membranes modified by MEA solution (98 wt%, 16 mol/L) decreased more significantly than the contact angle of PVDF membranes modified by DEA solution (99.5 wt%) and AMP solution (95 wt%). This indicates that, under these conditions, MEA could improve the hydrophilicity of membrane surface more remarkably than DEA and AMP did. As described in the suggested reaction mechanism by Ross et al. [2000], the hydroxyl ions are important to the defluorination reaction. Especially, defluorination was the primary reaction. The concentration of hydroxyl ion in MEA solution (98%) was higher than in the other two types of amine solutions. So the MEA solution had better performance when it was used to improve the hydrophilicity of PVDF membrane. It also can be found that the hydrophilicity of membranes increased when the modification temperature increased, which implied that the increase of temperature could increase the rates to eliminate F^-, and the membranes modified at high temperature were more hydrophilic. Because of the effectiveness of MEA solution on membrane modification compared to the others, MEA was selected for further research. The effects of MEA concentration in the aqueous solution, treatment time and treatment temperature were investigated.

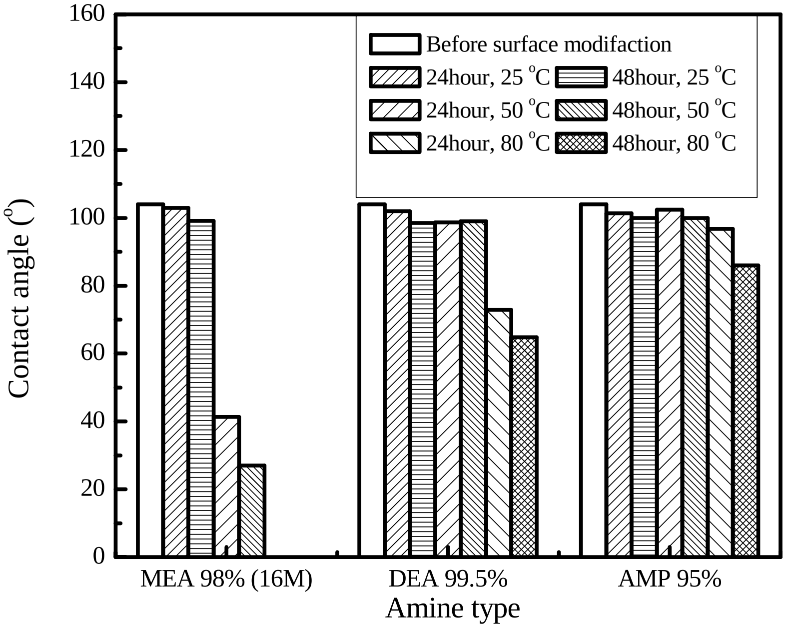

Figure 5.2 Contact angles of PVDF membranes before and after amine treatment at different temperatures.

The investigation of the effect of MEA solution concentration on membrane surface modification was conducted at different modification temperatures and treatment time. All experimental results are illustrated in Figures 5.3 and 5.4. At relatively high temperatures, the contact angle of PVDF membranes decreased drastically with an increase in the MEA concentration, which indicated that the hydrophilicity of the PVDF membranes was improved. The concentration of MEA solutions was shown to be more important at lower temperatures. As shown in Figure 5.4, membranes modified by MEA at high concentrations (14 mol/L, 16 mol/L) became hydrophilic.

Figure 5.4 also illustrates that the treatment time had no impact on the membrane modification at room temperature when the MEA concentration was less than 12 mol/L; it still took a long time to get better hydrophilicity, even at higher concentration (14 mol/L, 16 mol/L). Figure 5.5 shows that the contact angle of PVDF membranes decreased with an increase in treatment time at 80°C. For the membranes modified by MEA at concentrations of 10 and 12 mol/L, the contact angle decreased substantially after 5 h of modification. For the membranes modified by MEA at concentrations of 14 and 16 mol/L, the contact angle decreased much faster. However, after 9 and 5 h of amine treatment, the membranes became very fragile. Figure 5.6 also shows that the contact angle of PVDF membranes decreased with an increase in the amine treatment time.

Generally, it is quicker to obtain more hydrophilic membranes by increasing the concentration of MEA or raising the treatment temperature. The improvement in the hydrophilicity of the membranes should be attributed to the elimination of F^-. This is consistent with Ross's mechanism [2000]: a MEA solution with a higher alkalinity could provide more hydroxyl ions, which would accelerate the defluorination rate; similarly, increasing the treatment time and raising the temperature could increase the amount of fluorine eliminated.

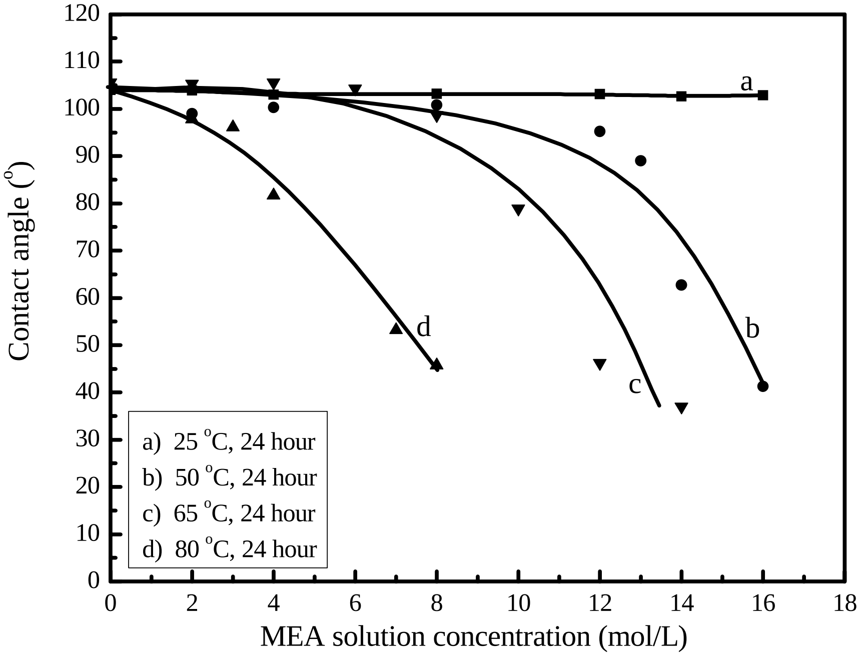

Figure 5.3 Effect of MEA concentration on the membrane contact angle at different treatment temperatures.

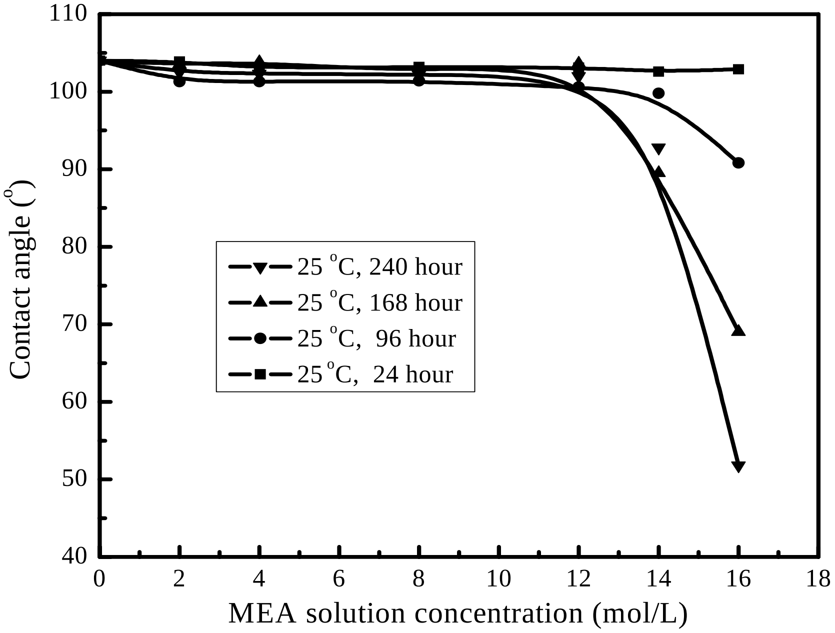

Figure 5.4 Effect of MEA concentrations on the membrane contact angle for amine treatment over different treatment time. Amine treatment temperature: 25°C.

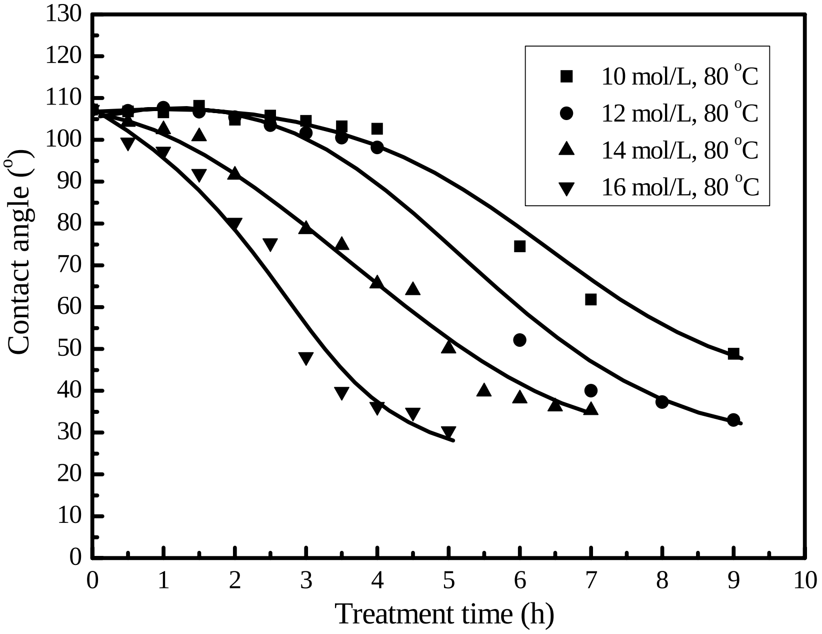

Figure 5.5 Effect of treatment time on the contact angle of membranes at given MEA concentrations. Amine treatment temperature: 80°C.

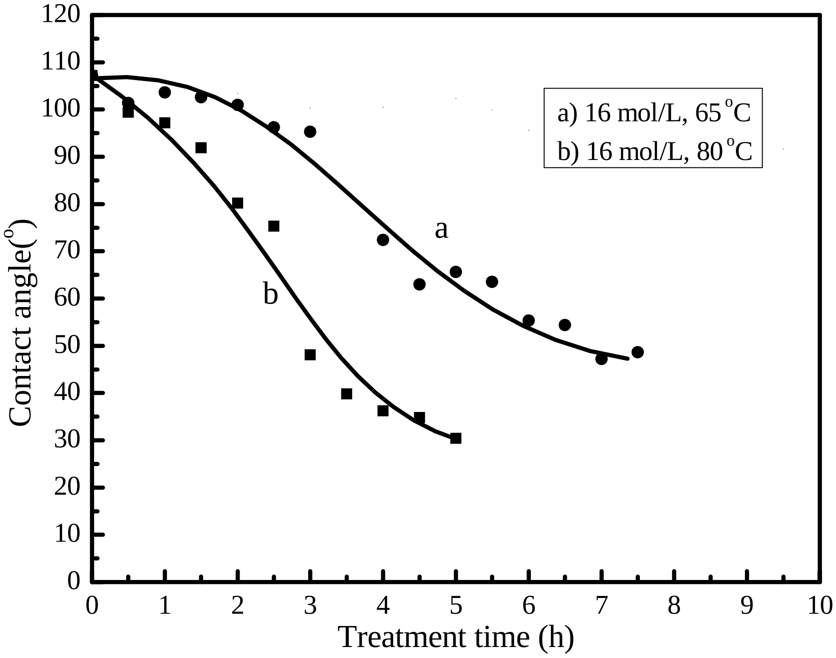

Figure 5.6 Effect of treatment time on the contact angle of membranes at different treatment temperatures. MEA concentration: 16 mol/L.

5.3.2.2 Significance of factors and interactions: factorial design experiment

Experimental results shown in Section 5.3.2.1 imply that there may be interactions (Conc. × Temp, Conc. × Time, Time × Temperature, Conc. × Temp × Time) among those factors. The interactions among factors are also possible variables influencing the hydrophilicity of the modified membranes. In order to find out the significance of the interactions, factorial design experiments were conducted.

The concentration of MEA, treatment temperature and treatment time were selected as the main variables. They are denoted as A, B and C respectively and varied at two levels, which are listed in Table 5.3. A full factorial experimental design including the interactions is presented in Table 5.4. All tests were repeated three times.

Table 5.3 Factors and levels.

Factor	Symbol	Low (-1)	High (+1)
MEA concentration	A	8 mol/L	16 mol/L
Treatment temperature	B	50^{o}C	80^{o}C
Treatment time	C	1 h	5 h

Table 5.4 Experiments of 2^3 complete factorial design: set up and results.

Treatment combination	Main effects			2-factor interactions			3-factor interactions	Contact angle (^{o})		
	A	B	C	AB	AC	BC	ABC	1	2	3
-1	-	-	-	+	+	+	-	100	101.5	97.1
C	-	-	+	+	-	-	+	100.7	101.1	100.2
B	-	+	-	-	+	-	+	96.8	94.4	98.7
BC	-	+	+	-	-	+	-	91.8	94.2	92.4
A	+	-	-	-	-	+	+	96.4	94.9	98.3
AC	+	-	+	-	+	-	-	73.2	68.4	72.2
AB	+	+	-	+	-	-	-	96.1	95.2	87.5
ABC	+	+	+	+	+	+	+	44.3	40.7	49.1

An analysis of variance (ANOVA) was employed to determine the relative significance of various factors and interactions, because it can demonstrate whether the observed variations in the response result from alteration of level adjustments or experimental errors. The construction of ANOVA table needs total sum of squares (TSS), sum of squares (SS), mean square (MS, variance) and associated *F*-value. The procedure to construct the ANOVA table is given in Appendix C.

Table 5.5 ANOVA table of factorial design.

Source of variation	Sum of Squares (SS)	Degree of freedom (df)	Mean Square (MS)	F-Value
A	2111.3	1	2111.3	286.4
C	1268.8	1	1268.8	82.6
A×C	765.0	1	765.0	38.5
B	2585.5	1	2585.5	349.6
A×B	1818.3	1	1818.3	247.2
B×C	503.3	1	503.3	18.6
A×B×C	465.5	1	465.5	16.0
Error	387.0	16	24.2	
Total	9904.5	23		

The *F*-value test is used to identify significant factors and interactions. *F* values are initially extracted from statistical tables at various risks (α_2). If the extracted *F*-value is smaller than the calculated value, the statistical significance of the effect will be considered [Sadrzadeh, 2007]. For α=0.01 (confidence interval, 99%), tabulated *F* value is $F_{1,16}$=8.531. ANOVA reveals that the calculated *F* values, which were calculated by equation C.17 (Appendix C) and listed in Table 5.5, exceed the tabulated value. It implies that the variance of all factors and interactions were significant compared with the variance of error, and all of them had significant effect on the response--hydrophilicity of PVDF membranes.

5.3.3 Filtration experiments: modified porous PVDF membranes

The filtration performance of modified PVDF membranes is also an important index to characterize the effectiveness of the modification.

The pure water permeation flux (J_{pwp}), rejection rate (*R*) on Dextran 266,000 and the fouling resistance [$R_{af} = \dfrac{J_{ps}}{J_{pwp}}$, the ratio of permeation flux obtained with the aqueous dextran solution (J_{ps}) over the pure water permeation flux] were used to evaluate the performance of modified membranes.

Figure 5.7 shows that the amine treatment did not affect the rejection rate significantly, which indicated that the modification did not have any significant impact on the mean pore size of the skin layers of the porous membranes. As shown in Figure 5.8, R_{af}

increased when the treatment time or the treatment temperature was increased. This implied that the fouling resistance of the modified microporous membranes was improved as a result of amine treatment. Because the fouling of hydrophobic membrane is usually resulted from the strong hydrophobicity of membranes [Liu et al., 2006], the improvement of fouling resistance of the modified membranes indicated that the PVDF membranes became more hydrophilic due to the amine treatment, which agrees with the results in contact angle studies: the hydrophilicity of modified membranes could be improved when more F^- of polymer backbone was eliminated. However, J_{pwp} decreased when the treatment time or the treatment temperature was increased, as shown in Figure 5.9. The same observations can be made for other treated membranes, as shown in Figures 5.10 – 5.15.

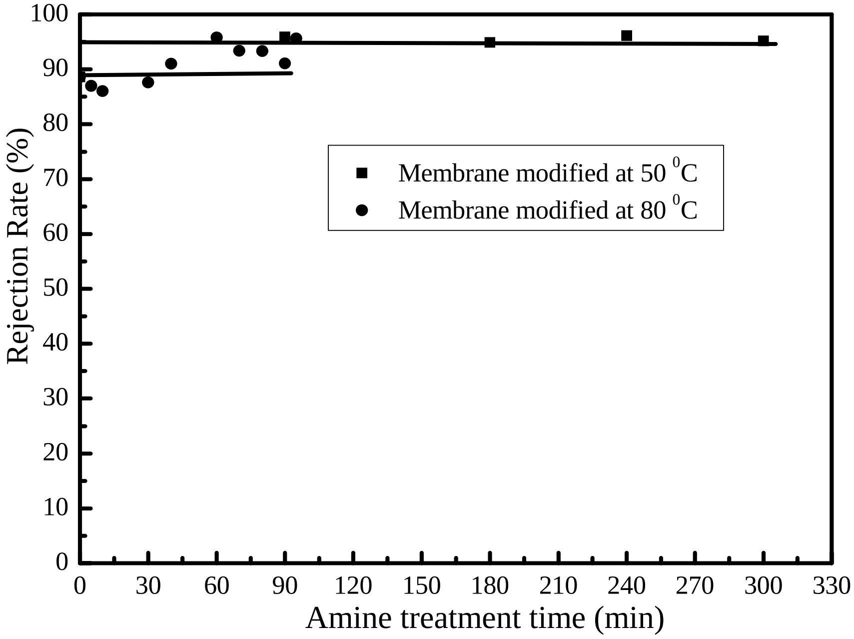

Figure 5.7 Rejection of Dextran solution with MEA treated PVDF membranes. MEA concentration: 16 mol/L. Transmembrane pressure for filtration tests: 100 kPa.

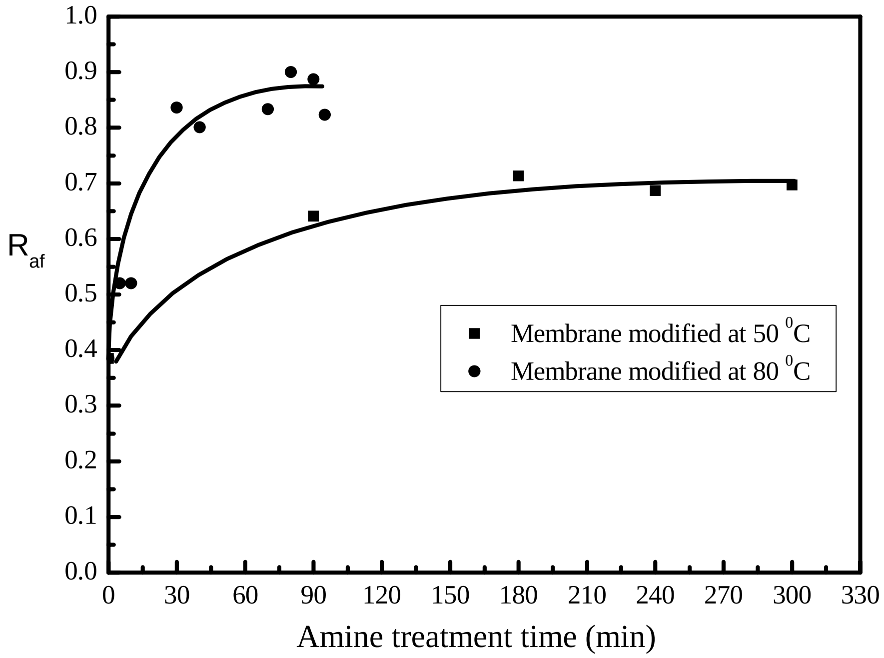

Figure 5.8 Fouling resistance of the MEA treated PVDF membranes. Amine treatment and filtration conditions are same as the conditions in Figure 5.7.

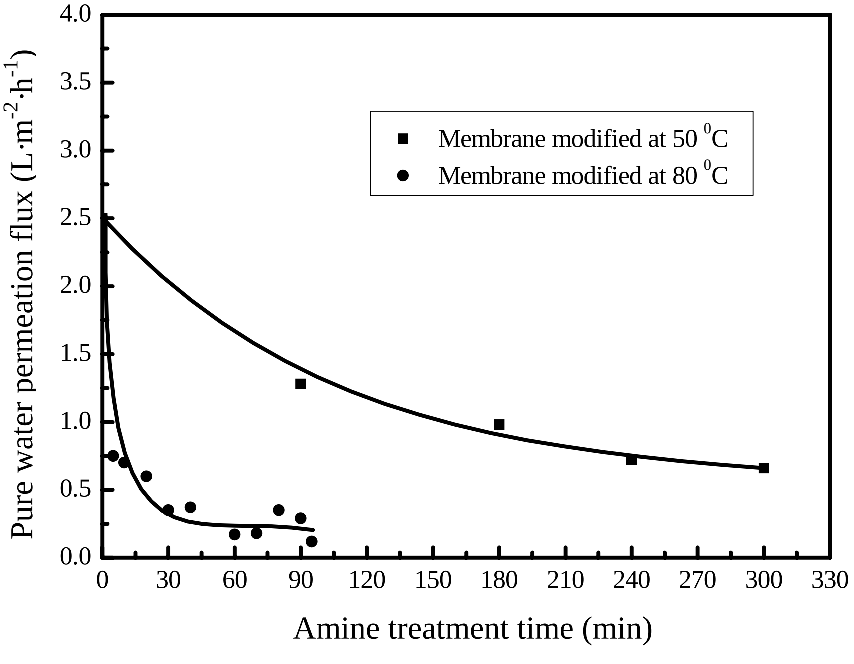

Figure 5.9 Pure water permeation flux of membranes treated with MEA vs. treatment time. Amine treatment and filtration conditions are same as the conditions in Figure 5.7.

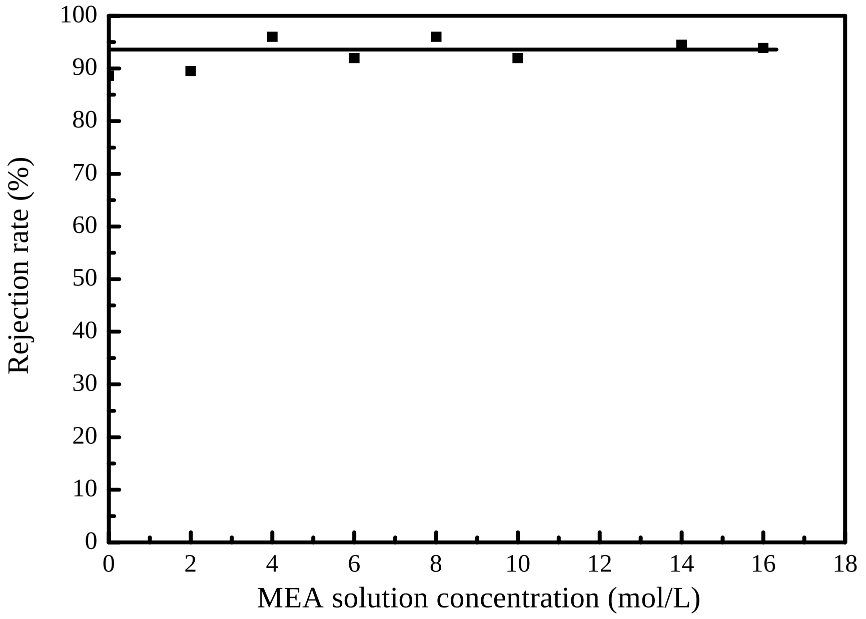

Figure 5.10 Rejection of Dextran solution with MEA treated PVDF membranes at different concentrations. Amine treatment time: 90 min, amine treatment temperature: 90°C. Transmembrane pressure for filtration tests: 100 kPa.

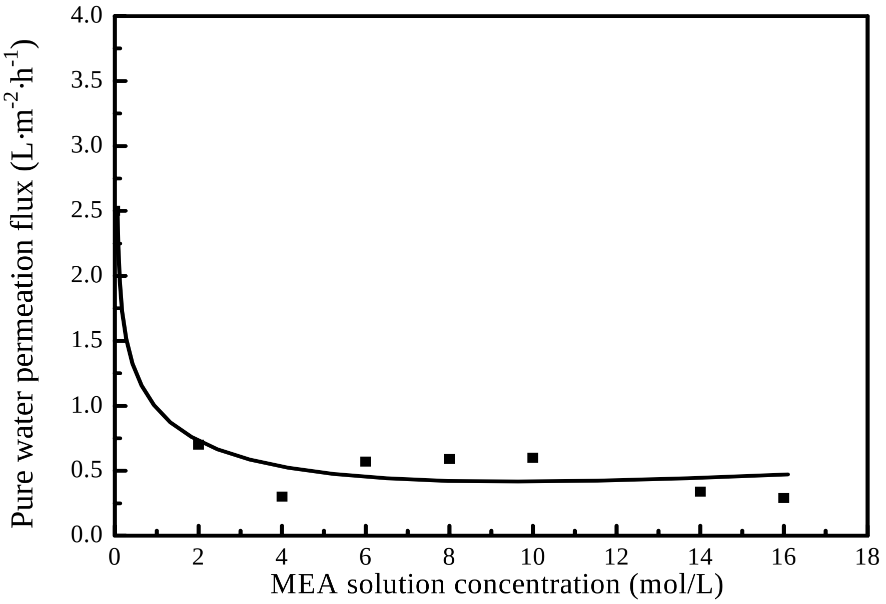

Figure 5.11 Pure water permeation flux of membranes treated with MEA at different concentrations. Amine treatment and filtration conditions are same as the conditions in Figure 5.10.

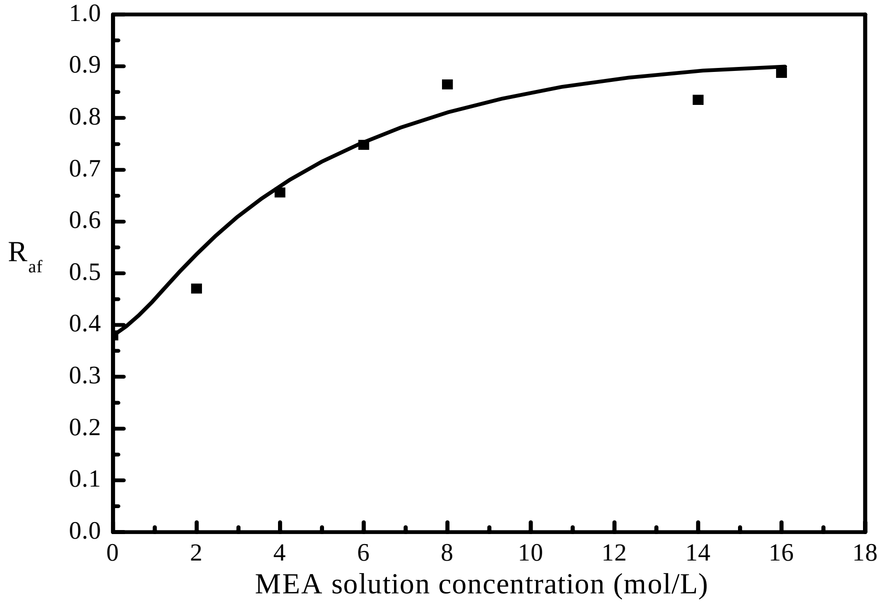

Figure 5.12 Fouling resistance of the MEA treated PVDF membranes. Amine treatment and filtration conditions are same as the conditions in Figure 5.10.

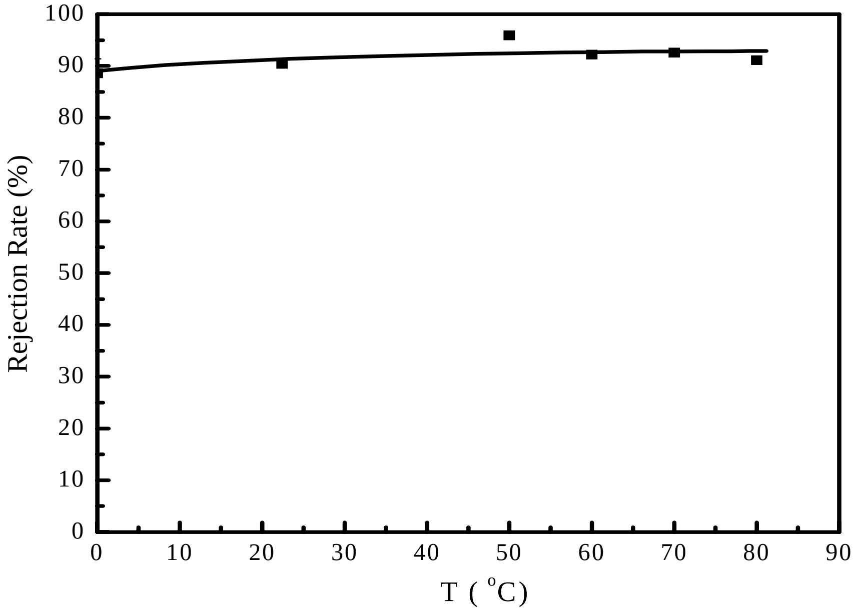

Figure 5.13 Rejection of dextran solution with MEA treated membranes at different temperature. Amine treatment time: 90 min, MEA concentraiton: 16 mol/L. Transmembrane pressure for filtration tests: 100 kPa.

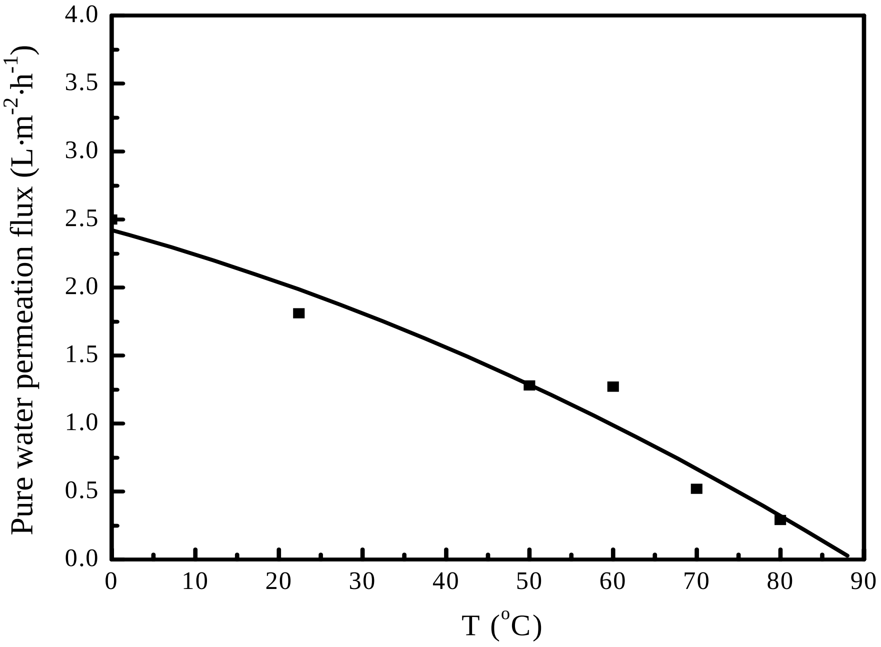

Figure 5.14 Pure water permeation flux of MEA treated PVDF membranes. Amine treatment and filtration conditions are same as the conditions in Figure 5.13.

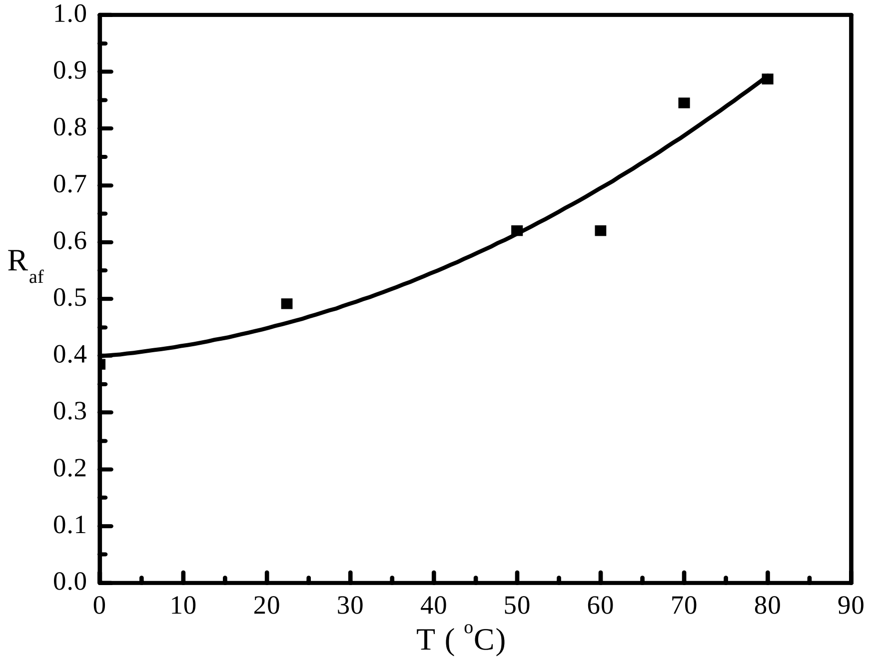

Figure 5.15 Fouling resistance of the MEA treated PVDF membranes. Amine treatment and filtration conditions are same as the conditions in Figure 5.13.

The decrease of J_{pwp}, which was not expected, implies that the structures of modified membranes changed. The cross-sectional morphologies of the membranes were examined with scanning electron microscopy (SEM). Figures 5.16 – 5.18 illustrate the structures of the original PVDF membrane, the membrane modified with 16 mol/L MEA solution at 80°C for 40 min, and the membrane modified by 16 mol/L MEA solution at 80°C for 90 min. Both the porous top layers that offer size exclusion capabilities and the sponge-like support layers do not show any significant difference before and after amine treatment. However, the macrovoid-like support layers in the modified membranes collapse, and this is more obvious after a longer period of amine treatment, as shown in Figures 5.17 and 5.18. The collapsing of the macrovoid-like structures indicates that the mechanical strength of the macrovoid-like support layers becomes weak after amine treatment. Although the macrovoid-like support layers do not influence the exclusion capability of the microporous membranes, their collapse can increase the mass transfer resistance within the membranes. As a result, the value of J_{pwp} decreased.

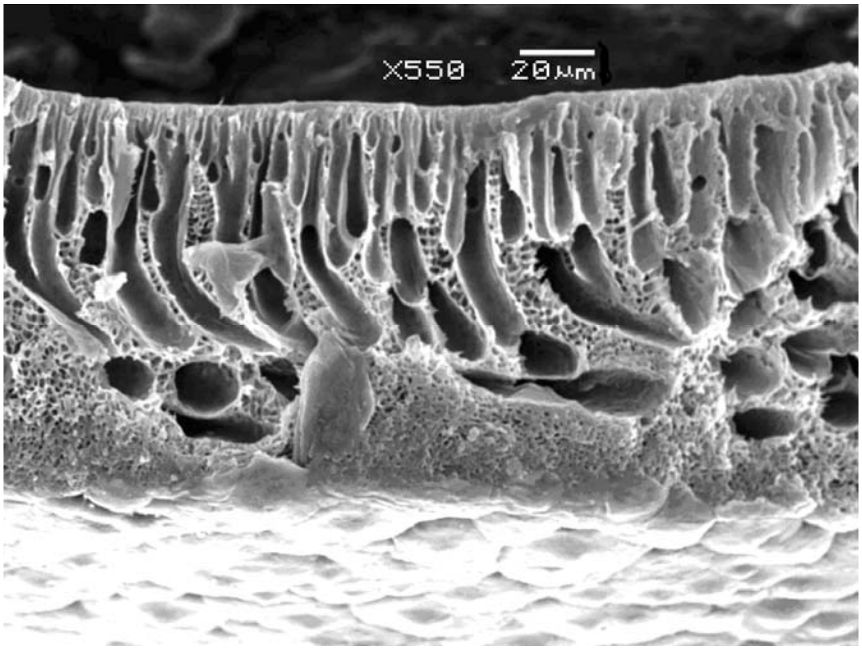

Figure 5.16 Cross section of original PVDF microporous membrane.

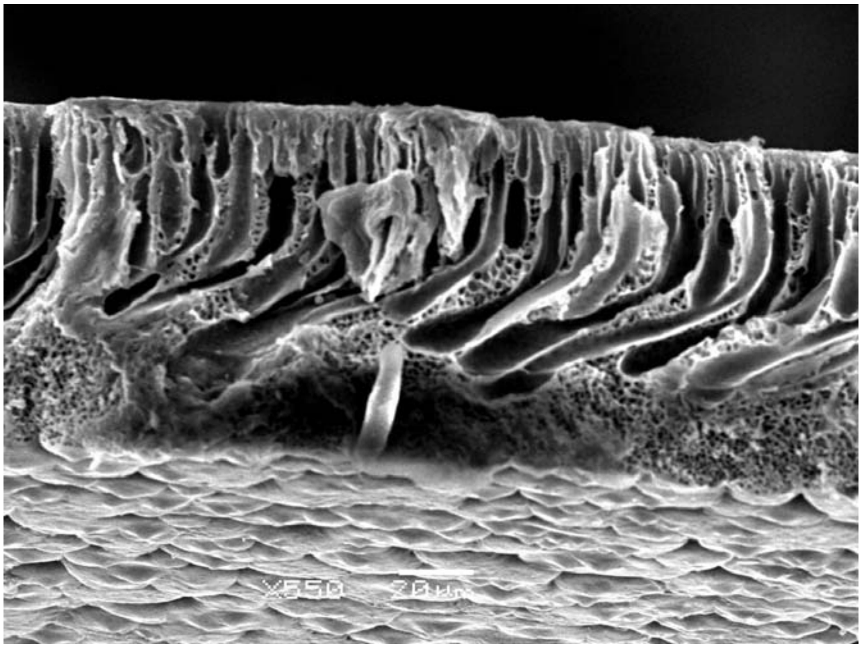

Figure 5.17 Cross section of membrane modified at 80^{o}C for 40 min by 16 mol/L MEA solution.

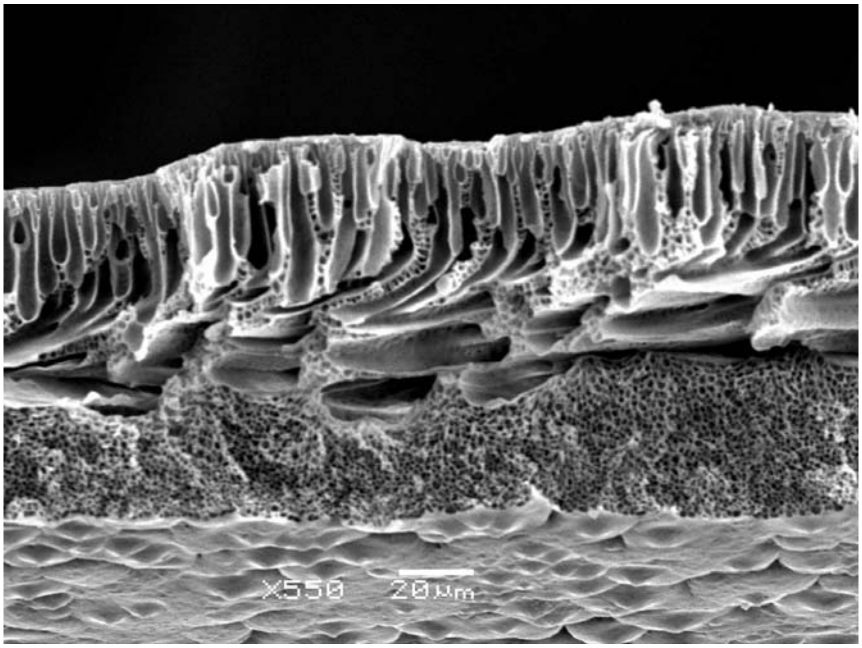

Figure 5.18 Cross section of membrane modified at 80^{o}C for 90 min by 16 mol/L MEA solution.

5.4 Conclusions

Amines were used to treat PVDF membranes in order to achieve more hydrophilic membranes. Contact angle studies and filtration experiments were carried out to evaluate the modified membranes. MEA concentration, treatment time, treatment temperature and the interactions among these factors affected the modification of membranes significantly.

FT-IR and EDAX element analysis illustrated that defluorination occurred during the amine treatment. Conjugated C=C and C=O double bonds appeared at the modified PVDF polymer backbones. After amine treatment, the hydrophilicity and the fouling resistance of the modified membranes improved. And the improvement of the hydrophilicity of modified membranes will benefit the assembly of hollow fiber membrane module by tubesheet potting.

The amine treatment did not have any significant impacts on the structures of the skin layers of modified membranes. However, the excessive amine treatment damaged the macrovoid-like structure. This increased the mass transfer resistance within the membranes. From this perspective, more work should be carried out in future.

Chapter 6

Application of microporous PVDF membranes for vacuum membrane distillation

---

6.1 Introduction

Scarcity of drinking water has been a problem in many arid regions for years. The shortage of water is a major obstacle for the development of agriculture, economics and technologies. Desalination of seawater and brackish water has been the most promising method to produce fresh water for decades [Bruggen, 2003].

Nowadays membrane distillation (MD) has been well recognized as a potential desalination technology for fresh water production [Khayet, 2004]. When vacuum is applied in the permeate side, the MD process is termed as vacuum membrane distillation (VMD). The mass transfer in VMD can be characterized by the following steps: vaporization of the more volatile compounds at the liquid/vapor interface; diffusion of vapor through the membrane pores [Bandini and Sarti, 1999; Wirth and Cabassud, 2002]. As shown in Figure 6.1, the membrane acts as a physical support for the vapor/liquid interface. The evaporation rate of water was expected to be influenced by both the heat and mass transfer resistances in the liquid phase at different extent because of the polarization effects [Bandini, 1997]. Therefore, mass transfer through the membrane, heat and mass transfer through the liquid phase are the main parameters determining the performance of VMD [Khayet, 2004].

As mentioned previously, hollow fibers offer many advantages over other membrane configurations. The application of hollow fibers in membrane distillation is promising as well. However, the pressure build-up in the bores of the fibers, which can reduce the driving force for the permeation, must be considered and investigated.

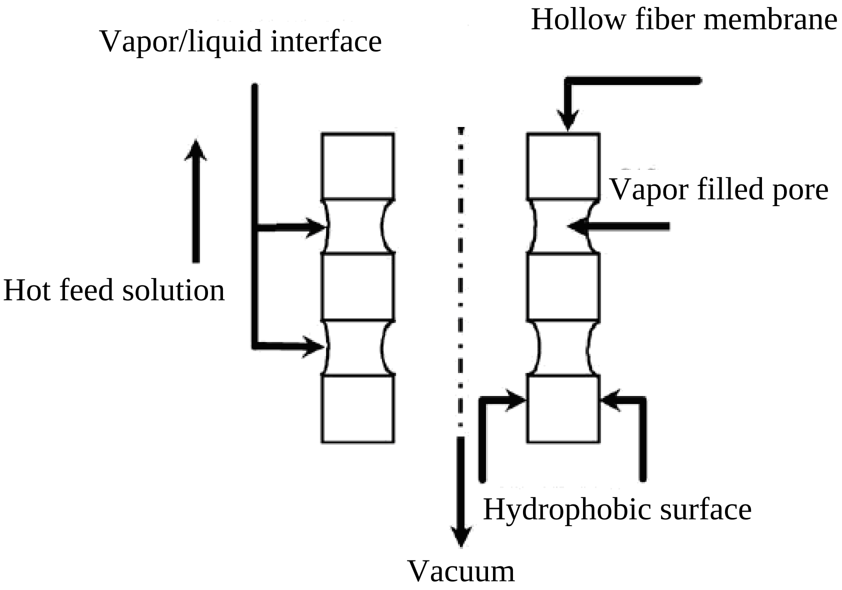

Figure 6.1 Vacuum membrane distillation [Li and Sirkar, 2005].

The main objective of this chapter was to perform a detailed analysis of VMD by hollow fiber PVDF membranes for desalination, and to get an insight into how to improve the process performance. The effects of membrane permeability, temperature, NaCl concentration and feed flowrate were evaluated. The effects of the interactions among these variables were also investigated.

6.2 Experimental

6.2.1 Hollow fiber module preparation

To prepare PVDF membranes, a predetermined amount of NMP and PVDF Kynar 741 polymer were mixed in a 1-liter flask. The solution was heated to $60^{o}C$ to facilitate the dissolution of PVDF. During this process, the flask was sealed to prevent solvent loss from evaporation. The PVDF solution was then transferred into a stainless steel dope tank and kept in the tank for about 36 h at room temperature to remove the air bubbles entrapped in the polymer solution.

PVDF hollow fiber membranes were fabricated via the dry/wet phase inversion method, which has already been discussed in Chapter 4. All hollow fibers fabricated were kept in the water bath for at least 7 days to remove residual NMP completely. Finally, the hollow fiber membranes were dried at ambient conditions before being used to assemble hollow fiber membrane modules. The inner diameter of the hollow fiber membrane modules was 4.80 mm. The number of hollow fibers assembled in each module was 3. The diameters of hollow fiber membranes were measured with a microscope (Cole-Parmer, Model 3894). The average pore size (r) and the ratio of the porosity to pore length that takes into account the tortuosity of the membrane pores (ε/l) were determined with the gas permeation method; the experiment procedure has been described before.

6.2.2 Vacuum membrane distillation

The experimental setup for VMD is shown schematically in Figure 6.2. The feed solution (i.e., aqueous NaCl solution) was circulated through the feed side of the membrane. The volume of the feed tank was approximately 1.25 liter. The temperature of the feed solution was monitored at the feed tank and the inlet of the hollow fiber module. The feed flowrate was set with a rotameter (Cole–Parmer, PTFE).

The permeate side of the hollow fiber module was connected to a vacuum pump, and the permeate vapor was condensed and collected in a liquid nitrogen cold trap. The vacuum pump was used to provide the driving force for permeation and the pressure at the permeate outlet was measured with a digital vacuum gauge (V664, Supco).

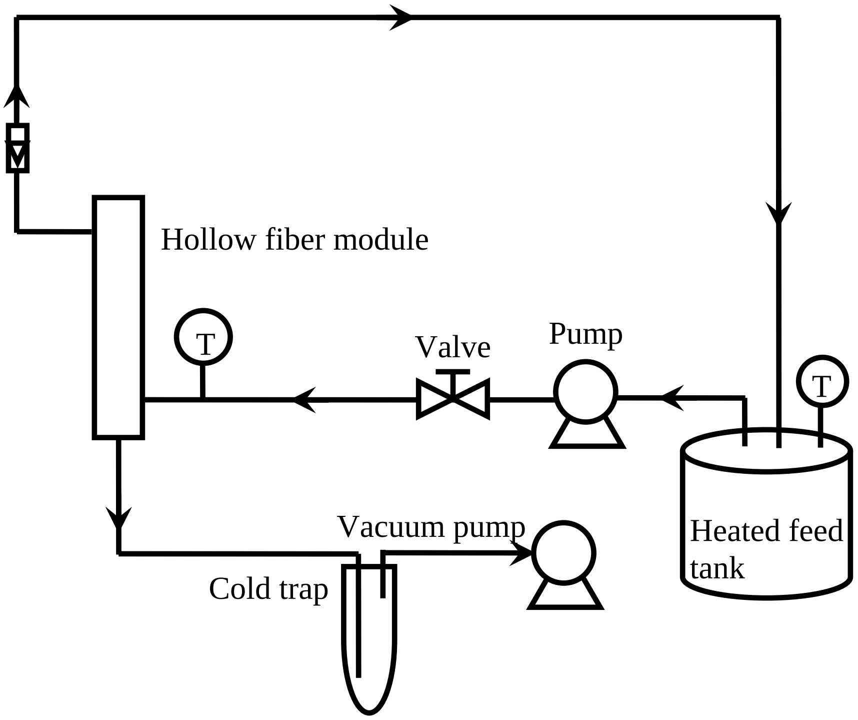

Figure 6.2 Schematic representation of vacuum membrane distillation apparatus.

6.3 Results and discussion

The mass transfer in VMD can be described using an overall mass transfer coefficient, which is the reciprocal of the overall mass transfer resistance. Generally, three main resistances are involved in the VMD process: mass-transfer resistance through the membrane, mass transfer and heat transfer resistances within the liquid phase [Bandini and Sarti, 1999]. Usually, the heat transfer resistance within the liquid phase has a considerable effect on the performance of VMD, and the heat transfer coefficient can be estimated from empirical correlations [Li, 2005]. However, in this study, because a large amount of feed was used compared to the amount of membrane distilled water permeate, the heat transfer resistance in this case can be neglected and the system can be considered to be isothermal. Therefore, the overall mass transfer is determined by the mass transfer in the liquid phase and the mass transfer across the membrane:

$$\frac{1}{K_{\mathrm{ov}}} = \frac{1}{(H \cdot K_m \cdot M_{H_2O}^{-0.5})} + \frac{1}{K_f} \tag{6.1}$$

where K_{ov} is the overall mass transfer coefficient, H is the Henry's law constant. $(K_m \cdot M_{H_2O}^{-0.5})$ and K_f are the mass transfer coefficients in the liquid phase and across the membrane, respectively; they are dimensionally different. The mass transfer coefficient through the membrane depends on the membrane permeability K_m, which will be discussed later. The mass transfer coefficient through the liquid phase is influenced by the hydrodynamic conditions of the feed flow.

6.3.1 Pure water experiments

6.3.1.1 Effects of membrane permeability and temperature on VMD performance

As discussed in section 2.3.1, vapor transport through microporous membranes depends upon the pore size (r) of the membrane relative to the mean free path (λ) of the vapor molecules. When the membrane has pores comparable in size to the mean free path, the permeation flux N (mol·m^{-2}·s^{-1}) through the membrane can be described by Knudsen diffusion-viscous flow [Izquierdo-Gil and Jonson, 2003]:

$$N = \frac{1}{RT}\left[\frac{2\varepsilon r}{3l} \cdot \left(\frac{8RT}{\pi M}\right)^{1/2} + \frac{\varepsilon r^2}{8\mu l} \cdot \overline{P}\right] \cdot \Delta P \tag{6.2}$$

where R is the gas constant, T is the temperature, l is the effective pore length, ε is porosity, $\overline{P}$ is the average pressure of the vapor in the membrane pores, ΔP is the pressure difference across the membrane, μ is the viscosity of the vapor, and M is the molecular weight of vapor permeant.

When the membrane pore size is below the mean free path of the permeating vapor, Knudsen diffusion will dominate the mass transport through the membrane [Banat and Simandl, 1996], and the molar permeation flux is given by [Cabassud and Wirth, 2003]:

$$N = \frac{K_m}{\sqrt{M_i}} \cdot \Delta P = \frac{K_m}{\sqrt{M_i}} \cdot (P_{f,i} - P_{p,i}) \tag{6.3}$$

where $P_{f,i}$ and $P_{p,i}$ are the vapor pressures of the permeating species at the feed and permeate sides, respectively. The membrane permeability, K_m is related to structural properties of the membrane:

$$K_m = \frac{2\varepsilon r}{3l}\sqrt{\frac{8}{\pi RT}} \tag{6.4}$$

The permeability coefficient (K_m) and the mean pore size (r) can be evaluated by the gas permeation method, which has been described in Chapters 2 and 4. Figure 6.3 shows the nitrogen permeance of the membranes used in this membrane distillation experiment. The procedure for the gas permeance measurements has been described previously. The values of K and c in equation 2.6 can be calculated by data fitting. From the values of K and c, the mean model pore radius (r) can be calculated by equation 2.7. The effective surface porosity ε and the effective pore length l cannot be evaluated individually, but their ratio (ε/l) can be obtained using equation 2.8. Table 6.1 summarizes these data as well as the length, the internal and external diameters of the hollow fiber membranes. While the fiber dimensions of the three membranes studied here are not much different. Membrane 3 has much smaller pore sizes than the other two membranes.

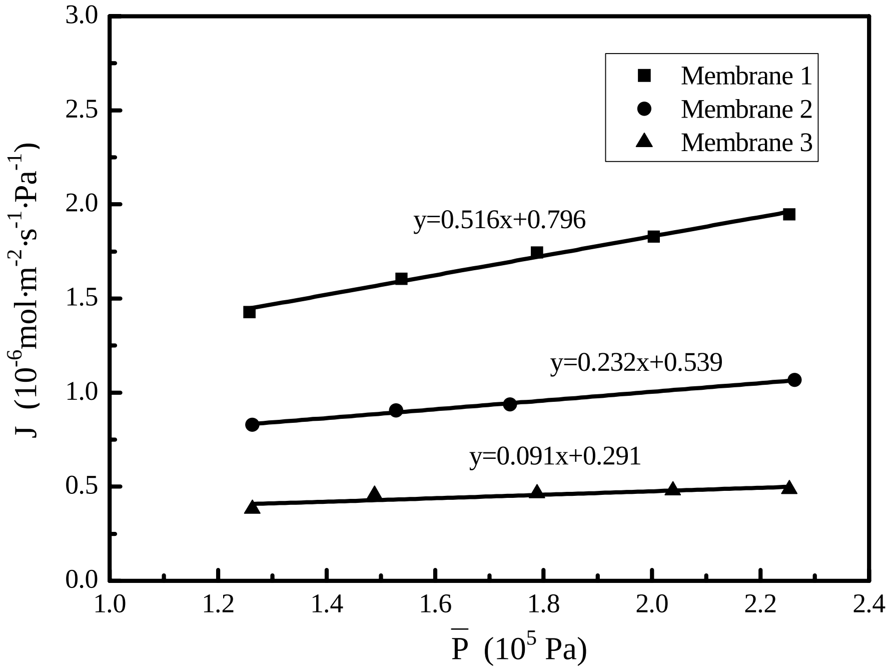

Figure 6.3 Nitrogen permeance vs. average pressure in the membranes pores.

Table 6.1 Characteristics of the hollow fiber membranes.

Membrane	Length(cm)	Outer diameter (mm)	Inner diameter (mm)	Wall thickness (mm)	Mean pore size (μm)	ε/l (m^{-1})
1	28.10	0.655	0.249	0.203	0.282	22.2
2	28.50	0.730	0.224	0.253	0.225	20.9
3	28.70	0.770	0.231	0.269	0.0451	69.5

The mean free path of a gas can be calculated by equation 2.2. Table 6.2 shows the calculated mean free path of water vapor molecules at different temperatures. The vapor pressure at the vapor/liquid interface is assumed to be equal to the saturated vapor pressure at a given temperature and the permeate pressure taken as 1000 Pa, which is close to the experiment conditions.

Table 6.2 Mean free path of water vapor molecule.

Temperature (^{o}C)	30	40	50	60	70	80
Mean free path (μm)	3.65	3.45	3.40	3.40	3.44	3.50

The mean free path of water vapor molecules are shown to be indeed much bigger than the membrane pores, which justifies the assumption that the water vapor transport through membrane is by Knudsen diffusion. This means the equation 6.3 can be used to describe the mass transfer in the membrane. For vacuum membrane distillation, the following equation is applicable.

$$N = \frac{K_m}{\sqrt{M_{H_2O}}} \cdot \Delta P = \frac{K_m}{\sqrt{M_{H_2O}}} \cdot (P_{sat} - P) \qquad (6.5)$$

where P_{sat} is the saturated vapor pressure at temperature T, P is the permeate pressure, and M_{H_2O} is the molar mass of water. The membrane permeability for water vapor permeation can be obtained from the intercept c of nitrogen permeance vs. average pressure plot shown in Figure 6.3.

$$K_m \big/ M_{H_2O}^{0.5} = c \cdot (\frac{M_{N_2}}{M_{H_2O}})^{0.5} \qquad (6.6)$$

It was found that the ($K_m \big/ M_{H_2O}^{0.5}$) values for water vapor permeation through membranes 1 -- 3 are 0.988×10^{-6}, 0.672×10^{-6} and 0.363×10^{-6} mol·m^{-2}·s^{-1}·Pa^{-1}, respectively.

These three membranes were used to investigate the effects of feed temperature on the permeation flux, using pure water as feed liquid, for which there is no mass transfer resistance within the liquid phase. The feed temperatures varied between 30.0 and 80.0^{o}C at a feed flowrate of 0.60 L/min. Figure 6.4 shows that the permeation flux could be significantly enhanced by raising the feed temperature due to increased driving force. According to the Antoine equation, the saturated vapor pressure increases with temperature significantly [Li and Sirkar, 2005]:

$$P_{sat}^{o} = exp\left(23.1964 - \frac{3816.44}{T - 46.13}\right) \qquad (6.7)$$

where P_{sat}^{o} is the saturated vapor pressure of pure water in Pa, and T is temperature in K. According to equation 6.5, an increase in the saturated water vapor pressure over the liquid/vapor interface will increase the driving force across the membrane, resulting in an increase in the permeation flux. This is more clearly shown in Figure 6.5, where the permeation flux is plotted vs. the driving force. A linear relationship is obtained, with a correlation coefficient (R^2) over 0.99. This implies that the linear model is adequate and the mass transfer through the membranes is dominated by the Knudsen flow.

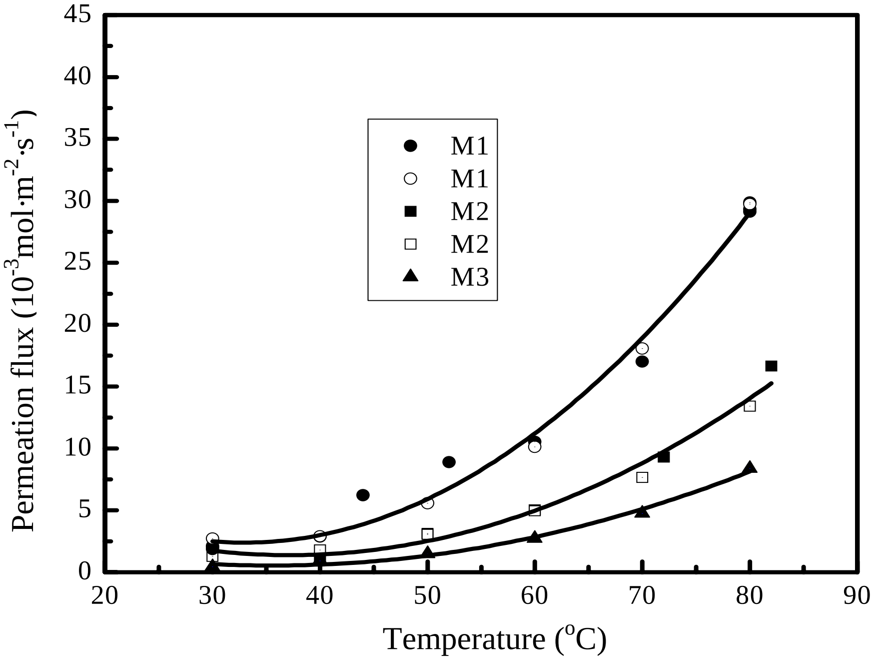

Figure 6.4 Permeation flux of pure water vs. temperature through the membranes. Feed flowrate: 0.60 L/min. Duplicate experiments with different membranes fabricated separately under the same conditions, were also carried out, and the results are represented by the open symbols.

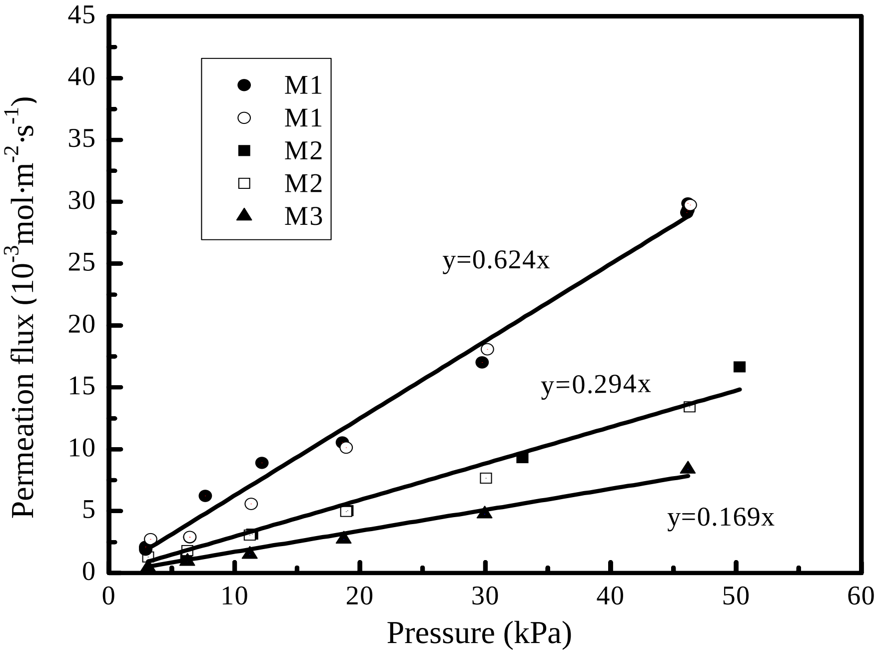

Figure 6.5 Permeation flux vs. driving force for vacuum membrane distillation with pure water.

For VMD with pure water, the overall mass transfer coefficient is expected to equal the membrane permeability. As shown in Figure 6.6, the calculated overall mass transfer coefficient, which uses a permeate pressure obtained with a Vacuum gauge at the permeate outlet of the hollow fiber module, increases with the increase of membrane permeability. However, these calculated overall mass transfer coefficients for VMD with the three hollow fiber membranes are found to be 0.624×10^{-6}, 0.294×10^{-6} and 0.169×10^{-6} mol·m^{-2}·s^{-1}·Pa^{-1}, respectively. These values are lower than the theoretical values predicted based on the N_2 gas permeation data. This is caused by the permeate pressure build-up, which results in a decrease in the actual driving force. This will be discussed in more detail in the following section that focus on permeate pressure build-up in the hollow fiber lumens.

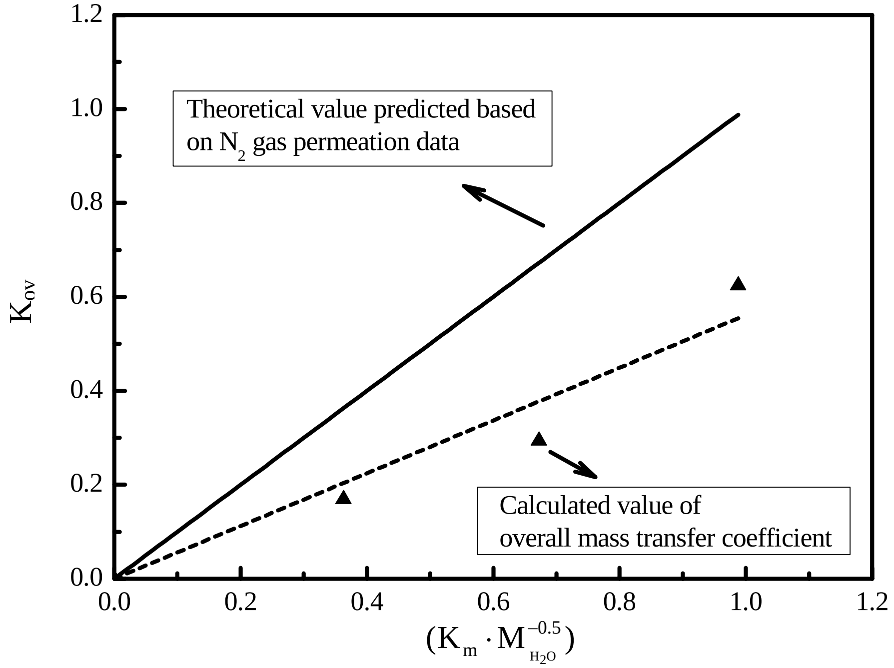

Figure 6.6 Overall mass transfer coefficient vs. membrane permeability (10^{-6} mol·m^{-2}·s^{-1}·Pa^{-1}).

6.3.1.2 Permeate pressure build-up in fiber lumen

A schematic of a hollow fiber for VMD is shown in Figure 6.7. The feed solution flows outside the fiber. One end of the fiber lumen is open to provide an outlet for the permeate vapor to exit the membrane module. Vacuum is applied at the open end of the fiber. Hollow fibers with small inner diameters may result in a large pressure drop in the bulk flow direction when the vapor flows in the bore of the fibers [Shao and Huang, 2006]. The permeate pressure increases from the open end to the dead end; that is, there is a pressure build-up in the fiber bores.

Based on the permeation equation and the Hagen–Poiseuille equation, a mathematical model can be developed to describe the permeate pressure build-up in the fiber bores with the following assumptions:

(1) The vapor mass transfer through the membrane is by Knudsen flow;

(2) Vapor behaves as an ideal gas;

(3) Isothermal process and there is no temperature polarization on the feed side;

(4) Vapor flow in the hollow fiber lumen is laminar;

(5) Radial flow is relative low to the axial flow;

(6) Steady state operation.

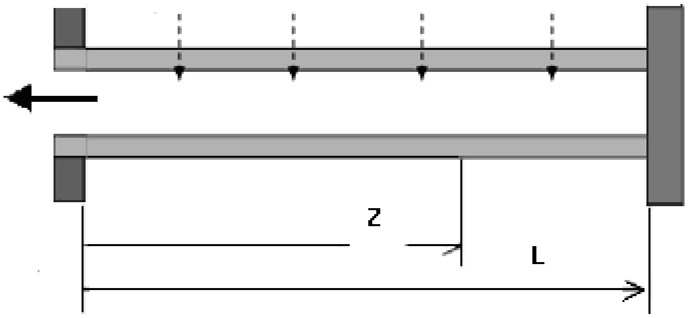

Figure 6.7 Schematic representation of permeation through a hollow fiber with shell side feed.

The permeate pressure in the hollow fiber lumens can be described by the Hagen–Poiseuille equation [Pan, 1983]:

$$\frac{d(P^2)}{dz} = \frac{256\mu RT}{n\pi d_i^4} F \tag{6.8}$$

where z is the distance the open end, P is the local pressure, F is the local molar flowrate of vapor, d_i is the inner diameter of the hollow fiber, n is the number of hollow fibers, and μ is the viscosity of water vapor at temperature T.

The local permeation flowrate can be described by the permeation equation:

$$\frac{dF}{dz} = -n\pi d_{\mathrm{o}} \frac{K_m}{\sqrt{M_{H_2O}}} \left(P_{sat} - P\right) \tag{6.9}$$

where d_o is the outer diameter of the hollow fibers. The boundary conditions for equations 6.8 and 6.9 are

$z = L \qquad F=0 \qquad dP/dz=0 \qquad P=P_e$

$z=0 \qquad F=F_o \qquad P=P_o$

where F_o is the total water vapor flowrate from the membrane unit, P_e and P_o are the vapor pressure at the dead end and the open end (i.e. module outlet), respectively. The value of P_o was determined using a vacuum gauge during VMD experiments.

The profiles of permeate pressure and flowrate can be determined by solving the above formulated ordinary differential equations. Polymath software was used to solve the differential equations for a given set of operating conditions (feed temperature T, outlet pressure P_o, product flowrate F_o) and the membrane properties (membrane permeability K_m, outer diameter d_o and inner diameters d_i). The viscosity (μ) of water vapor was obtained from the Handbook of Chemistry and Physics [Weast, 1976]. The initial values (F_o, P_o) used to solve the differential equations was specified at z=0. A trial-and-error method was used; when the calculated value of permeation flowrate matched the other boundary condition ($z=L$, $F=0$), then the equations were solved correctly, and the permeate pressure and flowrate profiles were obtained.

The profiles of the permeate pressure build-up and the permeation flowrate in the three different hollow fibers at different operating temperatures were presented in Figures 6.8 – 6.13, where the fiber length started from the open end of fibers as defined in the boundary conditions for equations 6.8 and 6.9. It can be seen that the permeate pressure build-up was more significant within 35% fiber length, and it increased slightly over 35% fiber length in membranes 1 and 2, which had high membrane permeabilities. Compared to membrane 1 and 2, the pressure build-up increased less significantly within 50% fiber length in hollow fiber membrane 3, which had a lower membrane permeability. It can also be observed that an increase in temperature will enhance the pressure build-up. These observations can be explained easily. As the flowrate profile shows, the permeation flowrate increases as the vapor flowed away from the dead end of the fibers and reached a maximum value at the open end [Shao and Huang, 2006]. With a higher membrane permeability, a higher flowrate will be achieved under a given driving force. At a higher temperature, the driving force will be greater, resulting in a larger flowrate. On the other hand, as the Hagen–Poiseuille equation shows, there will be a sharper pressure change at places where the permeation flowrate is high.

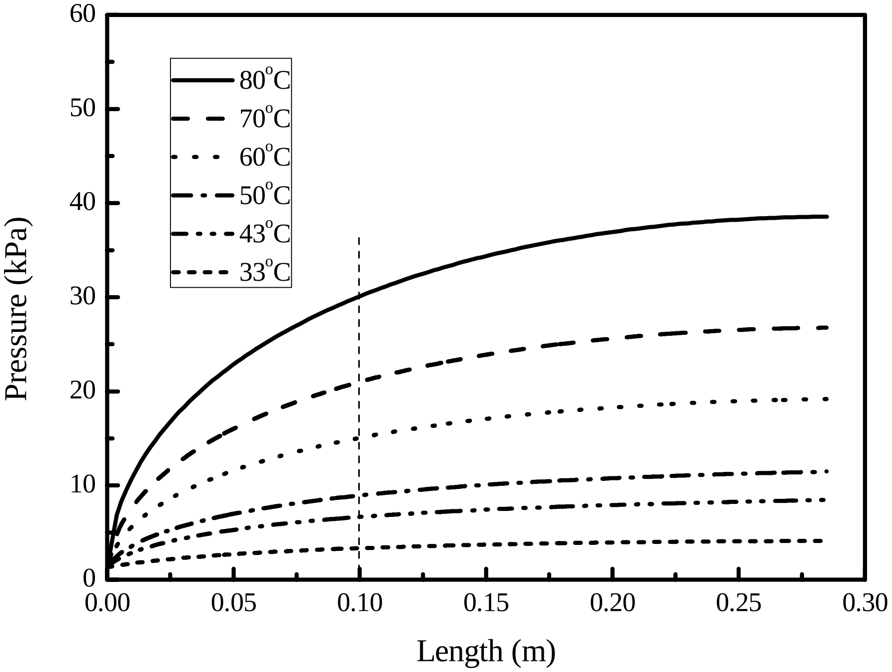

Figure 6.8 Pressure profile in fiber bores for membrane 1.

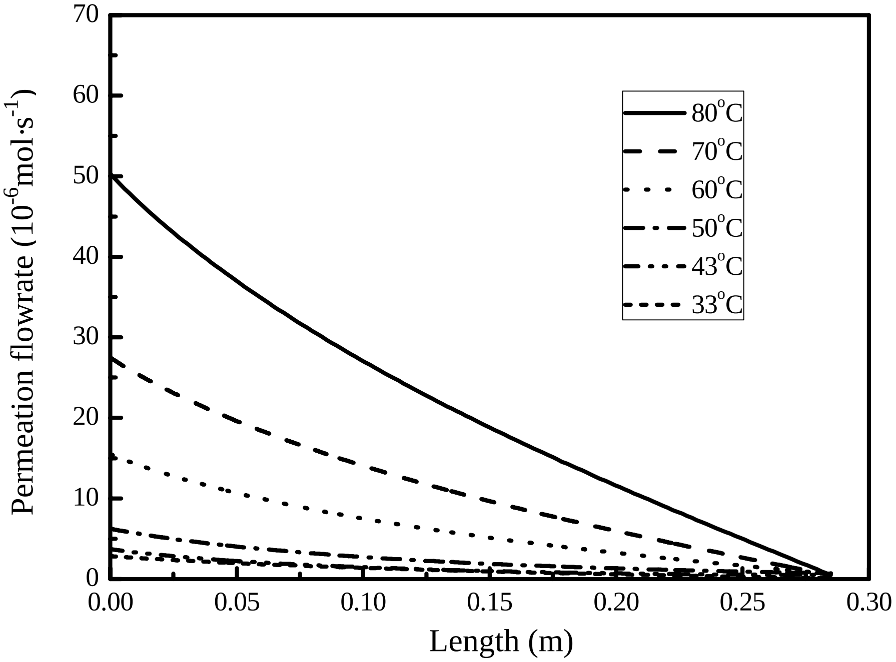

Figure 6.9 Flowrate profile in fiber bores for membrane 1.

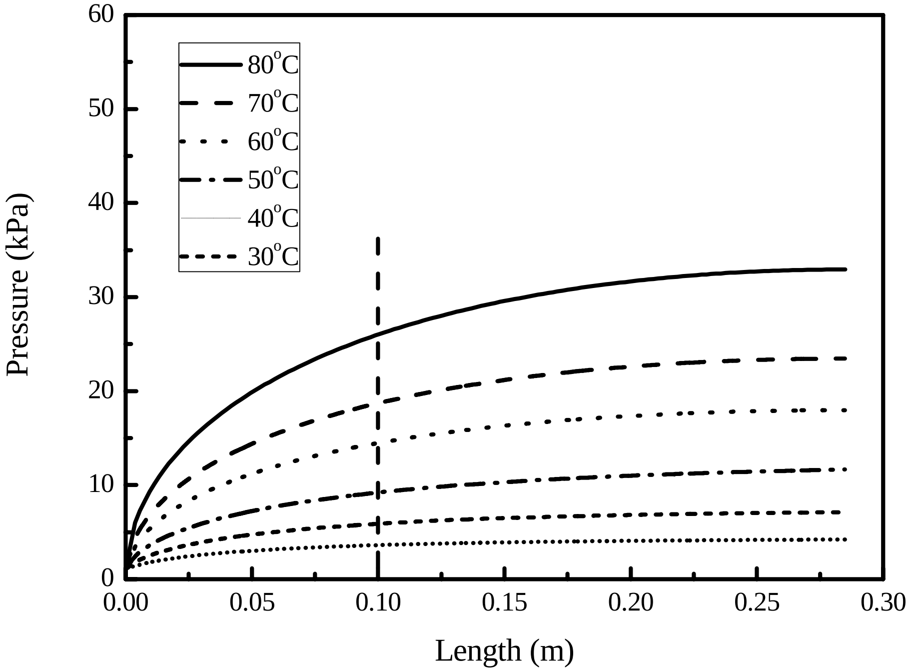

Figure 6.10 Pressure profile in fiber bores for membrane 2.

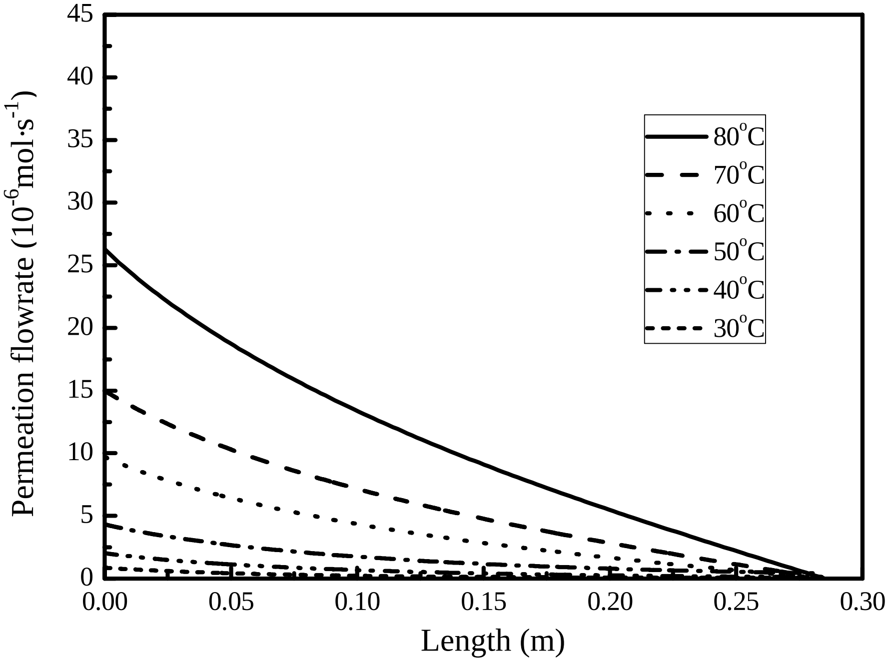

Figure 6.11 Flowrate profile in fiber bores for membrane 2.

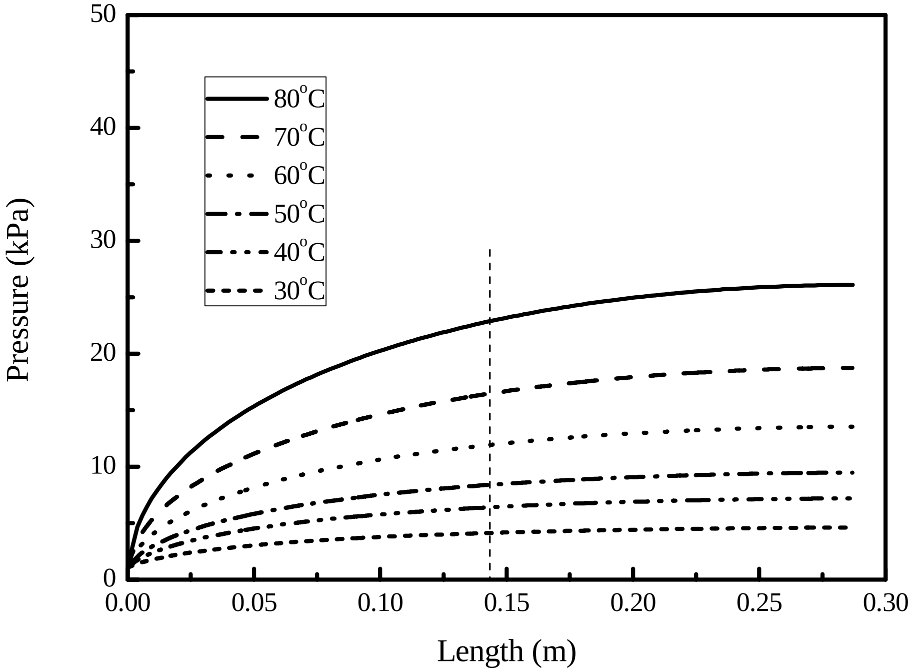

Figure 6.12 Pressure profile in fiber bores for membrane 3.

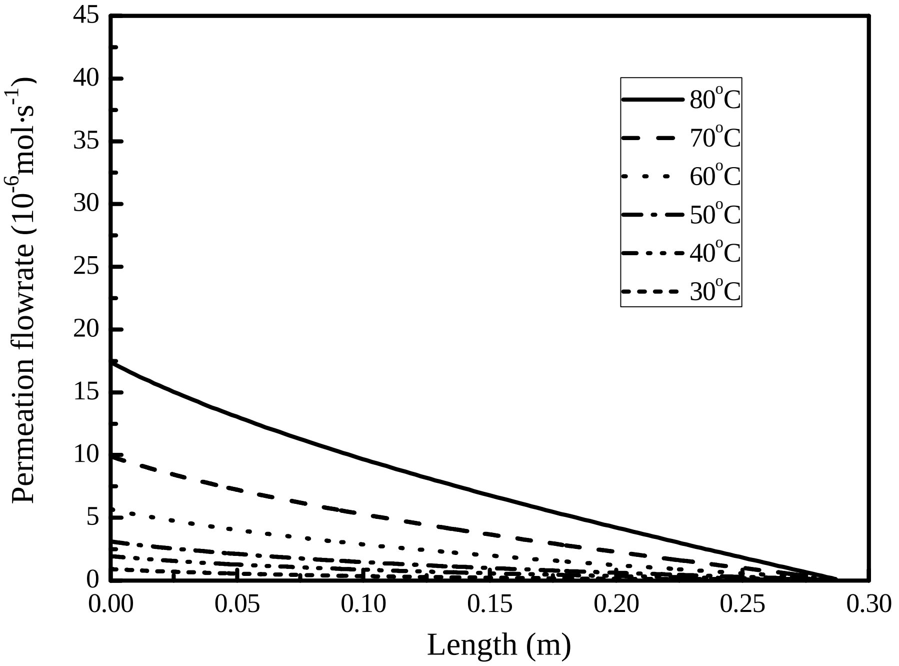

Figure 6.13 Flowrate profile in fiber bores for membrane 3.

The permeate pressure profiles illustrate that the permeate pressure reached a maximum P_e at the dead end ($z=L$). The maximum P_e at the dead end of a fiber is limited by the saturated vapor pressure P_{sat}. When the permeation rate is sufficiently high, P_e will reach P_{sat} and a maximum product flowrate (F_o) will be obtained. It can be evaluated based on an analytical solution.

By combining equations 6.8 and 6.9, the relationship between P and F can be obtained:

$$\frac{d(P^2)}{dF} = -\frac{256\mu RT}{n^2\pi^2 d_i^4 d_o} \cdot \frac{1}{K_m / M_{H_2O}^{0.5}} \cdot \frac{1}{\left(P_{sat} - P\right)} \cdot F \tag{6.10}$$

Integrating,

$$\int_{P_e}^{P_o} \left(2P_{sat}P - 2P^2\right) \cdot dP = -\frac{256\mu RT}{n^2\pi^2 d_i^4 d_o} \cdot \frac{1}{K_m / M_{H_2O}^{0.5}} \int_0^{F_O} F \cdot dF \tag{6.11}$$

When the dead-end pressure (P_e) equals to the saturated vapor pressure P_{sat}, equation 6.11 can be written as:

$$\int_{P_{sat}}^{P_o} \left(2P_{sat}P - 2P^2\right) \cdot dP = -\frac{256\mu RT}{n^2\pi^2 d_i^4 d_o} \cdot \frac{1}{K_m / M_{H_2O}^{0.5}} \int_0^{F_O} F \cdot dF \tag{6.12}$$

The theoretical maximum value of the product permeation flowrate (F_o) is given by:

$$F_{\mathrm{o}} = \left[-\frac{3n^2\pi^2 d_i^4 d_o}{128\mu RT} \cdot K_m / M_{H_2O}^{0.5} \cdot \left(3P_{sat}P_o^2 - P_o^3 - P_{sat}^3\right) \right]^{0.5} \tag{6.13}$$

If the permeate pressure build-up is negligible (for example, flat membranes and hollow fibers with larger diameters), the molar flowrate of permeate product can be evaluated from:

$$F_{\mathrm{o}}^{'} = K_m \cdot \mathrm{A} \cdot \Delta P = K_m / M_{H_2O}^{0.5} \cdot \mathrm{A} \cdot (P_{sat} - P) \tag{6.14}$$

where A is the membrane area, and P is the permeate pressure applied to the membrane unit.

Figures 6.14 – 6.16 illustrate the experimental and calculated permeate product flowrate for VMD with pure water using membranes 1 – 3, respectively. Clearly, the experimental data are far away from the theoretical values without pressure build-up, which are calculated from equation 6.14, but very close to the values calculated from equation 6.13. This indicates that the applicablility of the Hagen-Poiseuille equation for describing the pressure build-up in the fiber. The model can be used to estimate the performance of a VMD process.

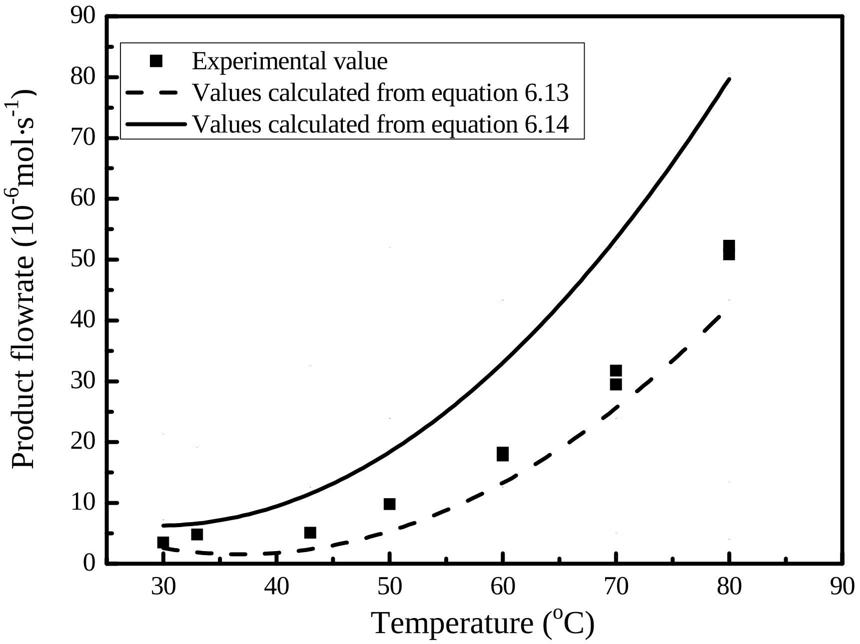

Figure 6.14 Permeate product flowrate for distillation with pure water using membrane 1. Feed flowrate: 0.60 L/min.

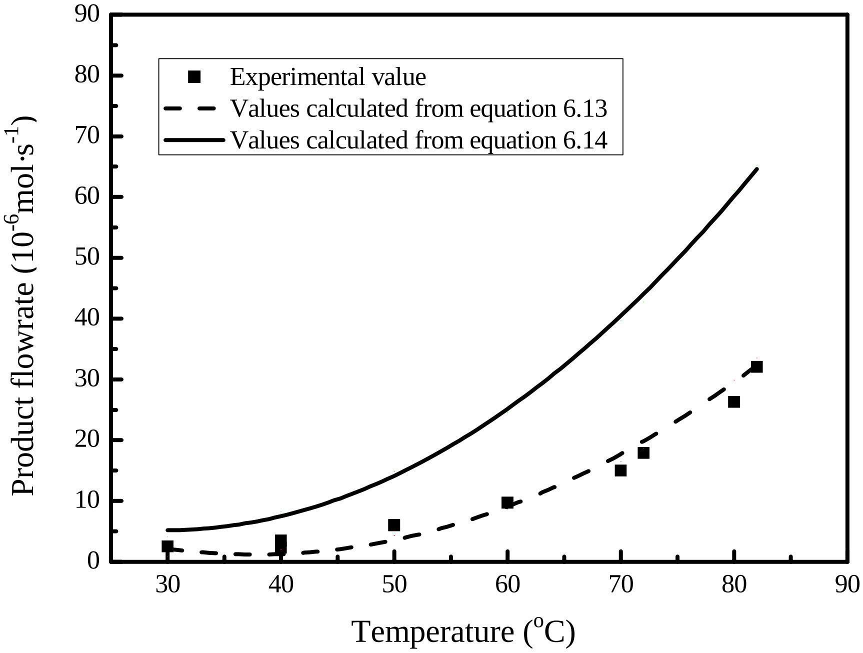

Figure 6.15 Permeate product flowrate for distillation with pure water using membrane 2. Feed flowrate: 0.60 L/min.

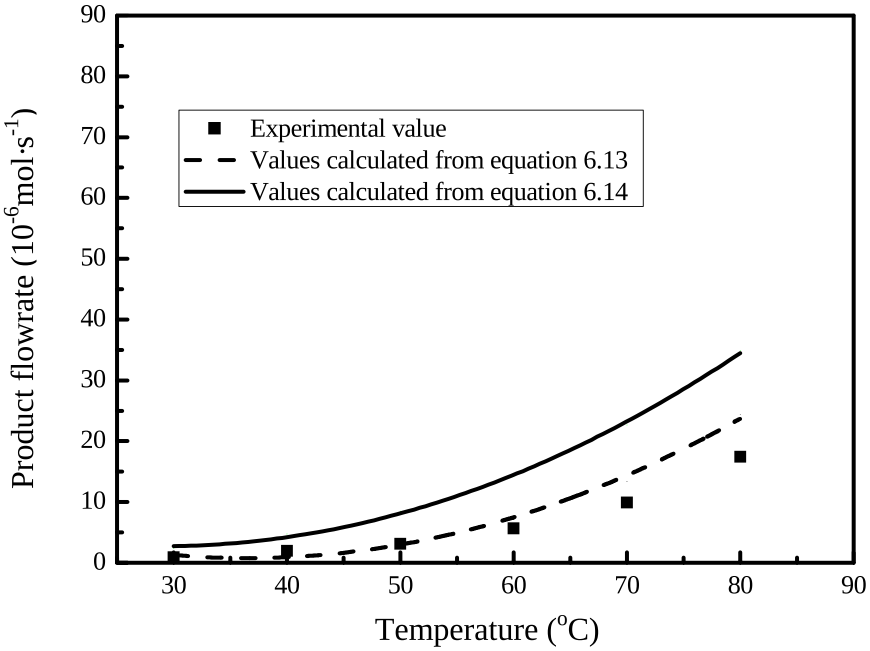

Figure 6.16 Permeate product flowrate for distillation with pure water using membrane 3. Feed flowrate: 0.60 L/min.

6.3.2 Desalination experiments

In order to obtain a clear understanding on how to improve the performance of VMD for water desalination, the effects of feed NaCl concentration and flowrate on the permeation flux were evaluated.

6.3.2.1 Effect of NaCl concentration on VMD performance

Water can be categorized according to its salinity level. There are four main categories of salinity: brine water (which has total dissolved solids concentration of about 5 wt% or more), saline water (with a salt concentration of 3 – 5 wt%), brackish water (with a salt concentration of 0.05 – 3 wt%) and fresh water with a salt concentration below 0.5 wt%. Different types of water have been discussed in details by El-Manharawy and Hafez [Ei-Manharawy and Hafez, 2001].

In order to investigate the effects of water salinity on VMD performance, experiments were conducted using two hollow fiber membranes (membrane 1 and membrane 3) with different membrane permeabilities. Figure 6.17 shows the relationship between the permeation flux and the feed concentration. The permeation flux decreased when the salt concentration in the feed increased. The trend is more obvious for membrane 1, which has a higher permeability. The decrease in the permeation flux can be attributed to concentration polarization, which leads to reduced water vapor pressure at the liquid/vapor interface.

The dependence of saturated water vapor pressure on the NaCl concentration in the feed can be evaluated from the thermodynamics of aqueous NaCl solutions. When the salt concentration increases, the activity coefficient of water decreases, and so does the saturated water vapor pressure above the solution. A thermodynamic model, which can be used to calculate the saturated vapor pressures of solutions at different operating conditions, has been proposed, which is in a good agreement with the experimental data [Mokbel et al., 1997]. This model is discussed in Appendix D. Once the water vapor pressure at the liquid/vapor interface is obtained, the permeation flux, taking into account the permeate pressure build-up, can be determined using the overall mass transfer coefficients in Figure 6.5. Figures 6.17 and 6.18 show that the calculated permeation flux is much higher than the experimental data for membrane 1, which has a higher permeability. For the membrane 3 with a lower permeability, the experimental data are close to the calculated values. This implied that the impact of concentration polarization on permeation flux is more significant for VMD with a high permeability membrane, and the concentration polarization is less important for VMD with a low permeability membrane because of the relatively high mass transfer resistance from the membrane. This also seems to suggest that there may be interaction effects on permeation flux between concentration and membrane permeability, which will be discussed in 6.3.3.

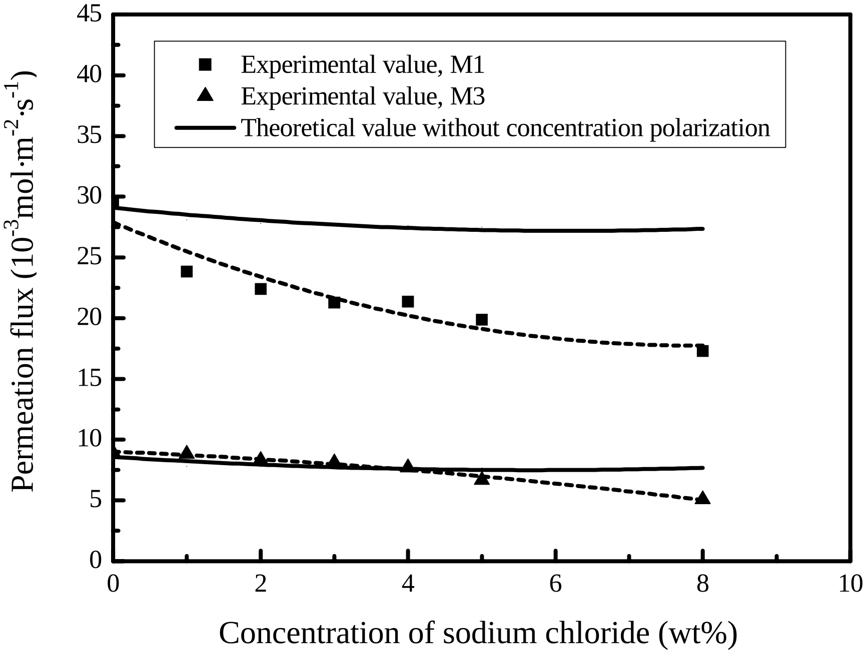

Figure 6.17 Permeation flux vs. the concentration of sodium chloride in the feed. Flowrate, 0.60 L/min; operating temperature, 80°C.

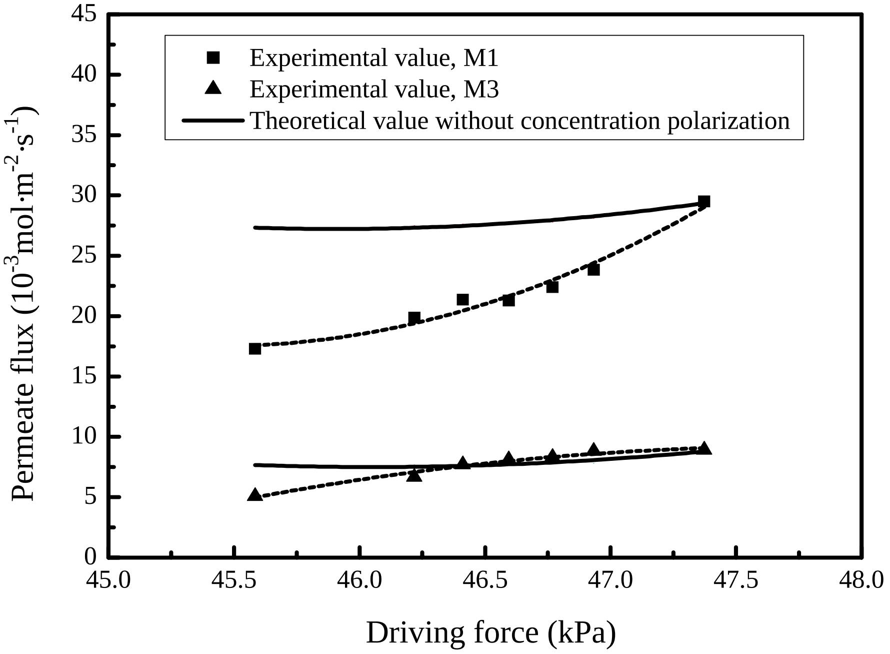

Figure 6.18 Permeation flux vs. driving force. Flowrate, 0.60 L/min; operating temperature, 80 °C.

6.3.2.2 Effect of feed flowrate VMD performance

The effect of feed flowrate on the VMD performance was conducted at different operating conditions: different feed solutions (pure water and 8 wt% NaCl solution) at two temperatures (30.0 and 80.0°C).

Figure 6.19 shows the permeation flux as a function of the feed flowrate. When pure water was used as the feed, no influence of feed flowrate was observed whatever the temperature was. The flux is re-plotted vs. Reynolds number (Re) for the different operating conditions in Figure 6.20. The Reynolds number ranges from 780 to 5200 when the flowrate operation varies from 0.2 to 0.60 L/min. Laminar flow is considered to occur when Re is less than 2000, and turbulent flow occurs when Re is higher than 4000. In the interval between Re 2000 and 4000, transition flows take place. The feed flowrate does not have any influence on the permeation flux of pure water in all three flow regimes, which implies that the heat transfer resistance or the temperature polarization is indeed negligible.

For 8 wt% NaCl in feed, the permeation flux at 80.0°C varies from 12.1×10^{-6} to 17.3×10^{-6} $mol\cdot m^{-2}\cdot s^{-1}$ with an increase in the feed flowrate from 0.1 and 0.6 L/min. When the fluid flow was in the laminar flow region, the permeation flux increased with the increase of the flowrate. This means the concentration polarization occurred in the feed side and an increase in feed flowrate reduced the thickness of the boundary layer, thereby increasing the mass transfer coefficient in the liquid phase. As a result, the permeation flux increases. When the flow becomes turbulent, the boundary layer resistance is minimized, and thus a further increase in the flowrate will not affect the permeation flux, which will remain constant (17.3×10^{-3} $mol\cdot m^{-2}\cdot s^{-1}$).

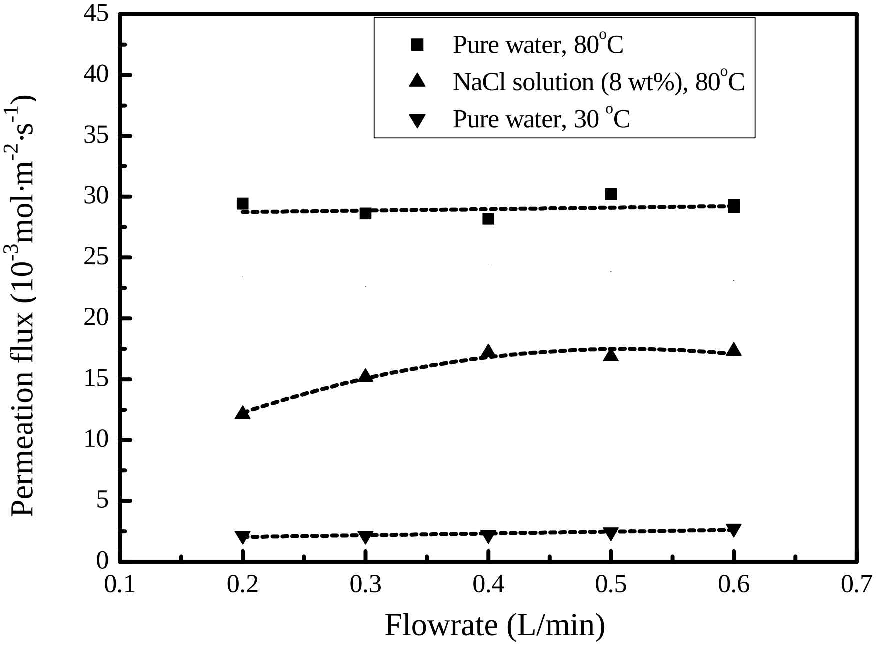

Figure 6.19 Effect of feed flowrate on permeation flux.

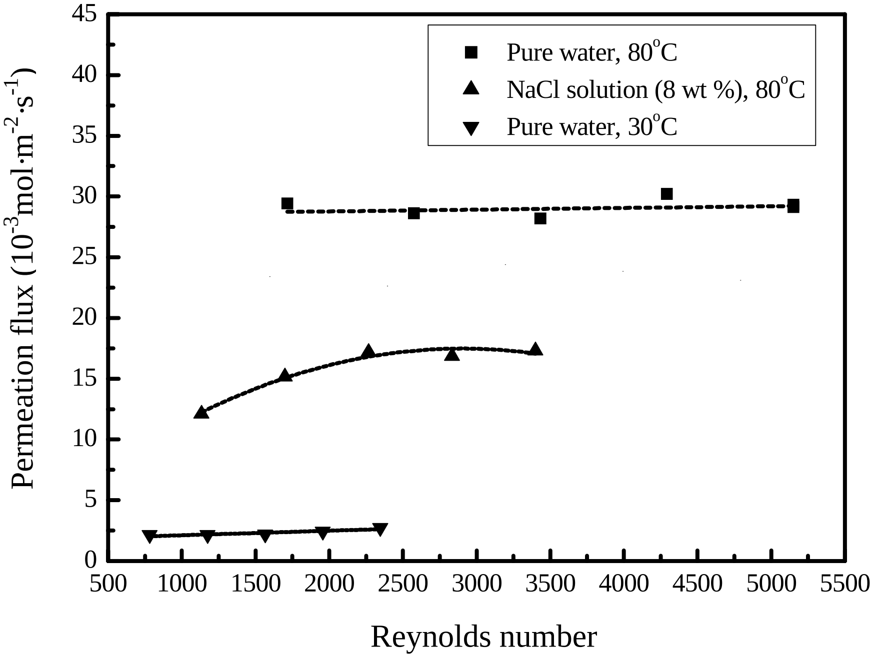

Figure 6.20 Permeation flux plotted as a function of Reynolds number.

6.3.3 Effects of interactions of operating parameters on VMD performance

The above results about effects of membrane permeability, temperature, feed NaCl concentration and flowrate on the permeation flux reveal that the effect of one factor on a response depended upon the level of other factors. There may be interactions among the main factors. For example, the effect of concentration polarization on the permeation flux was more significant for a membrane with a high permeability. While a high permeability favors water permeation, the concentration polarization will affect water permeation negatively. Hence, it was necessary to investigate the effects of the interactions on the permeation flux.

The overall mass transfer resistance is the sum of the liquid phase resistance phase and the resistance across the membrane. The feed flowrate and the feed concentration are two crucial factors that can influence mass transfer resistance within the liquid phase. When concentration polarization exists in the liquid phase, the mass transfer resistance through the boundary layers will also influence the performance of VMD. This can be shown by the following equation based on the film theory [Lawson and Lloyd, 1996]

$$N = K_f C_f \ln(\frac{x_i}{x_b}) \tag{6.15}$$

where C_f is the bulk concentration in the feed, and the x_b is the mole fraction of NaCl in the bulk feed, x_i is the mole fraction of NaCl at the interface.

K_f and $(K_m \cdot M_{H_2O}^{-0.5})$ are dimensionally different, which makes it difficult to evaluate the overall mass transfer coefficient. In order to evaluate the influence of the liquid phase on the mass transfer, based on Bandini and Sarti's work [1999], a more convenient method is used to analyze the contribution of the mass transfer resistance of the liquid phase. By replacing x_b *for* x_i to obtain a value of a driving force ΔP (T, x_b), a value of a mass transfer coefficient K_{ov} was calculated form equation 6.5. By comparing the values of K_{ov} and $(K_m \cdot M_{H_2O}^{-0.5})$, the contribution of membrane resistance to overall mass transfer resistance can be appreciated properly. If $K_{ov} = (K_m \cdot M_{H_2O}^{-0.5})$, the mass transfer within the liquid phase is negligible. If the $K_{ov} < (K_m \cdot M_{H_2O}^{-0.5})$, there is concentration polarization in liquid phase which offers additional resistance to mass transfer.

With a factorial design, the influence of membrane permeability and mass transfer in the liquid phase can be evaluated. The coded variables as well as their levels are shown in Table 6.3. The effects represented by single letters are the main effects and those represented by multi-letters are the interactions. These factors were varied at two levels: the codes "-" and "+" denote the "low" and the "high" levels, respectively. A 2^4 full factorial experimental design and the responses (permeation flux and the overall mass transfer coefficient) are presented in Table 6.4.

Table 6.3 Factors and levels.

Factor	Notation	Low (-1)	High (+1)
Membrane permeability	A	0.363 (M3)	0.988 (M1)
Flowrate (L/min)	B	0.20	0.60
Temperature (^oC)	C	30.0	80.0
NaCl concentration (wt %)	D	0.00	8.00

Unit of membrane permeability ($K_m / \sqrt{M_{H_2O}}$) (10^{-6} mol·m^{-2}·s^{-1}·Pa^{-1})

Table 6.4 Experiments of 2^4 full factorial design: set up and results.

Run	Treatment combination	Main effects				2 factor interactions						3 factor interactions				4 factor interaction	Permeation flux (mol·m^{-2}·s^{-1})	Overall mass transfer coefficient (mol·m^{-2}·s^{-1}·Pa^{-1})
		A	B	C	D	AB	AC	AD	BC	BD	CD	ABC	ABD	ACD	BCD	ABCD		
1	-1	-	-	-	-	+	+	+	+	+	+	-	-	-	-	+	4.31E-04	1.36E-07
2	A	+	-	-	-	-	-	-	+	+	+	+	+	+	-	-	2.15E-03	6.79E-07
3	B	-	+	-	-	-	+	+	-	-	+	+	+	-	+	-	4.33E-04	1.37E-07
4	C	-	-	+	-	+	-	+	-	+	-	+	-	+	+	-	8.30E-03	1.79E-07
5	D	-	-	-	+	+	+	-	+	-	-	-	+	+	+	-	4.51E-04	1.84E-07
6	AB	+	+	-	-	+	-	-	-	-	+	-	-	+	+	+	2.73E-03	8.62E-07
7	AC	+	-	+	-	-	+	-	-	+	-	-	+	-	+	+	2.94E-02	6.35E-07
8	AD	+	-	-	+	-	-	+	+	-	-	+	-	-	+	+	1.18E-03	4.82E-07
9	BC	-	+	+	-	-	-	+	+	-	-	-	+	+	-	+	8.37E-03	1.81E-07
10	BD	-	+	-	+	-	+	-	-	+	-	+	-	+	-	+	4.75E-04	1.94E-07
11	CD	-	-	+	+	+	-	-	-	-	+	+	+	-	-	+	4.18E-03	1.09E-07
12	ABC	+	+	+	-	+	+	-	+	-	-	+	-	-	-	-	2.93E-02	6.33E-07
13	ABD	+	+	-	+	+	-	+	-	+	-	-	+	-	-	-	1.58E-03	6.44E-07
14	ACD	+	-	+	+	-	+	+	-	-	+	-	-	+	-	-	1.21E-02	3.15E-07
15	BCD	-	+	+	+	-	-	-	+	+	+	-	-	-	+	-	4.75E-03	1.24E-07
16	ABCD	+	+	+	+	+	+	+	+	+	+	+	+	+	+	+	1.73E-02	4.52E-07

The identification of significant effects on permeation flux and overall mass transfer coefficient was performed using normal probability plots, which are a graphical technique based on the ‘‘Central limit theorem’’. If an effect has a large deviation from the normal distribution which describes a straight line, it indicates that the corresponding factor or interaction had significant influence on the response in the designed experiment [Lundstedt et al., 1998]. The results that were used to construct the normal probability plot are given in Tables 6.5 and 6.6. By examining the normal probability plot in Figures 6.21 and 6.22, the following observations can be made:

In general, the main effects A, C, D and to a lesser extent, their interactions AC, CD, AD, ACD, had significant effects on the permeation flux. A, B, D and AD were significant for the overall mass transfer coefficient.

The main effects of A (membrane permeability) and the interactions involving A had significant effects on the permeation flux. This indicates the membrane transfer resistance played a dominant role in the mass transfer, which is also demonstrated by the results in Figure 6.22. Hence, it is obvious that the performance of VMD can be enhanced by using proper membranes.

The main effects of C (temperature) had significant effect on permeation flux but it is not significant for the overall mass transfer coefficient. Increasing temperature will increase the saturated vapor pressure significantly, which results in an enhancement in the driving force for permeation. Although equation 6.4 indicates that the mass transfer coefficient might slightly depend on the temperature, Figure 6.22 illustrates that the temperature dependence of mass transfer coefficient is not significant.

Besides the main effect A, the main effects B (feed flowrate) and D (feed NaCl concentration) were also significant factors for the overall mass transfer coefficient. This implies that the liquid phase mass transfer resistance was not negligible. The reason for this is that: the concentration polarization takes place, and it not only offers a mass transfer resistance in the liquid phase but also reduced the saturated vapor pressure at the liquid/vapor interface due to increased NaCl concentration [Fawzi and Simandl, 1994; Mokbel et al., 1997].

The main effects and interactions that are close to the central straight line are relatively less significant compared to the other effects. However, it must be clarified that the insignificance of an effect does not necessarily mean that this particular factor is unimportant; it just implies that this factor has little influence on the response when this factor is varied over the operating range of exploration, compared to the other factors. For example, as shown in the Figure 6.21, B is identified as less important to the permeation flux. However, Figure 6.22 shows the feed flowrate did have an influence on the overall mass transfer coefficient, which means that it can enhance the VMD performance.

The interactions exist among A, C and D. The performance of VMD is determined by the overall mass transfer coefficient and the driving force. A high productivity can be obtained by either increasing overall mass transfer coefficient or increasing the driving force, or both. However, the performance of one factor depends upon the level of other factors. For example, the productivity of water can be increased more significantly by increasing the operating temperature when a membrane has a higher permeability. The overall mass transfer resistance consists of mass transfer resistances of the membrane and the liquid boundary layer, and therefore, the significance of either of the two resistances depends on the level of the other. This is consistent with the research findings in pervaporation that the significance of the effect of concentration polarization on separation depends on the relative resistances of the membrane and the boundary layer [Feng and Huang, 1994].

Table 6.5 Calculation for normal probability plot: effects on permeation flux.

Factor	Estimated effects(E)	Rank Order (i)	Probability(P_i) =(i-0.5)/15	Cumulative standard normal distribution
D	-4.90E-03	1	0.0333	-1.8343
CD	-4.39E-03	2	0.1000	-1.2817
AD	-2.98E-03	3	0.1667	-0.9672
ACD	-2.44E-03	4	0.2333	-0.7281
ABC	4.45E-04	5	0.3000	-0.5244
ABD	5.80E-04	6	0.3667	-0.3405
BC	6.00E-04	7	0.4333	-0.1679
ABCD	6.31E-04	8	0.5000	0
AB	6.82E-04	9	0.5667	0.1679
BD	7.12E-04	10	0.6333	0.3405
BCD	7.51E-04	11	0.7000	0.5244
B	8.51E-04	12	0.7667	0.7281
AC	7.08E-03	13	0.8333	0.9672
A	8.55E-03	14	0.9000	1.2817
C	1.30E-02	15	0.9667	1.8343

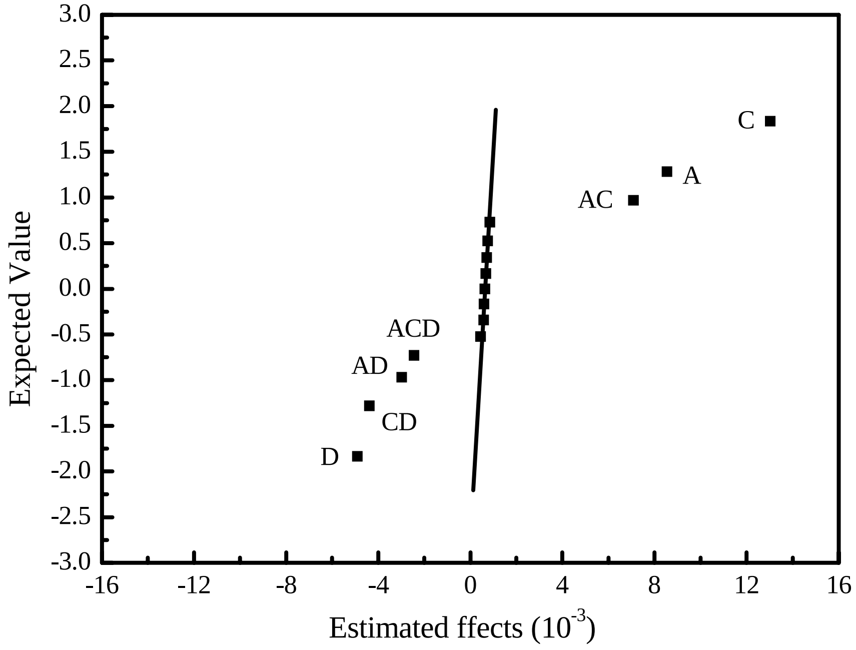

Figure 6.21 Normal probability plot: effects on permeation flux.

Table 6.6 Calculation for normal probability plot: effects on K_{ov}.

Factor	Estimated effects(E)	Rank Order (i)	Probability(P_i) =(i-0.5)/15	Cumulative standard normal distribution
D	-1.81E-07	1	0.0333	-1.8343
AD	-1.45E-07	2	0.1000	-1.2817
C	-6.53E-08	3	0.1667	-0.9672
AC	-6.22E-08	4	0.2333	-0.7281
ABC	-2.53E-08	5	0.3000	-0.5244
BC	-2.39E-08	6	0.3667	-0.3405
CD	-1.90E-08	7	0.4333	-0.1679
ABD	5.03E-09	8	0.5000	0
BD	9.56E-09	9	0.5667	0.1679
ABCD	2.11E-08	10	0.6333	0.3405
BCD	2.20E-08	11	0.7000	0.5244
ACD	2.76E-08	12	0.7667	0.7281
AB	4.96E-08	13	0.8333	0.9672
B	5.52E-08	14	0.9000	1.2817
A	4.00E-07	15	0.9667	1.8343

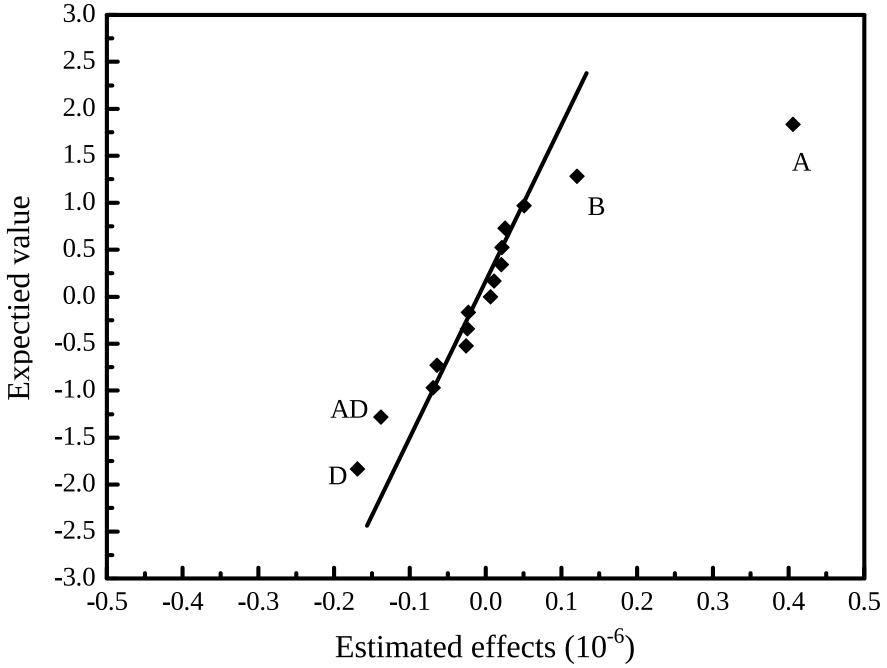

Figure 6.22 Normal probability plot: effects on K_{ov}.

6.4 Conclusions

In order to obtain a understanding of the VMD for water desalination, experiments were carried out to evaluate the effects of the operating conditions, and the significance analysis of parameter interactions was also performed by factorial design. It was found:

1) The membrane played a dominant role in the mass transfer process and the significance of the liquid phase resistance depended on the membrane permeability.

2) The concentration polarization in the boundary layer could occur, depending on the hydrodynamic conditions, which affected by the feed concentration and flowrate. At a given feed concentration, an increase in the feed flowrate would increase the water permeation rate in VMD.

3) An increase in temperature would increase the driving force for permeation, leading to an increase in the water permeation flux.

4) The permeate pressure build up was analyzed and the significance of the pressure build-up on VMD was illustrated. The higher the permeation flowrate, the more significant the permeate pressure build-up.

Chapter 7

Conclusions and recommendations

7.1 General conclusions and contributions to original research

7.1.1 Thermodynamics and kinetics pertinent to the formation of microporous PVDF membranes

Specialty PVDF materials (Kynar 741, 761, 461, 2851, and RC-10186) developed by Arkema were examined from a thermodynamic and kinetic point of view. The polymer structure did have an influence on the thermodynamic stability of the polymer solution system. The effects of additives on the thermodynamic stability of the polymer solutions depended on the specific polymer as well. The use of LiCl additive could improve the water tolerance of Kynar 461, 2851 and RC 10186, but there was no significant impact on the thermodynamic stability of Kynar 761 and 741 solution systems.

Solvent evaporation in the early stage could be described quantitatively. The different grades of PVDF materials did not seem to affect the solvent evaporation. The solvent evaporation rate depended on temperature and the film-casting thickness: solvent evaporated faster from a thinner membrane at a higher temperature.

The mass-transfer during the polymer precipitation was diffusion controlled. A mathematical model could be used to assess the solvent-nonsolvent exchange rate and LiCl leaching rate. By adjusting the solvent evaporation and polymer precipitation conditions, the permeability and selectivity of the microporous membranes could be finely tuned.

7.1.2 Fabrication of PVDF hollow fiber membranes

Polymers that can be cast into flat membranes may not be suitable for hollow fiber membrane fabrication. In order to examine the properties of the newly developed specialty PVDF as hollow fiber membrane materials, Kynar 741, 761, 2851 and RC10214 were used to fabricate hollow fiber membranes. It was found that Kynar 741 and 2851 were most suitable for fabricating hollow fiber membranes.

The effects of parameters involved in the procedure of fiber spinning on the dimensions and properties of the fiber membranes were investigated. The porous structure of the membranes was characterized by the gas permeation method, gas-liquid displacement method and scanning electron microscope. The membranes exhibit a macrovoid structure near the surface, and a sponge-like structure in the middle of the walls.

7.1.3 Improving the hydrophilicity of PVDF membranes by amine treatment

Amine-treatment improved the hydrophilicity of the resulting PVDF membranes. The effects of MEA concentration, treatment time, treatment temperature and the interactions among these factors were evaluated. Defluorination occurred in the amine treatment of PVDF membranes. The existence of conjugated C=C and C=O after amine treatment were confirmed by FT-IR and EDAX element analysis. The improvement in the membrane hydrophilicity was demonstrated by contact angle studies with non-porous PVDF membranes. However, excessive amine treatment could damage the macrovoids in the microporous membrane.

7.1.4 Vacuum membrane distillation with PVDF hollow fibers

Membranes played a dominant role in the mass transfer process, and the significance of the liquid phase resistance depended on the magnitude of the membrane permeability. An increase in temperature could increase the water productivity remarkably. The negative effects of concentration polarization on VMD could be reduced by increasing the feed flowrate. The permeate pressure build-up in the hollow fiber bores was investigated by experiments and parametric analysis. It was revealed that the water productivity would be overestimated if the pressure build-up was not taken into account.

7.2 Recommendations for future work

Based on the research findings from this work, the following are recommended for further studies in future.

1) An empirical equation (equation 3.4) was used to evaluate solvent evaporation quantitatively. Castellari and Ottani [1981] proposed that the mass transfer within the cast film during the solvent evaporation was a combination of solvent diffusion and polymer contraction. The mutual diffusion coefficient for a solvent-polymer system depends on temperature and molecular weight [Resi et al., 2005]. The applicability of the empirical equation 3.4 for different polymers (PVDF, PEI, PSF) and solvents (NMP, DMAc, DMF, DMSO) should be investigated.

2) It was also found that the solvent-nonsolvent exchange followed a linear relationship with respect to the square root of time at the early stage of polymer precipitation. A further mathematical simulation based on equation 3.5 may be helpful for better understanding of the kinetics of membrane formation based on established mass transfer and diffusion theories [Reis et al., 2005].

3) While the amine treatment of PVDF membranes improved surface hydrophilicity, the membrane structure will collapse if the treatment conditions are not properly controlled. Investigations on chemical compositions of suitable amine solutions, which will be applied in surface modification of PVDF membranes, should be performed.

4) Besides water desalination by VMD, the removal of organic component from aqueous solutions is another potential application of VMD. As there are more than one permeating species involved (i.e., water and volatile organic compounds), the effects of pressure build-up in fiber bores on the VMD will be more complicated than in the desalination process. Therefore, it is necessary to investigate the gas pressure build-up when VMD is used to remove the volatile organic component from solutions. In addition, the use of smaller fibers can increase membrane area packing density in hollow fiber

modules. However, the pressure build-up in the fiber bores will be more significant, which affect the process performance negatively. It is thus of interest to optimize the fiber dimensions in order to maximize the membrane productivity.

References

Altena, F. W., J. Smid, J. W. A. Van den berg, J. G. Wijimans and C. A. Smolders, Diffusion of solvent from a cast cellulose acetate solution during the formation of skinned membranes, Polymer, 26 (1985) 1531-1538.

Altinkaya, S. A. and B. Ozbas, Modeling of asymmetric membrane formation by dry-casting method, J. Membr. Sci., 230 (2004) 71-89.

Anderson, J. E. and R. Ullman, Mathematical analysis of factors influencing the skin thickness of asymmetric reverse osmosis membrane, J. Appl. Polym. Sci., 44 (1973) 4303-4311.

Aptel, P., N. Abidine, F. Ivaldi and J. P. Lafaille, Polysulfone hollow fibers-effect of spinning conditions on ultrafiltration properties, J. Membr. Sci., 22 (1985) 199-215.

Atkinson, S., A brief history of membrane science, Filtr. and Sep., 36 (1999) 28.

Baker, R. W., Membrane Technology and Applications, 2nd ed., Wiley, West Sussex, 2004.

Bakunov, V. A. and L. F. Maiboroda, Ultrafiltration equipment hollow fibers and areas of application, Fibre Chem., 33 (2001) 145-149.

Banat, A. F. and J. Simandl, Theoretical and experimental study in membrane distillation, Desalination, 95 (1994) 39-52.

Banat, A. F. and J. Simandl, Removal of benzene traces from contaminated water by vacuum membrane distillation, Chem. Eng. Sci., 51 (1996) 1257-1265.

Bandini, S., C. Gostoh and G. C. Sarti, Separation efficiency in vacuum membrane distillation, J. Membr. Sci., 73 (1992) 217-229.

Bandini, S., A. Saavedra and G. C. Sarti, Vacuum membrane distillation: experiments and modeling, AIChE J., 43 (1997) 398-408.

Bandini, S. and G. C. Sarti, Heat and mass transport resistances in vacuum membrane distillation per drop, AIChE J., 45 (1999) 1422-1433.

Barth, C., M. C. Goncalves, A. T. N. Pires, J. Roeder and B. A. Wolf, Asymmetric polysulfone and polyethersulfone membranes: effects of thermodynamic conditions during formation on their performance, J. Membr. Sci., 169 (2000) 287-299.

Boenig, H. V., Structure and Properties of Polymers, Wiley, New York, 1973.

Bottino, A., G. Capannelli, S. Munari and A. Turturro, Solubility parameters of poly(vinylidene fluoride), J. Polym. Sci., Part B: Polym. Phys., 26 (1988) 785-794.

Bottino, A., G. Capannelli, O. Monticelli and P. Piaggio, Poly(vinylidene fluoride) with improved functionalization for membrane production, J. Membr. Sci., 166 (2000) 23-29.

Bradley, D. J. and K. S. Pitzer, Thermodynamics of electrolytes. 12. Dielectric properties of water and Debye-Hueckel parameters to 350°C and 1kbar, J. Phys. Chem., 83 (1979) 1599-1603.

Brewis, D. M., I. Mathieson, I. Sutherland, R. A. Cayless and R. H. Dahm, Pretreatment of poly(vinyl fluoride) and poly(vinylidene fluoride) with potassium hydroxide, Int. J. Adhes. Adhes., 16 (1996) 87-95.

Bruggen, B. V. and C. Vandecasteele, Distillation vs. membrane filtration: overview of process evolutions in seawater desalination, Desalination, 143 (2002) 207-218.

Bruggen, B. V., Desalination by distillation and by reverse osmosis–trends towards the future, Membr. Technol., (2003) 6-9.

Cabasso, I., E. Klein and J. K. Smith, Polysulfone hollow fibers. I. Spinning and properties, J. Appl. Polym. Sci., 20 (1976) 2377-2394.

Cabassud, C. and D. Wirth, Membrane distillation for water desalination: how to chose an appropriate membrane, Desalination, 157 (2003) 307-314.

Cardona, E., S. Culotta and A. Piacentino, Energy saving with MSF-RO series desalination plants, Desalination, 153 (2002) 167-171.

Castellari, C. and S. Ottani, Preparation of reverse osmosis membranes. A numerical analysis of asymmetric membrane formation by solvent evaporation from cellulose acetate casting solutions, J. Membr. Sci., 9 (1981) 29-41.

Chabot, S., C. Roy, G. Chowdhury and T. Matsuura, Development of poly(vinylidene fluoride) hollow fiber membranes for treatment of water/organic vapor mixtures, J. Appl. Polym. Sci., 65 (1997) 1263-1270.

Cheng, L., D. Lin, C. Shin, A. Dwan and C. C. Gryte, PVDF membrane formation by diffusion-induced phase separation morphology prediction based on phase behavior and mass transfer modeling, J. Polym. Sci., Part B: Polym. Phys., 37 (1999) 2079-2092.

Cheng, J., D. Wang, F. Lin and J. Lai, Formation and gas flux of asymmetric PMMA membranes, J. Membr. Sci., 109 (1996) 93-107.

Cheng, L., T. Young, W. Chuang, L. Chen and L. Chen, The formation mechanism of membranes prepared from the nonsolvent-solvent-crystalline polymer systems, Polymer, 42 (2001) 443-451.

Cheryan, M., Ultrafiltration and Microfiltration Handbook, Technomic Publishing, Lancaster, 1998.

Childress, A. E., P. L. Clech, J. L. Daugherty, C. Chen and G. L. Leslie, Mechanical analysis of hollow fiber membrane integrity in water reuse applications, Desalination, 80 (2005) 5-14.

Cho, J. W. and H. Y. Song, Dehydrofluorination of a copolymer of vinylidene fluoride and tetrafluoroethylene by phase transfer catalysis reaction, J. Polymer Sci., Part A: Polym. Chem., 33 (1995) 2109-2112.

Chou, W. L. and M. C. Yang, Effect of take-up speed on physical properties and permeation performance of cellulose acetate hollow fibers, J. Membr. Sci., 250 (2005) 259-267.

Chung, T. S., J. Qin and J. Gu, Effect of shear rate within the spinneret on morphology, separation performance and mechanical properties of ultrafiltration polyethersulfone hollow fiber membranes, Chem. Eng. Sci., 55 (2000) 1077-1091.

Cohen, C., G. B. Tanny and S. Prager, Diffusion-controlled formation of porous structures in ternary polymer systems, J. of Polym. Sci. Polymer Phys. Ed., 17 (1979) 477-489.

Comerton, A. M., R. C. Andrews and D. M. Bagley, The influence of natural organic matter and cations on fouled nanofiltration membrane effective molecular weight cut-off, J. Membr. Sci., 327 (2009) 155-163.

Couffin, N., C. Cabassud and V. Lahoussine-Turcaud, A new process to remove halogenated VOCs for drinking water production: vacuum membrane distillation, Desalination, 117 (1998) 233-245.

Crowe, R. and J. P. S. Badyal, Surface modification of poly(vinylidene difluoride) (PVDF) by LiOH, J. Chem. Soc., Chem. Commun., (1991) 958-959.

Cuperus, F. P. and C. A. Smolders, Characterization of UF membranes: membrane characteristics and characterization techniques, Adv. Colloid Interface Sci., 34 (1991) 135-173.

Deanin, R. D., Polymer Structure, Properties and Applications, Cahners Books, Boston, 1972.

Demshmukh, S. P. and K. Li, Effect of ethanol composition in water coagulation bath on morphology of PVDF hollow fiber membranes, J. Membr. Sci., 150 (1998) 75-85.

Dias, A. J. and T. J. McCarthy, Dehydrofluorination of poly(vinylidene fluoride) in dimethylformamide solution: synthesis of an operationally soluble semiconducting polymer, J. Polym. Sci., Part A: Polym. Chem., 23 (1985) 1057-1061.

Ei-Manharawy, S. and A. Hafez, Water type and guidelines for RO system design, Desalination, 139 (2001) 97-113.

El-Bourawi, M. S., Z. Ding, R. Ma and M. Khayet, A framework for better understanding membrane distillation separation process, J. Membr. Sci., 285 (2006) 4-29.

Ellis, B., Chemistry and Technology of Epoxy Resins, Blackie Academic and Prefessional, London, 1993.

Feng, C., R. Wang, B. Shi, G. Li and Y. Wu, Factors affecting pore structure and performance of poly(vinylidene fluoride-co-hexafluoro propylene) asymmetric porous membrane, J. Membr. Sci., 277 (2006) 55-64.

Feng, X. and R. Y. M. Huang, Concentration polarization in pervaporation separation processes, J. Membr. Sci., 92 (1994) 20 l-208.

Franken, A. C. M., J. A. M. Nolten, M. H. V. Mulder, D. Bargeman and C. A. Smolders, Wetting criteria for the applicability of membrane distillation, J. Membr. Sci., 33 (1987) 315-328.

Hahn, B. and V. Percec, Functional polymers and sequential copolymers by phase transfer catalysis. Vinylidene fluoride–trifluoroethylene copolymers by surface modification of polyvinylidene fluoride, J. Polym. Sci., Part A: Polym. Chem., 25 (1987) 783-804.

Hanemaaijer, J. H., J. V. Medevoort, A. E. Jansen, C. Dotremont, E. V. Sonsbeek, T. Yuan and L. D. Ryck, Memstill membrane distillation–a future desalination technology, Desalination, 199 (2006) 175-176.

Hao, J. and S. Wang, Studies on membrane formation mechanism by the light transmission technique. I, J. Appl. Polym. Sci., 87 (2003) 174-181.

Hernández, A., J. I. Calvo, P. Prádanos and F. Tejerina, Pore size distributions in microporous membranes. A critical analysis of the bubble point extended method, J. Membr. Sci., 112 (1996) 1-12.

Hester, J. F. and A. M. Mayes, Design and performance of foul-resistant poly(vinylidene fluoride) membrane prepared in a single-step by surface segregation, J. Membr. Sci., 202 (2002) 119-135.

Ho, W. S. W. and K. K. Sirkar, Membrane Handbook, 1st ed., Van Nostrand Reinhold, New York, 1992.

Huang, R. Y. M. and X. Feng, Studies on solvent evaporation and polymer precipitation pertinent to the formation of asymmetric polyetherimide membranes, J. Appl. Polym. Sci., 57 (1995) 613-621.

Idris, A., M. Y. Noordin, A. F. Ismail and S. J. Shilton, Study of shear rate influence on the performance of cellulose acetate reverse osmosis hollow fiber membranes, J. Membr. Sci., 202 (2002) 205-215.

Imdakm, A. O. and T. Matsuura, A Monte Carlo simulation model for membrane distillation processes: direct contact (MD), J. Membr. Sci., 237 (2004) 51-59.

Ismail, A. F., I. R. Dunkin, S. L. Gallivan and S. J. Shilton, Production of super selective polysulfone hollow fiber membranes for gas separation, Polymer, 40 (1999) 6499-6506.

Ismail, A. F. and L. P. Yean, Review on the development of defect-free and ultrathin-skinned asymmetric membranes for gas separation through manipulation of phase inversion and rheological factors, J. Appl. Polym. Sci., 88 (2003) 442-451.

Ismail, A. F. and S.N. Kumari, Potential effect of potting resin on the performance of hollow fibre membrane modules in a CO_2/CH_4 gas separation system, J. Membr. Sci., 236 (2004) 183-191.

Ismail, A. F., M. I. Mustaffar, R. M. Illis and M. S. Abdullah, Effect of dope extrusion rate on morphology and performance of hollow fibers membrane ultrafiltration, Sep. Sci. Technol., 49 (2006) 10-19.

Izquierdo-Gil, M. A. and G. Jonsson, Factors affecting flux and ethanol separation performance in vacuum membrane distillation (VMD), J. Membr. Sci., 214 (2003) 113-130.

Kesting, R. E., Synthetic Polymeric Membranes, McGraw-Hill, New York, 1971.

Kesting, R. E., Synthetic Polymeric Membranes: A Structural Perspective, Wiley, New York, 1985.

Khayet, M., C. Y. Feng, K. C. Klulbe and T. Matsuura, Preparation and characterization of polyvinylidene fluoride hollow fiber membranes for ultrafiltration, Polymer, 43 (2002) 3879-3890.

Khayet, M., The effects of air gap length on the internal and external morphology of hollow fiber membranes, Chem. Eng. Sci., 58 (2003) 3091-3104.

Khayet, M., K. C. Khulbe and T. Matsuura, Characterization of membranes for membrane distillation by atomic force microscopy and estimation of their water vapor transfer coefficients in vacuum membrane distillation process, J. Membr. Sci., 238 (2004) 199-211.

Kise, H. and H. Ogata, Phase transfer catalysis in dehydrofluorination of poly(vinylidene fluoride) by aqueous sodium hydroxide solutions, J. Polym. Sci., Part A: Polym. Chem., 21 (1983) 3443-3451.

Kim, Y., J. Kim, H. Lee and S. Kim, A new modeling of asymmetric membrane formation in rapid mass transfer system, J. Membr. Sci., 190 (2001) 69-77.

Kim, H., R. K. Tyaci, A. E. Fouda and K. Jonasson, The kinetic study for asymmetric membrane formation via phase inversion process, J. Appl. Polym. Sci., 62 (1996) 621-629.

Koros, W. J. and G. K. Fleming, Membrane-based gas separation, J. Membr. Sci., 83 (1993) 1-39.

Kong, J. and K. Li, Preparation of PVDF hollow-fiber membrane via immersion precipitation, J. Appl. Polym. Sci., 81 (2001) 1643-1653.

Krantz, W. B., R. J. Ray. R. L. Sani and K. J. Gleason, Theoretical study of the transport processes occurring during the evaporation step in asymmetric membrane casting, J. Membr. Sci., 29 (1986) 11-36.

Kroschwitz, J. I. and M. Howe-Grant, Kirk-Othmer Encyclopedia of Chemical Technology, 4th ed., Wiley, New York, 1991.

Kunst, B. and S. Sourirajan, Evapoation rate and equilibrium phase separation data in relation to casting conditions and performance of porous cellulose acetate reverse osmosis membranes, J. Appl. Polym. Sci., 14 (1970) 1983-1996.

Kushida, A., Y. Masayuki, K. Akihiko and O. Teruo, Two-dimensional manipulation of differentiated Madin–Darby canine kidney (MDCK) cell sheets: The noninvasive harvest from temperature-responsive culture dishes and transfer to other surfaces, J. Biomed. Mater. Res., 154 (2001) 37-46.

Lai, J., F. Lin, T. Wu and D. Wang, On the formation of macrovoids in PMMA membranes, J. Membr. Sci., 155 (1999) 31-43.

Lawson, K. W. and D. R. Lloyd, Membrane distillation. I. Module design and performance evaluation using vacuum membrane distillation, J. Membr. Sci., 120 (1996) 111-121.

Lawson, K. W. and D. R. Lloyd, Review: Membrane distillation, J. Membr. Sci., 124 (1997) 1-25.

Lee, H. J., J. Won, H. Lee, Y. S. Kang, Solution properties of poly(amic acid)–NMP containing LiCl and their effects on membrane morphologies, J. Membr. Sci., 196 (2002) 267–277.

Lee, Y., J. Jeong, I. J. Toun and W. H. Lee, Modified liquid displacement method for determination of pore size distribution in porous membranes, J. Membr. Sci., 130 (1997) 149-156.

Leiknes, T., The effect of coupling coagulation and flocculation with membrane filtration in water treatment: A review, J. Environ. Sci., 21 (2009) 8-12.

Li, B. and K. K. Sirkar, Novel membrane and device for vacuum membrane distillation based desalination process, J. Membr. Sci., 257 (2005) 60-75.

Li, J. and B. Chen, Review of CO_2 absorption using chemical solvents in hollow fiber membrane contactors, Sep. Sci. Technol., 41 (2005) 109-112.

Li, Z. and C. Jiang, Investigation of the dynamics of poly(ether sulfone) membrane formation by immersion precipitation, J. Polym. Sci., Part B: Polym. Phys., 43 (2005) 498-510.

Lim, S. P., X. Tan and K. Li, Gas/vapor separation using membranes: Effect of pressure drop in lumen of hollow fibers, Chem. Eng. Sci., 55 (2000) 2641-2652.

Liu, F., B. K. Zhu and Y. Y. Xu, Improving the hydrophilicity of poly(vinylidene fluoride) porous membrane by electron beam initiated surface grafting of AA/SSS binary monomers, Appl. Surf. Sci., 253 (2006) 2096-2101.

Liu, Y. J., Separation of Volatile Organic Compounds from Nitrogen by Hollow Fiber Composite Membranes, MASc Thesis, University of Waterloo, Ontario, 2003.

Lundstedt, T., E. Seifert, L. Abramo, Bernt Thelin, A. Nystrom, J. Pettersen and R. Bergman, Experimental design and optimization, Chemom. Intell. Lab. Syst., 42 (1998) 3-40.

Lüdtkea, K., K. V. Peinemanna, V. Kascheb, and R. D. Behlinga, Nitrate removal of drinking water by means of catalytically active membranes, J. Membr. Sci., 151 (1998) 3-11.

Machado, P. S. T., A. C. Habert and C. P. Borges, Membrane formation mechanism based on precipitation kinetics and membrane morphology: flat and hollow fiber polysulfone membranes, J. Membr. Sci., 155 (1999) 171-183.

Mahajani, V. V. and J. B. Joshi, Kinetics of reactions between carbon dioxide and alkanolamines, Gas Sep. Purif., 2 (1988) 50-64.

Malaisamy, R., D. R. Mohan and M. Rajendran, Polyurethane and sulfonated polysulfone blend ultrafiltration membranes: I. Preparation and characterization studies, J. Colloid Interface Sci., 254 (2002) 129-140.

Malcolm, P. S., Polymer Chemistry: An Introduction, 3rd ed., Oxford University Press, New York, 1999.

Marek, R. and J. Straub, Analysis of the evaporation coefficient and the condensation coefficient of water, Int. J. Heat Mass Transfer., 44 (2001) 39-53.

Márquez-Rocha, F. J., M. Aguilar-Juárez, M. J. Acosta-Ruíz and M. I. Gradilla, Rapid characterization of ultrafiltration membranes by scanning electron microscopy, Russ. Chem. Bull. (Int. Ed.), 50 (2001) 1320-1322.

Martinez, L. F., J. Florido-Diaz, A. Hernandez and P. Pradanos, Characterization of three hydrophobic porous membranes used in membrane distillation: Modeling and evaluation of their water vapor permeabilities, J. Membr. Sci., 203 (2002) 15-27.

Mason, R. L., R. F. Gunst and J. L. Hess, Statistical Design and Analysis of Experiments: with Applications to Engineering and Science, 2nd ed., Wiley, Hoboken, 2003.

Matsuyama, H., M. Nishiguchi and Y. Kitamura, Phase separation mechanism during membrane formation by dry-cast process, J. Appl. Polym. Sci., 77 (2000) 776-782.

McGuire, K. S., K. W. Lawson and D. R. Lloyd, Pore size distribution determination from liquid permeation through microporous membranes, J. Membr. Sci., 99 (1995) 127-137.

Mokbel, I., S. Ye, J. Jose and P. Xans, Study of non ideality of various aqueous sodium chloride solutions by vapor pressures measurements and correlation of experimental results by Pitzer's method, J. Chem. Phys., 94 (1997) 122-137.

Mchugh, A. J. and C. S. Tsay, Dynamics of the phase inversion process, J. Appl. Polym. Sci., 48 (1992) 2011-2021.

Mulder, M., Basic Principles of Membrane Technology, Kluwer Academic, Dordrecht, 1991.

Mueller, J. and R. H. Davis, Protein fouling of surface-modified polymeric microfiltration membranes, J. Membr. Sci., 116 (1996) 47-60.

Nunes, S. P., Recent advances in the controlled formation of pores in membranes, Trends Polym. Sci., 5 (1997) 187-192.

Nunes, S. P. and T. Inoue, Evidence for spinodal decomposition and nucleation and growth mechanisms during membrane formation, J. Membr. Sci., 111 (1996) 93-103.

Nunes, S. P. and K. V. Peinemann, Ultrafiltration membranes from PVDF/PMMA blends, J. Membr. Sci., 73 (1992) 25-35.

Owen, E. D., M. Shah and M. V. Twigg, Phase transfer catalysed degradation of poly(vinyl chloride). I. Product characterisation and handling, Polym. Degrad. Stab., 51 (1996) 151-158.

Pacioreck, K. L., L. C. Mitchell and C. T. Leh'k, Mechanism of amine crosslinking of fluoroelastomers. I. Solution studies, J. Polym. Sci., (1960) 405-413.

Paciorek, K. L., B. A. Merkl and C. T. Lenk, Mechanims of amine crosslinking of fluoroelastomers. II. Model compound syntheses and studies, J. of Org. Chem., 27 (1962) 266-269.

Pan, C. Y., Gas separation by permeators with high flux asymmetric membranes, AIChE J., 29 (1983) 545-552.

Pandey, P. and R. S. Chauhan, Membranes for gas separation, Prog. Polym. Sci., 26 (2001) 853-893.

Parlay, M., Influence of chain structure on the crystallization mechanism of poly(vinylidenefluoride)/poly(methyacrylate) blends: evidence of chain extension due to blending, Polymer, 39 (1998) 413-421.

Pasquier, A. D., P. C. Warren, D. Culver, A. S. Gozdz and G. G. Amatucci, Plastic PVDF-HFP electrolyte laminates prepared by a phase-inversion process, Solid State Ionics, 135 (2000) 249.

Patsis, A. V., E. H. Henriques and H. L. Frisch, Interdiffusion in complex polymer systems used in the formation of microporous coatings, J. Polym. Sci., Part B: Polym. Phys., 28 (1990) 2681-2689.

Piątkiewicz, W., S. Rosiński, D. Lewińska, J. Bukowski and W. Judycki, Determination of pore size distribution in hollow fiber membranes, J. Membr. Sci., 153 (1999) 91-102.

Pilon, R., B. Kunst and S. Sourirajan, Studies on the development of improved reverse osmosis membranes from cellulose acetate-acetone formamide casting solutions, J. Appl. Polym. Sci., 15 (1971) 1317-1334.

Pitzer, K. S. and J. C. Pelper, Thermodynamic properties of aqueous sodium chloride solutions, J. Phys. Chem. Ref. Data, 13 (1984) 1-104.

Pnueli, D. and C. Gutfinger, Fluid Mechanics, Cambridge University Press, Cambridge, 1992.

Resi, R. A., R. Nobrega, J. V. Oliveira and F. W. Tavares, Self and mutual diffusion coefficient equation for pure fluids, liquid mixtures and polymeric solutions, Chem. Eng. Sci., 60 (2005) 4581-4592.

Reuvers, A. J., J. W. A. van den Berg and C. A. Smolders, Formation of membrane by means of immersion precipitation: Part I. A model to describe mass transfer during immersion precipitation, J. Membr. Sci., 34 (1987) 45-65.

Ross, G. J., J. F. Watts, M. P. Hill and P. Morrissey, Surface modification of poly(vinyllidene fluoride) by alkaline treatment 1. The degration mechanism, Polymer, 4 (2000) 1685-1696.

Sadrzadeh, M., A. Razmi and T. Mohammadi, Separation of different ions from wastewater at various operating conditions using electrodialysis, Sep. Sci. Technol., 54 (2007) 147-156.

Seiler, D. A. and J. Scheirs, Modern Fluoropolymers, 2nd ed., Wiley, Chichester, 1998.

Shao, P., R. Y. M. Huang, X. Feng and W. Anderson, Gas-liquid displacement method for estimating membrane pore-size distributions, AIChE J., 50 (2004) 557-565.

Shao, P. and R.Y.M. Huang, Analytical approach to the gas in hollow fiber membranes, J. Membr. Sci., 271 (2006) 69-76.

Shih, H. C., Y. S. Yeh and H. Yasuda, Morphology of microporous poly(vinylidene fluoride) membrane studied by gas permeation and scanning electron microscopy, J. Membr. Sci., 50 (1990) 299-317.

Shimizu, H., H. Kawakami and S. Nagaoka, Membrane formation mechanism and permeation properties of a novel porous polyimide membrane, Polym. Adv. Technol., 13 (2002) 370-380.

Silverstein, R. M., F. X. Webster and D. J. Kiemle, Spectrometric Identification of Organic Compounds, 7th ed., Wiley, Hoboken, 2005.

Snir, R., L. Wicker, P. E. Koehler and K. A. Sims, Membrane fouling and molecular weight cutoff effects on the partitioning of pectinesterase, J. Agric. Food. Chem., 44 (1996) 2091-2095.

Stengaard, F. F., Characteristics and performance of new types of ultrafiltration membrane with chemical modified surfaces, Desalination, 70 (1998) 207-224.

Strathmann, H. and K. Kock, The formation mechanism of phase inversion membranes, Desalination, 21 (1971) 241-255

Su, Y., C. Li, W. Zhao, Q. Shi, H. Wang, Z. Jiang and S. Zhu, Modification of polyethersulfone ultrafiltration membranes with phosphorylcholine copolymer can remarkably improve the antifouling and permeation properties, J. Membr. Sci., 322 (2008) 171-177.

Tarvainen, T., T. Nevalainen, A. Sundell and B. Svarfvar, Drug release from poly(acrylic acid) grafted poly(vinylidene fluoride) membrane bags in the gastrointestinal tract in the rat and dog, J. Controlled Release, 66 (2000) 19.

Tomaszewska, M., Preparation and properties of flat-sheet membranes from poly(vinylidene fluoride) for membrane distillation, Desalination, 104 (1996) 1-11.

Tsay, C. S. and A. J. Mchugh, Mass transfer dynamics of the evaporation step in membrane formation by phase inversion, J. Membr. Sci., 64 (1991a) 81-92.

Tsay, C. S. and A. J. Mchugh, The combined effects of evaporation and quench steps on asymmetric membrane formation by phase inversion, J. Polym. Sci., Part B: Polym. Phys., 29 (1991b) 1261-1270.

Uragrami, T., M. Fujimoto and M. Sugihara, Studies on synthesis and permeabilities of special polymer membranes. 28. Permeation characteristics and structure of interpolymer membranes from poly(vinylidene fluoride) and poly(styrene sulfonic acid), Desalination, 34 (1980) 311-323.

Van´t Hof, J. A., A. J. Reuvers, R. M. Boom, H. H. M. Rolevink and C. A. Smolders, Preparation of asymmetric gas separation membranes with high selectivity by a dual-bath coagulation method, J. Membr. Sci., 70 (1992) 17-30.

Wang, D., K. Li and W. K. Teo, Effects of temperature and pressure on gas permselection properties in asymmetric membranes, J. Membr. Sci., 105 (1995) 89-101.

Wang, D., K. Li and W. K. Teo, Preparation and characterization of polyvinylidene fluoride (PVDF) hollow fiber membranes, J. Membr. Sci., 163 (1999) 211-220.

Wang, D., K. Li and W. K. Teo, Porous PVDF asymmetric hollow fiber membranes prepared with the use of small molecular additives, J. Membr. Sci., 178 (2000) 13-23.

Weast, R. C., Handbook of Chemistry and Physics, Chemical Rubber, Boca Raton, 1976.

Wirth, D. and C. Cabassud, Water desalination using membrane distillation comparison between inside out and outside in permeation, Desalination, 147 (2002) 139-145.

Witte, P. van de, P. J. Dijkstra, J. W. A. van den Berg and J. Feijin, Phase separation processes in polymer solutions in relation to membrane formation, J. Membr. Sci., 117 (1996) 1-31.

Yan, L., Y. Li and C. Xiang, Preparation of poly(vinylidene fluoride) (PVDF) ultrafiltration membrane modified by nano-sized alumina (Al_2O_3) and its antifouling research, Polymer, 46 (2005) 7701-7706.

Yan, J., S. Shao, J. Wang and J. Liu, Improvement of a multi-stage flash seawater desalination system for cogeneration power plants, Desalination, 217 (2007) 191-202.

Yeon, S., K. Lee, B. Sea, Y. Park and K. Lee, Application of pilot-scale membrane contactor hydrid system for removal of carbon dioxide from flue gas, J. Membr. Sci., 257 (2005) 156-160.

Yeow, M. L., Y. T. Liu and K. Li, Morphological study of poly(vinylidene fluoride) asymmetric membranes: effects of the solvent, additive, and dope temperature, J. Appl. Polym. Sci., 92 (2004) 1782-1789.

Yeow, M. L., Y. Liu and K. Li, Preparation of porous PVDF hollow fiber membrane via a phase inversion method using lithium perchlorate ($LiClO_4$) as an additive, J. Membr. Sci., 258 (2005) 16-22.

Yin, X., H. Cheng, X. Wang and Y. Yao, Morphology and properties of hollow fiber membrane made by PAN mixing with small amount of PVDF, J. Membr. Sci., 146 (1998) 179-184.

Ying, L., P. Wang, E. T. Kang and K. G. Neoh, Synthesis and characterization of poly(acrylic acid)-graft-poly(vinylidene fluoride) copolymers and pH-Sensitive membranes, Macromolecules, 35 (2002) 673-679.

Young, T. and L. Chen, A two-step mechanism of diffusion-controlled ethylene vinyl alcohol membrane formation, J. Membr. Sci., 57 (1991a) 69-81.

Young, T. and L. Chen, A diffusion-controlled model for wet-casting membrane formation, J. Membr. Sci., 59 (1991b) 169-181.

Young, T., Y. Huang and L. Chen, Effect of solvent evaporation on the formation of asymmetric and symmetric membranes with crystallizable EVAL polymer, J. Membr. Sci., 164 (2000) 111-120.

Zhao, Y. and M. W. Urban, Spectroscopic studies of microwave plasma reactions of maleic anhydride on poly(vinylidene fluoride) surfaces: crystallinity and surface reactions, Langmuir, 15 (1999), 3538-3544.

Zeman, L. and T. Fraser, Formation of air-cast cellulose acetate membranes part II. Kinetics of demixing and microvoid growth, J. Membr. Sci., 87 (1994) 267-279.

Zeman, J. L. and A. L. Zydney, Microfiltration and Ultrafiltration: Principles and Applications, Marcel Dekker, New York, 1996.

Appendix A

The relationship between the nitrogen flux and pressure for the various fibers

---

Table A.1 Spinning conditions of hollow fibers 1-9.

Serial number	Dope composition (wt %)	Air gap (cm)	Relative humidity (%)	Taken-up speed (m/min)	Internal coagulant velocity (m/min)	Dope extrusion rate (ml/min)
1	Kynar 741:NMP =82:18	7.8	42	5.92	4.07	2.53
2	Kynar 741:NMP =82:18	7.8	42	5.92	5.09	2.53
3	Kynar 741:NMP =82:18	7.8	42	5.92	8.15	2.53
4	Kynar 741:NMP =82:18	7.8	42	5.92	3.06	2.53
5	Kynar 741:NMP =82:18	7.8	42	8.70	6.11	2.53
6	Kynar 741:NMP:LiCl =78.4:18:3.6	7.8	21	8.70	14.26	1.19
7	Kynar 2851:NMP =82:18	7.9	50	5.92	6.11	3.99
8	Kynar 2851:NMP =82:18	7.9	50	5.92	6.11	6.67
9	Kynar 2851:NMP:LiCl =78.4:18:3.6	8.7	28-30	5.92	7.13	0.43

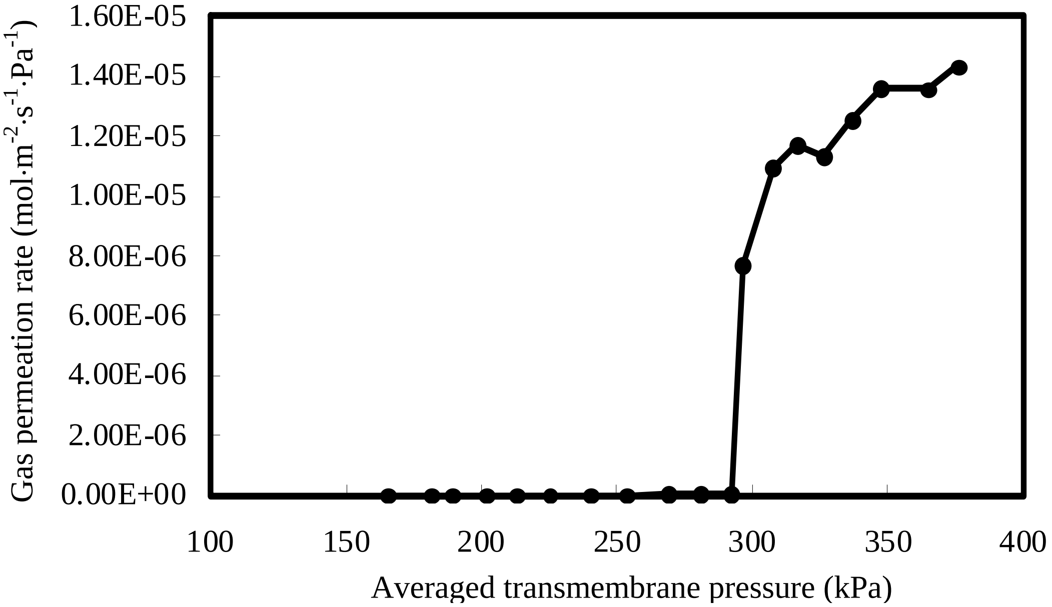

Figure A.1 Progressive gas permeation rate of membrane 1 vs. the averaged pressure.

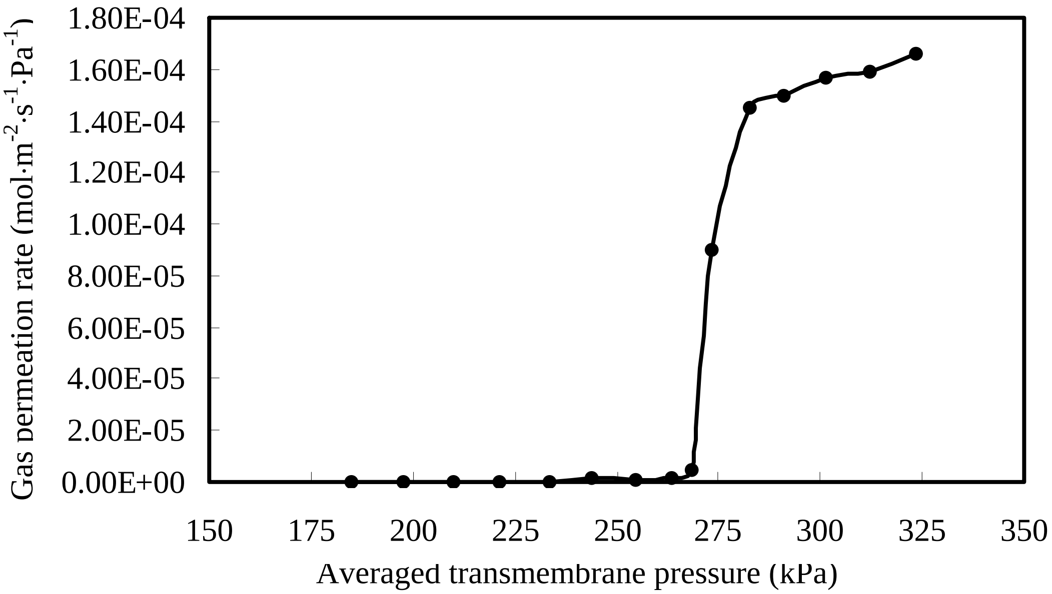

Figure A.2 Progressive gas permeation rate of membrane 2 vs. the averaged pressure.

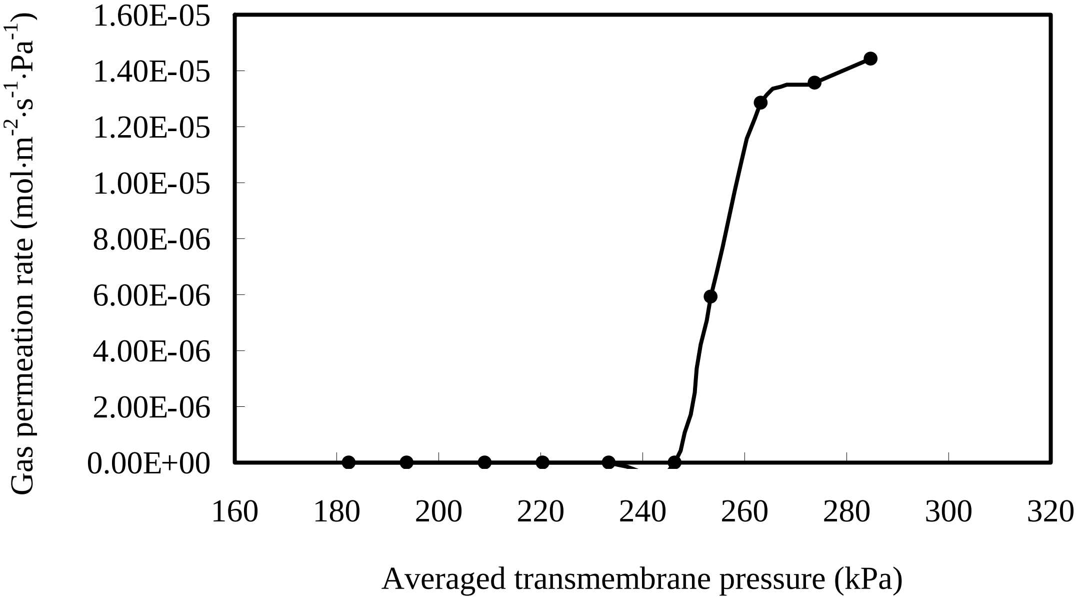

Figure A.3 Progressive gas permeation rate of membrane 3 vs. the averaged pressure.

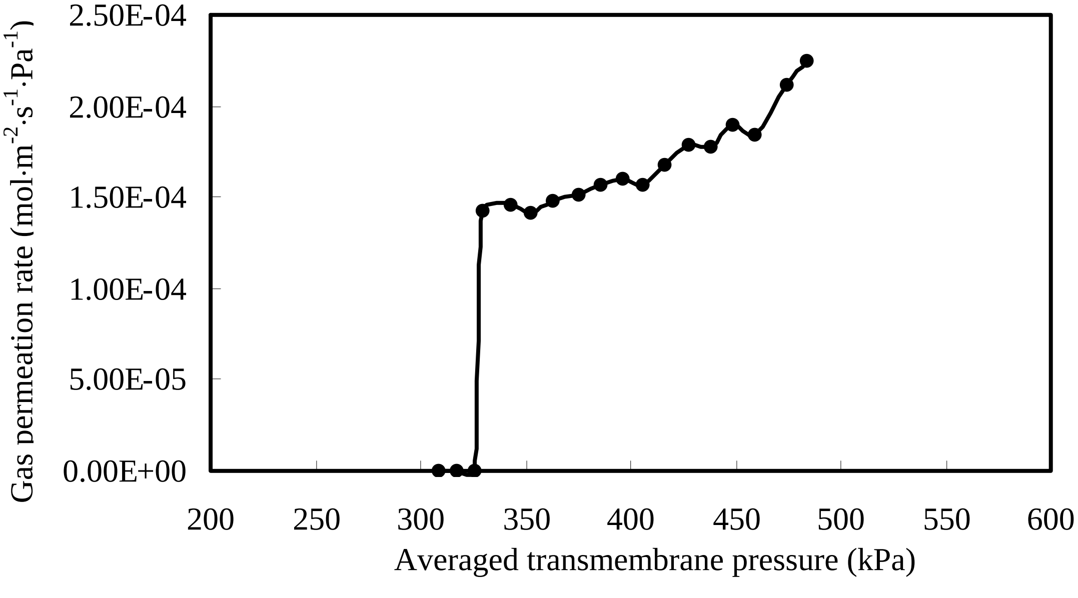

Figure A.4 Progressive gas permeation rate of membrane 4 vs. the averaged pressure.

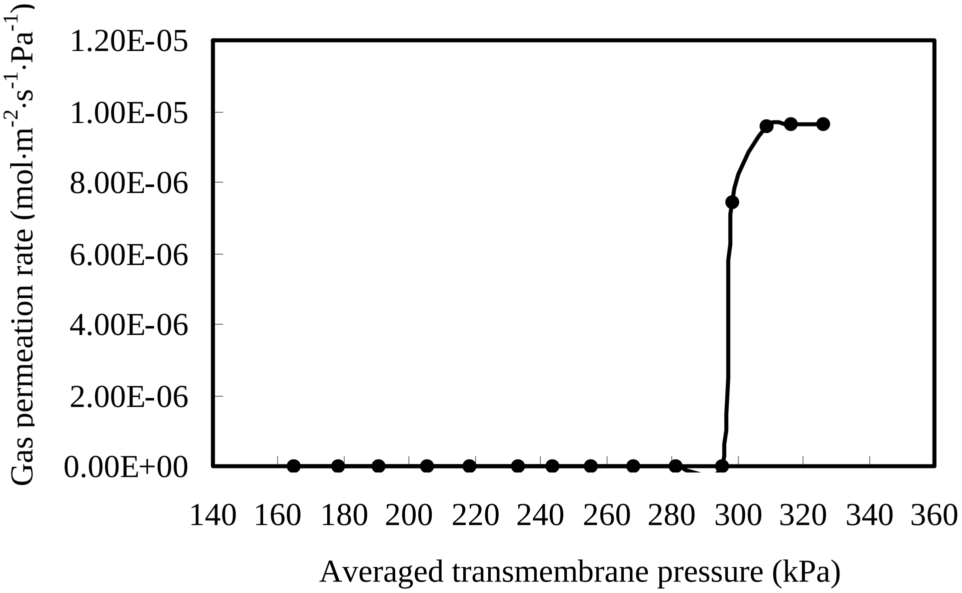

Figure A.5 Progressive gas permeation rate of membrane 5 vs. the averaged pressure.

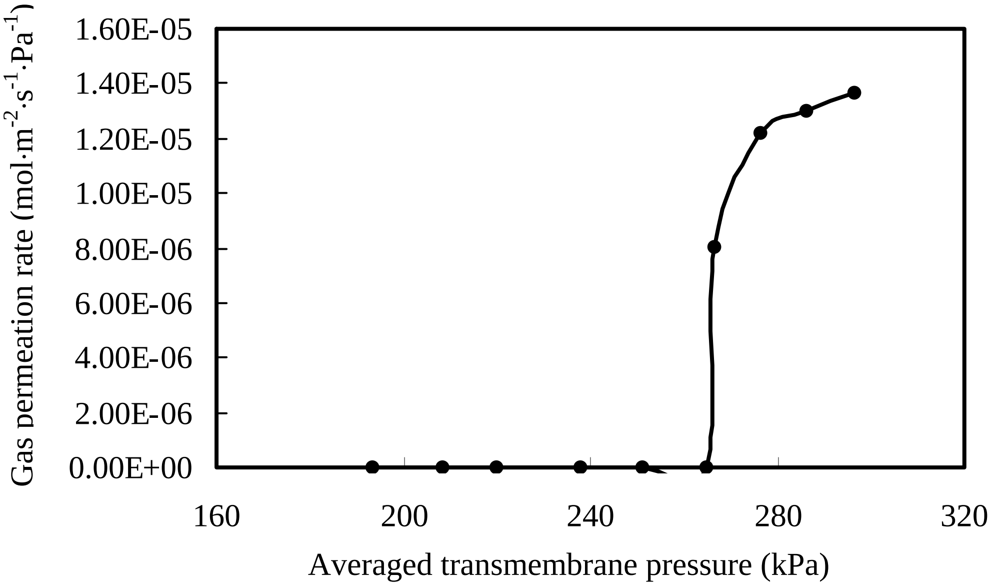

Figure A.6 Progressive gas permeation rate of membrane 6 vs. the averaged pressure.

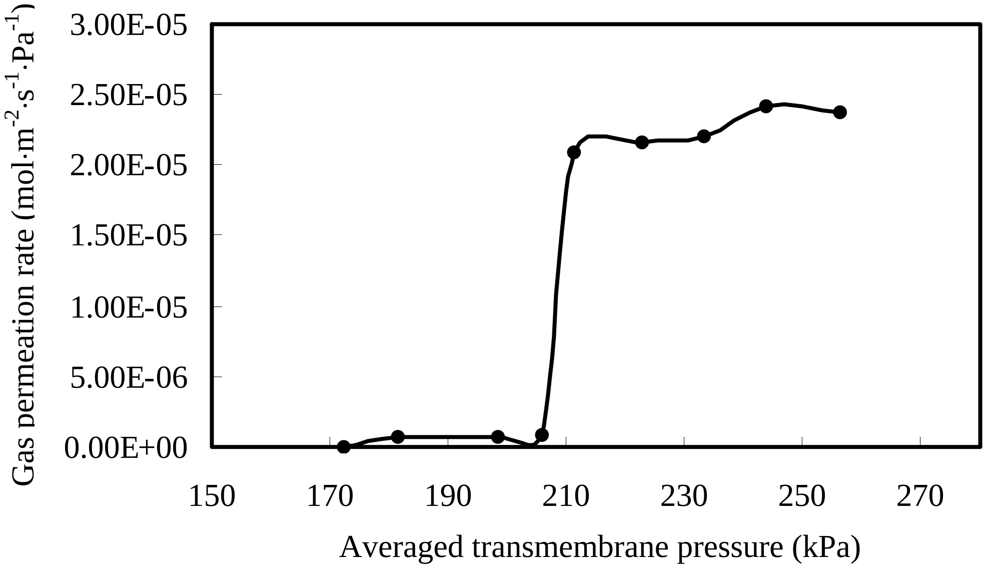

Figure A.7 Progressive gas permeation rate of membrane 7 vs. the averaged pressure.

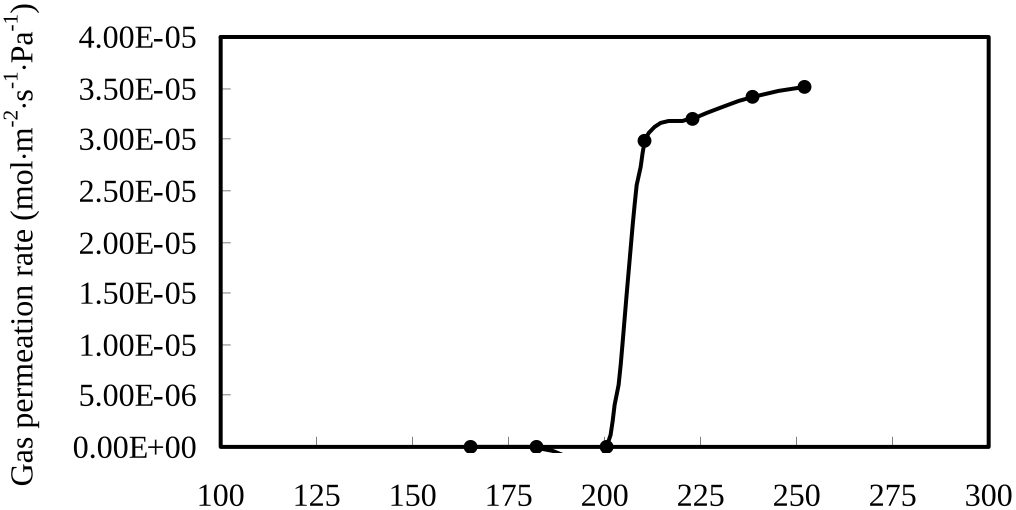

Figure A.8 Progressive gas permeation rate of membrane 8 vs. the averaged pressure.

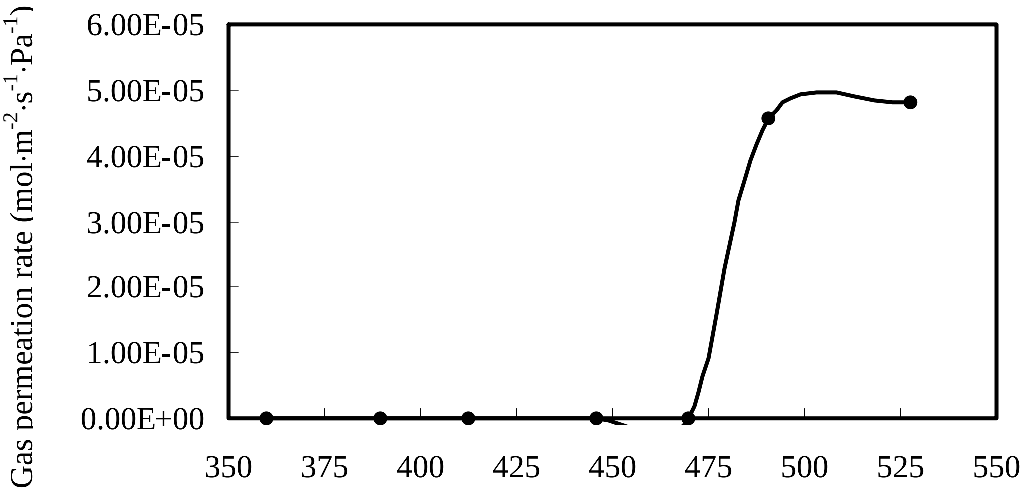

Averaged transmembrane pressure (kPa)

Figure A.9 Progressive gas permeation rate of membrane 9 vs. the averaged pressure.

Appendix B

EDAX spectra of PVDF membranes

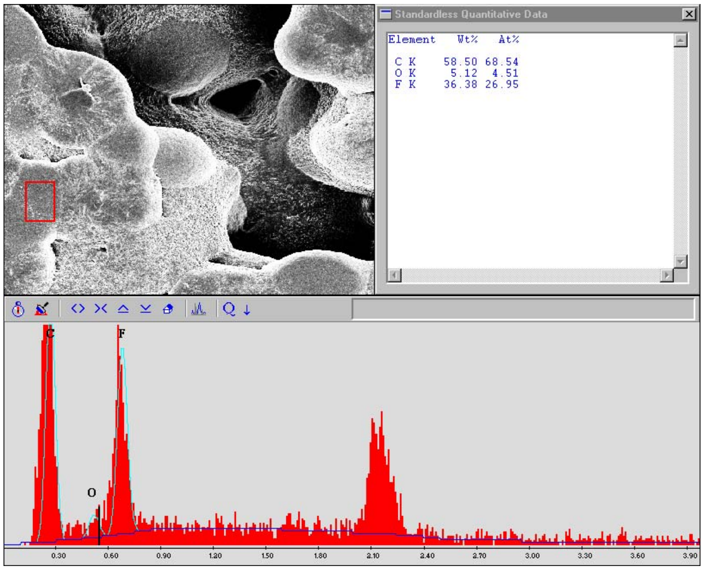

```
Element   Wt%   At%

 C K    58.50 68.54
 O K     5.12  4.51
 F K    36.38 26.95
```

Figure B.1 EDAX spectra of the original membrane.

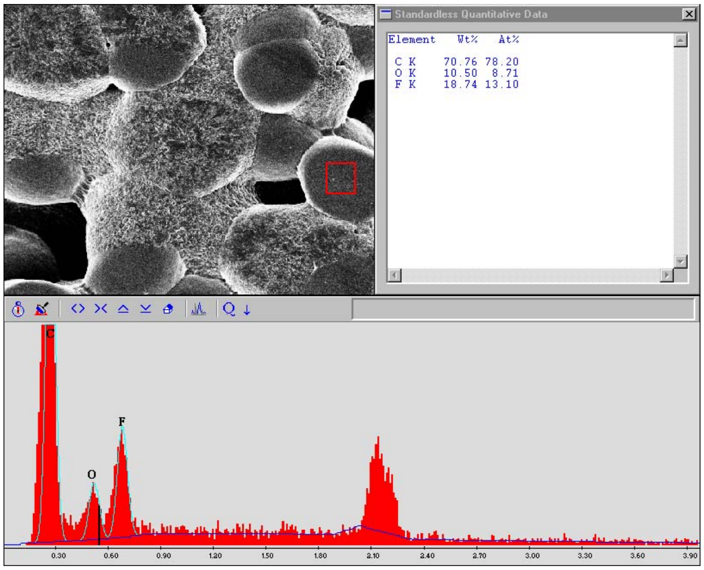

```
Element   Wt%   At%

 C K    70.76 78.20
 O K    10.50  8.71
 F K    18.74 13.10
```

Figure B.2 EDAX spectra of PVDF membranes after 5 h surface modification in 16M MEA at 80°C

Appendix C

Construction of ANOVA table

The procedure to construct the ANOVA table is given in this section, based on a model with three factors, of which factor A has *a* levels (subscript *i*), factor B has *b* levels (subscript *j*), and factor C has *c* levels (subscript *k*). Let there be *r* repeat tests for each combination of the factors [Mason, 2003].

The total sum of squares (TSS) [Mason, 2003]:

$$TSS = \sum_i \sum_j \sum_k \sum_l (y_{ijkl} - \bar{y}_{....})^2 \qquad \text{(C.1)}$$

$\bar{y}_{....}$ the overall average response.

The sum of squares for the main factors, interactions and error [Mason, 2003]:

$$SS_A = \sum_i y^2_{i...} / bcr - SS_M \qquad \text{(C.2)}$$

$$SS_B = \sum_j y^2_{.j..} / acr - SS_M \qquad \text{(C.3)}$$

$$SS_C = \sum_k y^2_{..k.} / abr - SS_M \qquad \text{(C.4)}$$

$$SS_{AB} = \sum_i \sum_j y^2_{ij..} / cr - SS_M - SS_A - SS_B \qquad \text{(C.5)}$$

$$SS_{AC} = \sum_i \sum_k y^2_{i.j.} / br - SS_M - SS_A - SS_C \qquad \text{(C.6)}$$

$$SS_{BC} = \sum_j \sum_k y^2_{.jk.} / ar - SS_M - SS_B - SS_C \qquad \text{(C.7)}$$

$$SS_{ABC} = \sum_i \sum_j \sum_k y^2_{ijk.} / r - SS_M - SS_A - SS_B - SS_C - SS_{AB} - SS_{AC} - SS_{BC} \qquad \text{(C.8)}$$

$$SS_E = TSS - SS_A - SS_B - SS_C - SS_{AB} - SS_{AC} - SS_{BC} - SS_{ABC} \qquad \text{(C.9)}$$

$$y_{....} = \sum_i \sum_j \sum_k \sum_l y_{ijkl} \quad \text{(C.10)}$$

$$y_{i...} = \sum_j \sum_k \sum_l y_{ijkl} \quad \text{(C.11)}$$

$$y_{ij..} = \sum_k \sum_l y_{ijkl} \quad \text{(C.12)}$$

$$y_{ikl.} = \sum_l y_{ijkl} \quad \text{(C.13)}$$

$$SS_M = y_{....}^2 / n \quad \text{(C.14)}$$

$$n = abcr \quad \text{(C.15)}$$

The mean sum of square [Mason, 2003]:

$$MS = \frac{SS}{df} \quad \text{(C.16)}$$

where df is the degree of freedom. Each factorial effect is assigned one degree of freedom; the total degree of freedom is $abcr - 1$.

The test statistic F-value is used to identify significant factors and interactions. In this research, statistical results were calculated by equation C.17 [Mason, 2003],

$$F = \frac{MS_{Effect}}{MS_{Error}} \quad \text{(C.17)}$$

Appendix D

Thermodynamics of sodium chloride solution

Saturated vapor pressure P_{sat} of an aqueous sodium chloride solution can be related to the vapor pressure of pure water by the following relationship [Mokbel et al., 1997]:

$$P_{sat} = \gamma P_{sat}^{o} \tag{D.1}$$

where γ is the activity coefficient of the water.

The value of γ can be found by equation D.2 [Pitzer and Pelper, 1984]. Osmotic coefficient ϕ of sodium chloride is defined by the equation:

$$\ln(\gamma) = \phi \ln(x) \tag{D.2}$$

where x is the molar percentage of water in the solution.

$$\begin{aligned}\phi - 1 = &-\left|z_+ z_-\right| A_\phi \frac{I^{0.5}}{1 + bI^{0.5}} \\ &+ m\frac{2\nu_+\nu_-}{\nu}\left[\beta^{(0)} + 2\beta^{(1)}e^{-\alpha I^{0.5}}\right] + m^2\frac{2(\nu_+\nu_-)^{1.5}}{\nu}C^\phi\end{aligned} \tag{D.3}$$

where z_+ and z_- are the charges of the ions, ν_+ and ν_- are the stoichiometric numbers of ions formed upon dissociation, ν is the number of ions generated on completed dissociation. α and b are the constants of the model with the values 2.0 $kg^{0.5}\cdot mol^{-0.5}$ and 1.2 $kg^{0.5}\cdot mol^{-0.5}$, respectively. I is the ionic strength:

$$I = \frac{1}{2}\sum_i m_i z_i^2 \tag{D.4}$$

And A_Φ is the Debye Hückel slope,

$$A_\phi = \frac{1}{3}\left(\frac{2\pi N_A \rho_w}{1000}\right)^{0.5}\left(\frac{e^2}{DkT}\right)^{1.5} \tag{D.5}$$

N_A is the Avogadro's number, e is the electric charge, ρ_w is the water density and D is the Dielectric constant.

$\beta^{(0)}$, $\beta^{(1)}$, and C^{ϕ} are adjustable parameters (ion-interaction parameters) dependent on temperature. Using Pitzer's notations, it comes:

$$\beta^{(0)} = w_6 + \frac{w_7}{T} + w_8 \ln T + w_9 T + w_{10} T^2 + \frac{w_{11}}{T - 227} + \frac{w_{12}}{680 - T} \tag{D.6}$$

$$\beta^{(1)} = w_{13} + \frac{w_{14}}{T} + w_{15} T + \frac{w_{16}}{T - 227} \tag{D.7}$$

$$C^{\phi} = w_{17} + \frac{w_{18}}{T} + w_{19} \ln T + w_{20} T + \frac{w_{21}}{T - 227} \tag{D.8}$$

The adjustable data are reported in Table D.1

Table D.1 Adjusted parameters: w_i [Mokbel et al., 1997].

i	w_i
6	2.50E+01
7	-6.53E+02
8	-4.49
9	1.10E-02
10	-4.70E-06
11	-1.19E+00
12	5.45E+00
13	-4.83E-01
14	1.19E+02
15	1.41E-03
16	-4.234548
17	4.06E-01
18	-6.11E+00
19	-7.54E-02
20	1.37E-04
21	2.76E-01

In terms of the dielectric constant, the equation takes the following form [Bradley and Pitzer, 1979]:

$$\mathrm{D} = D_{1000} + C\ln\left(\frac{B+P}{B+1000}\right) \quad \text{(D.9)}$$

D_{1000}, C and B are temperature dependent parameters. The choice of 1000 bar or the reference (D_{1000}) is just a matter of convenience; another pressure accessible at all temperature could have been used [Bradley and Pitzer, 1979]. The expressions of temperature dependence for these three parameters are as follows [Bradley and Pitzer, 1979]:

$$D_{1000} = U_1 \exp(U_2 T + U_3 T^2) \quad \text{(D.10)}$$

$$C = U_4 + U_5 /(U_6 + T) \quad \text{(D.11)}$$

$$B = U_7 + U_8 / T + U_9 T \quad \text{(D.12)}$$

The equations are valid in region of 0-350°C. The values of U_1-U_9 are given in Table D.2.

Table D.2 Values of U_i [Bradley and Pitzer, 1979].

i	U_i
1	3.43E+02
2	-5.09E-03
3	9.47E-07
4	-2.05E+00
5	3.12E+03
6	-1.83E+02
7	8.03E+03
8	4.21E+06
9	2.14E+00